Surface-Confined Molecular Self-Assembly

Dissertation der Fakultät für Geowissenschaften der Ludwig-Maximilians-Universität München

Rico Gutzler

München, 14. September 2010

Supervisor: Prof. Dr. Markus Lackinger

Second Referee: Prof. Dr. Wolfgang M. Heckl

Disputation: 19. November 2010

Abstract

The design and fabrication of nanometer-sized entities of defined structure on the nanometer scale is a challenge hardly achievable by large-scale top-down procedures. In particular, alternative techniques are needed to structure surfaces at very small length scales. In nanotechnology the process of self-assembly has become a potent method which allows to vanquish these difficulties. Self-assembly is a mechanism by which randomly distributed small units arrange into large, ordered structures under equilibrium conditions. Information about the final morphology of the self-assembled structure is encoded at least partially in the basic building units. The environment constitutes an additional parameter which influences the self-assembly process, impairing both its thermodynamics and kinetics. Thus, any assembly has to be interpreted in view of the boundary conditions which the environment inflicts.
In the following, self-assembly of molecules is elucidated based on experimental results. The formation of molecular monolayers at surfaces, under ambient conditions as well as in vacuum, is discussed in the light of the parameters that govern self-assembly. Thermodynamic and kinetic considerations are employed to gain deeper insight into the growth mechanisms of the monolayers. The primary instrument applied is the scanning tunneling microscope, a device which facilitates the real-space observation of surface-bound molecular structures with submolecular resolution. The assembly of various organic molecules is studied at the liquid/solid interface under ambient conditions. Especially the effects of molecular structure and molecular interactions, type of solvent, concentration, and temperature on the self-assembly process are investigated. Additionally, monolayer formation under ultra-high vacuum conditions is explored. Particularly the influence of temperature and of the type and crystallographic orientation of the crystal surface that serves as substrate for monolayer growth is studied. Both cases, liquid/solid and ultra-high vacuum, are fundamentally different with respect to the environment in which molecular self-assembly takes place. Hence they allow for comparative and complementary conclusions when adequately analyzed. This knowledge provides a basis for the deliberate tuning of the morphology of self-assembled monolayers, and eventually facilitates the defined manipulation of surfaces at the molecular level. Although much research has been done on self-assembled molecular monolayers, the delicate interplay between building blocks and environment in molecular self-assembly is still far from being fully understood. Only if fundamental principles and interactions in self-assembly are well comprehended, a controlled approach to deliberate surface patterning and functionalization becomes feasible.

Contents

Chapter 1

Introduction

1.1 Self-Assembly in Nanotechnology

A great part of current advances in nanoscience and nanotechnology is based on a process termed self-assembly, a mechanism by which disordered small building units spontaneously arrange into large, ordered phases. For example, self-assembly steers the growth of molecular crystals[1] and molecular monolayers,[2] is responsible for the folding of proteins,[3,4] and affects the morphology of lipid bilayers[5] and colloidal particles.[6] The importance of self-assembly thus manifests itself not only in the advances in material science, but also through its role in biology, life science, and the physics and chemistry of soft matter. Further examples for the successful use of self-assembly as a bottom-up approach for engineering at very small dimensions include the fabrication of nanoscopic structures like quantum dots,[7] photonic-bandgap materials,[8] and the design of hybrid organic-inorganic materials.[9] Supramolecular chemistry at surfaces, i.e., the association of molecules through rather weak non-covalent bonds, is yet another case where molecular self-assembly is decisive.[10–14] In this work the formation of molecular monolayers will be discussed in some detail, and the importance of self-assembly for this process will be elucidated.

Understanding how molecular crystals emerge in self-assembly from a disordered state requires more than just knowledge about the forces between two molecules. Rather rarely it is appreciated that kinetic and entropic considerations are equally important. Owing to the fact that material synthesis through self-assembly is still mostly a trial-and-error process, a profound understanding of its underlying concepts is desirable, and will eventually lead to more educated approaches to various problems in nanotechnology. Particularly supramolecular crystal engineering in two-dimensions (2D) is the principal objective for structuring and functionalizing surfaces. At the molecular level, self-assembly is responsible for the formation of ordered molecular monolayers at the liquid/solid interface as well as at the vacuum/solid interface. A prominent

example is the formation of self-assembled monolayers (SAM) on gold surfaces from thiol-functionalized molecules.[2] These layers permit to alter the surface termination, and thus to change the surface's physical and chemical properties. Studies on molecular thin films are naturally conducted with surface sensitive techniques like low-energy electron diffraction (LEED), atomic force microscopy (AFM), and scanning tunneling microscopy (STM). They cover a whole variety of research interests like the identification of exact epitaxial relations of adsorbate to substrate lattice,[15,16] dewetting of organic molecular layers on insulators,[17] molecular transport on surfaces,[18] or probing properties like molecular orbital distributions.[19–21] Especially the STM has proven to be a beneficial tool for probing molecules with high spatial resolution. Its use is not limited to imaging single molecules, islands of molecular aggregates, and monolayers in real space, but furthermore allows to acquire information about the local electronic structure of a molecule by scanning tunneling spectroscopy (STS).[22,23] This work continues with a brief convenient definition of self-assembly and its detailed description for molecular systems at surfaces. The next section gives a short description of scanning tunneling microscopy of molecular monolayers, since it was the primary technique used in this work. This includes a description of the low-temperature ultra-high vacuum STM which was set up as a complementary instrument to an ambient liquid/solid STM. Following, kinetics and thermodynamics are discussed, and their impact on molecular self-assembly is elucidated. The parameters that influence molecular self-assembly are examined and can be classified in two categories. Internal parameters, as for example structure and functionalization of the building blocks, i.e., the molecules, and external parameters, the background or environment in which the self-assembly takes place, e.g., temperature, substrate, solvent, and the like. A detailed analysis of internal and external parameters is illustrated by experimental results. This includes a distinction between liquid/solid and vacuum/solid interface, as well as the effects of substrate, concentration, and temperature on molecular self-assembly. Likewise, molecular properties like size, chemical structure, and molecular interactions are considered. A summary of this first part of the work finally leads to a compendium of published articles including the experimental results described.

1.2 Self-Assembly, a Brief Definition

As already stated, self-assembly is an autonomous process by which independent building units form ordered structures from a previously disordered state. These building units are separate fundamental entities in which relevant information about the outcome of the self-assembly process is encoded. The environment in which self-assembly takes place is likewise a relevant factor, and crucially influences its outcome. Various definitions of self-assembly are presented in literature which differ in some minor or major details as reviewed by Halley and Winkler.[24] From their text the following definition is adopted, which seems to be adequate for the case of molecular self-assembly:

> Self-assembly is a nondissipative structural order on a macroscopic level, because of collective interactions between multiple (usually microscopic) components that do not change their character upon integration into the self-assembled structure. This process is spontaneous because the energy of unassembled components is higher than the self-assembled structure, which is in static equilibrium, persisting without the need for energy input.

In the case of supramolecular structures, molecules take the part of the fundamental building units (components). The resulting crystalline structure is formed by nondissipative mechanisms, which means that no external energy input is required to form the structure. The intrinsic morphology, i.e., unit cell parameters and arrangement of molecules within the unit cell, is dominantly governed by molecular interactions as for example van der Waals forces, hydrogen bonds, aromatic interactions, and metal-organic bonds. These interactions encode how molecules collocate with respect to each other, and thus define the local microscopic structure within a 2D crystal. The environment in which the molecules self-assemble comprises parameters like temperature, type of solvent and concentration, or vacuum and vapor pressure. Certainly also the surface is of importance, as its interaction with the molecules can define the self-assembly and the commensurability of the molecular monolayer. Furthermore, Halley and Winkler explicitly point out that an element of reversibility has to be present in the bond formation. The reversibility of an intermolecular bond implies a self-healing mechanism, which allows defects in the structure to be repaired and to relax the system into thermodynamic equilibrium. If this reversibility was not present, the resulting structure would not show the long range order which is common to self-assembled monolayers, and disordered glassy states would be observed.

Chapter 2

Scanning Tunneling Microscopy

2.1 Contrast Formation in Molecular Adsorbates

The Scanning Tunneling Microscope is a powerful instrument to image molecular monolayers at surfaces. A sharp metallic STM tip allows to obtain topographs with submolecular resolution, and thus enables one to elucidate relative positions and orientations of molecules within the monolayer. In contrast to other surface sensitive techniques which rely on diffraction of incident waves, like the diffraction of low-energy electrons, the STM can image structures which do not possess translational symmetry. This includes resolving single isolated molecules and disordered monolayers. Although limited by a major drawback, the restriction to electrically conductive surfaces, the STM has proven to be a potent device for surface science.[10,12,13,22,23,25–29]

The contrast in STM images is not merely defined by the topography of the sample, but also represents its electronic structure, i.e., the electronic states accessible to the tunneling electrons. A simplistic model for conduction through single energy levels is given by Datta.[30] This model is easily extended to the case of tunneling through molecules, and explains the dependence of the image on the electronic structure. It is described at first in general for a molecule connected to two electrodes, and is later adopted to the case for asymmetric coupling of the molecule to surface and tip, as encountered in the case of STM. Two metallic electrodes, the surface and the tip, sandwich a one-level system, idealizing the molecule (Figure 2.1). In the equilibrium state, when the two electrodes are short-circuited, the Fermi levels align as do consequently the filled and empty states of each electrode (Figure 2.1 a). The average occupation of each energy level of the electrodes is given by the Fermi distribution

$$f(E) = \frac{1}{\exp\left(\frac{E-\mu_0}{k_\mathrm{B}T}\right)+1}, \tag{2.1}$$

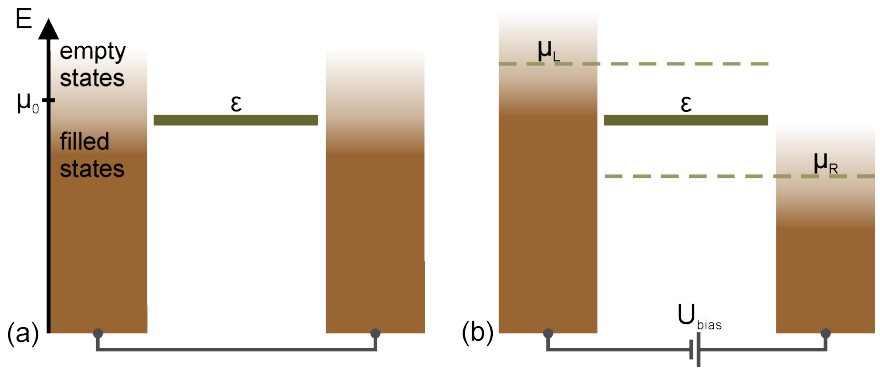

Figure 2.1 – Schematic model for the conduction through a one-level molecule. (a) Zero bias between the two short-circuited electrodes with aligned Fermi levels μ_0. The molecular level with energy ϵ lies somewhere fixed relative to the Fermi energy. (b) With a voltage applied, the Fermi levels shift with respect to each other by U_{bias} with $\mu_{\text{L}} = \mu_{\text{R}} + eU_{\text{bias}}$, enforcing different occupancies n on the molecular level.

where μ_0 is the Fermi level, k_{B} Boltzmann's constant and T the temperature. This function is 0 for energies E far above μ_0, and 1 for energies far below μ_0. A positive voltage U_{bias} applied to the right electrode lowers its Fermi level and raises the Fermi level of the left electrode (Figure 2.1 b). The energetic difference between both electrodes is $\mu_{\text{L}} - \mu_{\text{R}} = eU_{\text{bias}}$, with e being the fundamental charge, giving rise to two different Fermi distributions:

$$f_{\text{L}}(E) = \frac{1}{\exp\left(\frac{E-\mu_{\text{L}}}{k_{\text{B}}T}\right)+1} \tag{2.2}$$

$$f_{\text{R}}(E) = \frac{1}{\exp\left(\frac{E-\mu_{\text{R}}}{k_{\text{B}}T}\right)+1}. \tag{2.3}$$

In the case of Figure 2.1 a, the molecular level with an energy ϵ has the same occupancy as the respective Fermi function of the electrodes $f(\epsilon)$. Conduction is not possible since the molecule is in equilibrium with both electrodes. On the other hand, both electrodes attempt to impose different occupancies on the molecular level due to the different Fermi distributions when a voltage is applied (Figure 2.1 b). In this non-equilibrium state, each electrode intends to equilibrate the molecular level with its respective value of the Fermi distribution at energy ϵ. Electrons are injected from the left electrode, which enforces an occupancy of the molecular level of $f_{\text{L}}(\epsilon)$. At the same time the level is depleted from charge by the right electrode, which would be in equilibrium with the molecular level if it had an occupancy of $f_{\text{R}}(\epsilon)$. Thus, when the molecular level is an empty state, like for example the lowest unoccupied molecular

orbital (LUMO), electrons enter from the left electrode and leave to the right electrode, resulting in a net current through the molecule. If, on the other hand, the state is an occupied level, like the highest occupied molecular orbital (HOMO), charge is drawn away from the level from the right before it is refilled from the left, and the same current arises. The effective occupancy n of the molecular level at steady state lies then somewhere in between $f_{\mathrm{L}}(\epsilon)$ and $f_{\mathrm{R}}(\epsilon)$. The direction of the current through the molecule does not depend on whether the molecular level is already filled with electrons or whether it is empty at a given potential U_{bias}. Nevertheless, the magnitude of the current depends on the occupancy of the molecular level with charge carriers. This model points out that without the presence of a molecular energy level in between μ_L and μ_{R}, no conduction takes place through the molecule, since no allowed states for charge carriers exist in between the electrodes. Tunneling would then occur directly from tip to substrate (or vice versa). It also shows that only electrons with an energy below μ_{L} and above μ_{R} (within some $k_{\mathrm{B}}T$) contribute to the current. Far above μ_{L} all states in the left electrodes are empty, and no electrons are available that can contribute to the current. In the right electrode, all level with an energy much lower than μ_{R} are fully occupied, and no states are accessible for additional electrons. If two or more molecular levels lie in between the electrodes, all levels which possess an energy ϵ_{i} within the range $\mu_{\mathrm{R}} + eU_{\mathrm{bias}}$ contribute to conduction.
The current of charge carriers q through the molecule can be calculated from the charge flux I_{L} across the left junction, which is proportional to $[f_{\mathrm{L}}(\epsilon) - n]$ (with n being the occupancy of the molecular energy level), and the flux I_{R} across the right junction, proportional to $[f_{\mathrm{R}}(\epsilon) - n]$:

$$I_{\mathrm{L}} = -q\frac{\gamma_{\mathrm{L}}}{\hbar}\left[f_{\mathrm{L}}(\epsilon) - n\right] \tag{2.4}$$

$$I_{\mathrm{R}} = -q\frac{\gamma_{\mathrm{R}}}{\hbar}\left[f_{\mathrm{R}}(\epsilon) - n\right]. \tag{2.5}$$

The somewhat artificially introduced parameter γ_{i} can be interpreted as the coupling strength (interaction energy) between the respective electrode and the molecule. A large (small) γ_{i} then results in a high (low) current. The ratio $\gamma_{\mathrm{i}}/\hbar$ is a rate constant at which an electron present in the molecular level will be transferred to the left or right electrode. In equilibrium, the net current is zero, i.e., $I_{\mathrm{L}} + I_{\mathrm{R}} = 0$, which results in

$$n = \frac{\gamma_{\mathrm{L}} f_{\mathrm{L}}(E) + \gamma_{\mathrm{R}} f_{\mathrm{R}}(E)}{\gamma_{\mathrm{L}} + \gamma_{\mathrm{R}}}. \tag{2.6}$$

Substituting this expression for the occupancy n of the molecular level into either Equation 2.4 or Equation 2.5 yields

$$I = I_{\mathrm{L}} = -I_{\mathrm{R}} = 2\frac{q}{\hbar}\frac{\gamma_{\mathrm{L}}\gamma_{\mathrm{R}}}{\gamma_{\mathrm{L}} + \gamma_{\mathrm{R}}}\left[f_{\mathrm{L}}(\epsilon) - f_{\mathrm{R}}(\epsilon)\right]. \tag{2.7}$$

The newly introduced factor 2 accounts for the spin degeneracy of each energy level. This rather simple equation provides insight into the conduction of a molecule contacted by two electrodes. It permits to estimate the current once the coupling parameters γ_{i} are known. For the case when more than one molecular level exists in the respective energy interval, and thus more than one level contributes to the current, Equation 2.7 can be extended to

$$I = \sum_{\epsilon_{\mathrm{i}}} 2\frac{q}{\hbar}\frac{\gamma_{\mathrm{L}}\gamma_{\mathrm{R}}}{\gamma_{\mathrm{L}} + \gamma_{\mathrm{R}}}\left[f_{\mathrm{L}}(\epsilon_{\mathrm{i}}) - f_{\mathrm{R}}(\epsilon_{\mathrm{i}})\right] \tag{2.8}$$

with ϵ_{i} corresponding to the energy of each molecular level (Figure 2.2 a). Here it is assumed that the coupling parameter γ_{R} is the same for all energy levels, as is the parameter γ_{L}. Although in general this is not necessarily true, the following derivation can be adapted to the more generic case. The conclusions drawn below are thus equally valid.

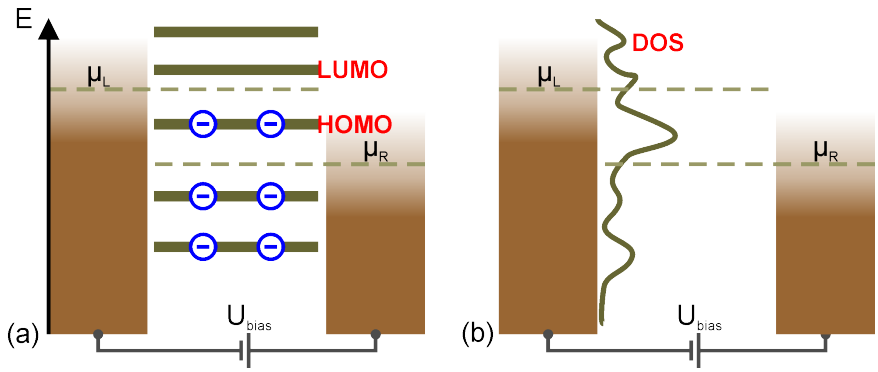

Figure 2.2 – Schematic model for conduction through a multi-level molecule. (a) Weak interaction between molecule and surface. Molecular levels are unaltered by the presence of the surface. (b) Strong interaction between molecule and substrate. An effective density of states comprised of hybridized molecule and substrate levels is formed, which consequently yields new conduction channels.

The above model explains conduction through a molecule in between two electrodes. In typical situations where STM is applied, the molecule is rather strongly bound to the substrate by either physisorption or chemisorption, in contrast to rather

weak coupling to the tip. Here the substrate is identified with the left electrode and the tip with the right electrode. In this scenario it is convenient to consider a superposition of states of the molecule with the surface (left electrode), in which molecular levels and surface states hybridize to an effective electronic structure. This can be expressed by a common effective density of states $D_{\text{eff}}(E)$ (DOS) of the strongly coupled molecule-substrate system. The integral over all energies of $D_{\text{eff}}(E)$ replaces the sum in Equation 2.8 ($\sum_{\epsilon_i} \rightarrow \int dE D_{\text{eff}}(E)$) (see also Figure 2.2 b). Furthermore, the coupling constant γ_{L} representing the molecule-substrate interaction is much larger than γ_{R}, the interaction between molecule and tip, therefore $\gamma_{\text{L}} \gg \gamma_{\text{R}}$ and $\gamma_{\text{L}} + \gamma_{\text{R}} \approx \gamma_{\text{L}}$. With these assumptions, Equation 2.8 reduces to

$$I = 2\frac{q}{\hbar}\int_{-\infty}^{\infty} dE D_{\text{eff}}(E)\gamma_{\text{R}}\left[f_{\text{L}}(E) - f_{\text{R}}(E)\right]. \tag{2.9}$$

Conduction is thus not limited to molecular levels, but the effective DOS of substrate-molecule opens a continuous distribution of charge transport channels.
To account for the tunneling in STM, one needs to replace γ_{R} by an appropriate physical coupling property. The interaction between molecule and tip for large tip-sample distances is quite weak, and the only channel available for charge carrier transfer is tunneling from an electronic quantum state in the tip to a state of the molecule or vice versa. At large electrode separations, the only way an electron can be transferred from the tip (molecule) into the molecule (tip) is by means of a suitable overlap of their wavefunctions. Only if their wavefunctions overlap, an electron has a nonzero probability to pass through the region separating both electrodes, thus establishing a tunneling current under applied bias. The wave function, and consequently the density of states of bare metal surfaces and likewise of molecules, decays exponentially perpendicular to the surface into vacuum. Wavefunction overlap, and thus charge transition probability, should thus also decay exponentially with electrode separation. The square of the tunneling matrix elements $|M|^2$ introduced by Bardeen,[31] and evaluated in more detail by Tersoff and Hamann[32] for the case of scanning tunneling microscopy, describes such a weak coupling between the wavefunctions of two electrodes. The tunneling process is adequately specified by the tunneling matrix whose elements are basically the tunneling (transition) probabilities from a tip state to a molecule state. Since the wavefunctions decay exponentially, it is not surprising that tunneling is extremely sensitive to the distance between tip and molecule. Effectively, Tersoff and Hamann showed that the tunneling probability falls off exponentially with the distance d between tip and sample, so that $|M|^2 \propto \exp(-2\kappa d)$ with $\kappa = \hbar^{-1}(2m\phi)^{1/2}$. Here, m is the electron mass, ϕ is a function of the work function of the tip and of the

substrate, and d is the separation between the two electrodes. Postulating γ_R to be proportional to the tunneling matrix elements $|M|^2$, the tunneling current becomes

$$I \propto 2\frac{q}{\hbar}\mathrm{e}^{-2\kappa d}\int_{-\infty}^{\infty} dE D_{\mathrm{eff}}(E)\left[f_{\mathrm{L}}(E) - f_{\mathrm{R}}(E)\right]. \tag{2.10}$$

This equation highlights the main features of contrast formation in STM images of molecular monolayers. A large signal, i.e., high brightness in either constant current or constant height STM images, can usually be attributed to a large density of states of the molecule-substrate system. The integral over the DOS and the difference in Fermi distributions indicates that only those peaks of the DOS contribute to the current which lie within the energy interval $\mu_{\mathrm{L}} - \mu_{\mathrm{R}} = eU_{\mathrm{bias}}$, or close (within a few $k_{\mathrm{B}}T$) above μ_{R} or below μ_{L}. Only in this region the term $[f_{\mathrm{L}}(E) - f_{\mathrm{R}}(E)]$ is nonzero. The exponential distance dependence of the tunneling current is owed to the tunneling matrix elements, and leads to a dependence on (physical) topography of the sample. Consequently, elevated features on a surface lead to larger signals, and hence higher brightness in STM topographs.

A short note is mandatory on the alignment of the molecular levels with respect to the surface Fermi level. The HOMO aligns just below the Fermi level, and thus the LUMO lies above the Fermi level (also compare Figure 2.2 a). Usually the vacuum level is used as a common reference point. In this picture, an electron from the surface electrode needs an energy equal to the electrode's work function in order to escape to the vacuum. Accordingly, the ionization potential is the analogue for the molecule, which is the minimum energy necessary to remove one electron from the HOMO. In general, the ionization potential of molecules is larger than the work functions of metals, therefore the HOMO lies below the Fermi level of the surface. The importance of this becomes clear when referring again to Figure 2.2 a, where a positive voltage is applied to the tip. The HOMO thus shifts right between the region where the Fermi distributions of both electrodes are between 0 and 1, and thus tunneling becomes possible if the gap eU_{bias} is large enough. In this case the HOMO is the only conduction channel where charge carriers can propagate from the surface through the molecule to the tip. All other molecular levels lie outside of this region. If one changed the polarity, the LUMO would be the molecular level inside the region where tunneling occurs. This is based on the assumption that the interaction between surface and molecule is strong enough that applying a voltage between the two electrodes does not change relative energetic positions of substrate and molecular energy levels. On the other hand, the interaction is assumed to be weak enough to allow for the description in terms of single molecular energy levels rather than hybridized states. In the case of

opposite polarity, the LUMO becomes the charge conducting channel from the tip to the surface. The relevance of these theoretical considerations was demonstrated for the case of a pentacene molecule adsorbed on weakly interacting surfaces like insulating NaCl layers on top of Cu(111) or a clean Au(111) surface.[20,21] In these studies, single molecular orbitals like LUMO, HOMO, and HOMO-1 could be imaged, depending on the voltage between tip and molecule-substrate. Contrary, imaging the same molecule directly adsorbed on Cu(111) did not reveal the internal structure of molecular orbitals, which is probably due to a strong pentacene-Cu(111) interaction.[33] Thin insulating layers like NaCl decouple the electronic structure of the adsorbant from the surface electronic structure, and facilitate imaging of discrete molecular orbitals *via* STM.

The model presented above is a simple sketch on how tunneling through molecules can be described. Obviously, a thorough description requires the use of much more complex physics and mathematics and is beyond the scope of this overview. Nevertheless, the model describes most of the important features which are necessary to understand contrast formation in scanning tunneling microscopy at molecule-metal interfaces.

2.2 The Low-Temperature Ultra-High Vacuum Scanning Tunneling Microscope

All experiments of the present work were carried out either at the liquid-solid interface with an ambient STM or at the vacuum-solid interface with a variable-temperature STM. The ambient STM is a home-built set-up controlled by commercial electronics. It allows to image self-assembled molecular monolayers by immersing the tip into a drop of solution previously applied to the substrate. While the ambient STM was pre-existing inventory of the laboratory, the UHV chamber and the low-temperature STM were built prior to conducting experiments. The design of the variable-temperature UHV STM is described elsewhere in detail[34] and was taken over with additional modifications.

In the UHV chamber, molecular deposition *via* organic molecular beam epitaxy (OMBE) is possible with the sample mounted in the STM, either at room temperature or cooled down to cryogenic temperatures. The design of the Knudsen cell is discussed in more detail below. Sample preparation by electron beam annealing and sputtering through neon ion bombardment is possible in a separate stage. This stage furthermore allows for electron beam heating of tunneling tips. Sample and tip manipulation from the storage carousel to preparation stage and STM is done with a wobble stick. The ultrahigh vacuum with a base pressure of $\sim 1 \times 10^{-10}$ mbar is generated and maintained by turbomolecular and ion getter pumps. An additional titan sublimation pump integrated into a cooling shroud (LN_2 cooled) improves the base pressure after bake out. In order to reduce vibrational coupling to the floor, the whole chamber is mounted on an air floated optical table. The STM itself is suspended from the top of a copper housing by three springs made from cold drawn Inconel 718 wire. These assure further vibrational isolation from the surrounding over a wide temperature range. The copper housing consists of a small box which is mounted inside a larger one. Its main purpose is that of a thermal radiation shield while operating at cryogenic temperatures. The material used is oxygen-free high conductivity copper (OFHC), which facilitates good heat transport when cooling down from room temperature to cryogenic temperatures. Both copper boxes are aureated on their outside and blackened on the inside to improve their effectivity as heat shields, reflecting radiation from the outside and absorbing radiation from the inside, thus keeping the STM at constant temperature. The reduction of the heat load from the environment results in lower equilibrium temperatures of the STM while working at low temperatures. The housing is attached to a flow cryostat which facilitates cooling of the STM, including the sample, with liquid helium or nitrogen. The STM itself is a beetle-type

design, where three outer piezoelectric tubes support the sample and are responsible for coarse approach of the sample to the tip and lateral scanning.[35] A center piezo tube serves as tip holder and facilitates z-scan motion. Coarse approach is realized through a stick-slip motion of the sample holder supported on top of tungsten balls, which are glued to the top of the three outer piezos. All four piezos are glued to a molybdenum base plate, which also includes connectors for the wiring. Underneath the base plate, an OFHC cross permits the clamping of the STM to the inner copper box, thus allowing both manipulation of the tip and sample, and rapid heat transfer from the STM to the copper housing. On the lateral and bottom end of the cross, cobalt-samarium magnets additionally reduce vibrational motion of the STM by eddy current damping. Most UHV data shown below were obtained with this instrument.

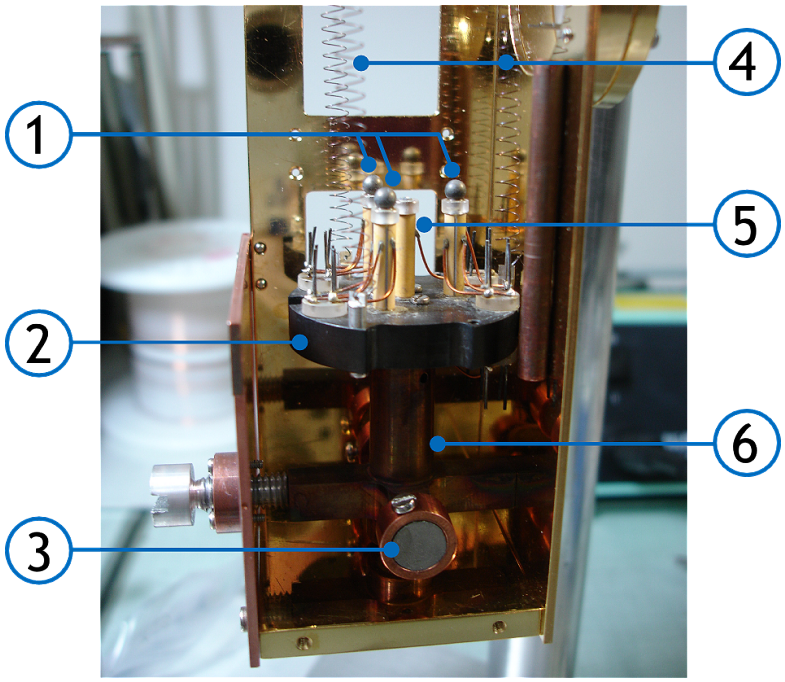

Figure 2.3 – Beetle type scanning tunneling microscope in copper housing. 1) Tungsten balls on which the sample holder rests while scanning. Balls are glued to three piezos which facilitate coarse approach and scanning in x and y direction. 2) Molybdenum base plate. 3) Cobalt-samarium magnets for eddy current damping. 4) Springs made from Inconel 718 wire attached to top of copper housing and STM base plate. 5) Inner piezo which functions as tip holder and moves tip in z direction. 6) Copper cross for rapid heat transfer and clamping of the STM.

The Knudsen cells used for molecular beam epitaxy were constructed with minor modifications according to a design presented in publication number 3 (*cf.* chapter 6). The custom-designed molecular evaporators offer the possibility to measure effusion rates with the help of a quartz crystal microbalance (QCMB) integrated into their beam shutter. These Knudsen cells facilitate the controlled deposition of molecular

monolayers of defined coverage. From the temperature dependence of the molecular deposition rate, measured using the QCMB, it is possible to calculate the sublimation enthalpy of the evaporant using the Clausius-Clapeyron equation. The combined Knudsen cell microbalance assembly has proven to be suitable both for monitoring molecular effusion rates with the QCMB, as well as for the deposition of organic compounds onto single crystals for subsequent STM experiments.

Chapter 3

Interfacial Self-Assembly, Thermodynamics, and Kinetics

The primary mechanisms in surface-confined self-assembly of molecules are the deposition of the adsorbate onto the substrate and its lateral transport on the surface. At the vacuum/solid interface, the adsorbate is usually deposited by organic molecular beam epitaxy, and once deposited molecules reside on the surface over large time scales. The long residence time, i.e., low desorption rate, is due to a high desorption energy compared to thermal energy. No further molecules are adsorbed once the molecular beam is shut off. On the other hand, adsorption from solution, as is common in liquid/solid experiments, allows for continuous deposition of molecules. A small droplet of solution applied to a surface can contain a supply of molecules much larger than required to cover the surface with a monolayer, and the droplet acts as a nearly unlimited reservoir of adsorbants. At the liquid/solid interface, a constant flux of adsorbing particles is compensated for by a constant flux of desorbing particles, resulting in a dynamic equilibrium between solution and interface in the steady state. The number of adsorbed molecules is thus constant. However, once a molecule desorbs from a surface under vacuum conditions, it is usually lost and cannot be replaced by another molecule from a reservoir. Nevertheless, desorption rates under vacuum conditions are relatively low for many molecules, and stable monolayers can be observed. In both cases, lateral transport on the surface is important for self-assembly of the molecules. A low diffusivity of the adsorbates on the surface would result in non-equilibrium structures, and only if thermally activated diffusion is present, ordered layers can grow. An assembly of a few molecules which associate on the surface can act as a nucleus for the growth of large-scale structures. Figure 3.1 shows an idealized scheme of self-assembly from the solution phase. In a first step, a molecule adsorbs from solution and diffuses on the surface. Eventually, the molecule either desorbs or binds to another molecule which is diffusing on the surface, thereby initiating growth of domains. Later, further molecules interact with the nucleus leading to larger do-

mains. After equilibration to the steady state when monolayer coverage is reached, molecules are still desorbing into solution, but can easily be replaced by molecules adsorbing from solution, resulting in a dynamic equilibrium. The adaptation of this picture to the vacuum/solid interface is straightforward by neglecting desorption and considering a time-limited flux of adsorbing molecules.

Two factors are important for molecular self-assembly: the relative thermodynamic stability of different polymorphs which can form on the surface, and the kinetic barriers associated with the formation of each polymorph. Adsorption/desorption rates thus influence the growth of the monolayers just as surface diffusion rates do. The endeavor of the system to settle into a global minimum of Gibbs free energy, i.e., reaching the thermodynamic equilibrium, will be discussed in the following section. Adsorption/desorption kinetics is the topic of the second section.

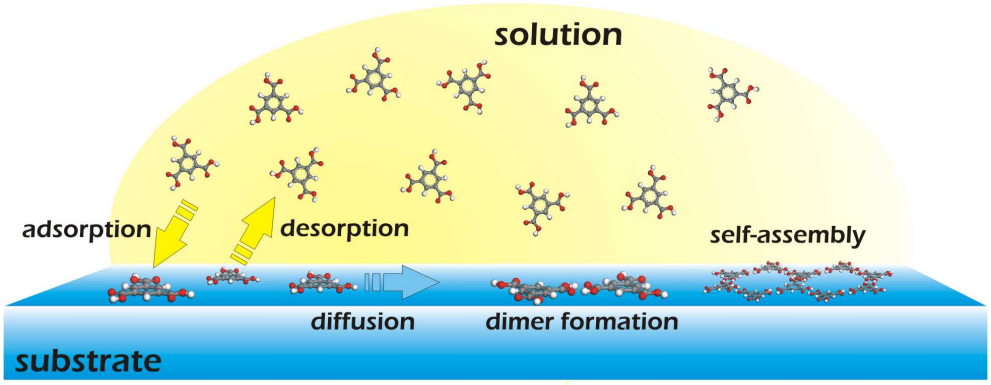

Figure 3.1 – Schematic model of molecular self-assembly at the liquid/solid interface. Molecules adsorb onto the surface (substrate) from solution and diffuse until desorbing or until encountering another molecule (dimerization). Attachment of further molecules to the nucleus result in growth of molecular domains, which subsequently coalesce into self-assembled monolayers. In equilibrium, the number of adsorbing molecules is balanced by the number of desorbing molecules.

3.1 Thermodynamics

Molecular self-assembly is usually a thermodynamically driven process. This means that under isobaric and isothermal conditions the system evolves towards a minimum in Gibbs free energy. A change in free energy ΔG can be decomposed into two contributions: change in enthalpy ΔH and change in entropy ΔS:

$$\Delta G = \Delta H - T\Delta S. \tag{3.1}$$

Here, T is the temperature of the system. Equation 3.1 provides a reasonable description of self-assembling systems, where a (local) minimum in Gibbs free energy corresponds to a (meta) stable state of the overall system. While changes in enthalpy can be computed more or less directly, entropy changes are not assessable in a straightforward manner. The following paragraphs describe one possible approach to a calculation of entropy change upon molecular self-assembly. When molecules self-assemble, entropy of the overall system decreases. This is due to a reduction of degrees of freedom for each assembled molecule, such as translational, rotational, vibrational, and conformational degrees of freedom. Nevertheless, although a decrease in entropy is not favorable in terms of Gibbs free energy, self-assembly still occurs as a spontaneous process. The diminishing entropy has to be compensated for by a reduction in enthalpy, mainly *via* the formation of molecular bonds due to intermolecular and molecule-substrate interactions. At the liquid/solid interface, an adsorbed but freely diffusing molecule on the surface looses part of its translational entropy upon aggregation. The same holds true for its rotational entropy. When fixed in a monolayer, the molecule looses all its translational and rotational entropy. On the other hand, the assembled molecules reduce the overall enthalpy of the system by optimizing molecular interactions with their neighbors and with the surface. These interactions stabilize the system energetically, and eventually lead to a reduction of Gibbs free energy. At the same time, the molecules which remain in solution are part of the whole system, too, and need to be considered in a complete thermodynamic descriptions. This implies that solvation enthalpy and entropy in the dissolved state also have to be accounted for. Likewise, solvent molecules might coadsorb on the surface, for example inside cavities of open-pore structures, and thus must be included into entropy and enthalpy calculations. For molecule-substrate systems under UHV conditions the situation is slightly simpler: as a good approximation, only adsorbed molecules need to be considered as the thermodynamic system, since no reservoir of molecules comparable to the dissolved molecules in solution is present. Adsorbed

molecules loose the same contributions to entropy as discussed for the liquid/solid interface, and similar bonding schemes contribute to the stabilization of the system *via* a decreasing enthalpy.

Changes in enthalpy in molecular self-assembly on surfaces, primarily due to adsorbate-adsorbate and adsorbate-substrate interactions, can be addressed for example by quantum chemical calculations. Although the effect of entropy on self-assembly cannot be neglected, as has been shown before,[36] no direct model is available to calculate it. However, a set of equations has been proposed which allows to estimate entropy losses upon self-assembly.[37,38] These equations were derived for molecular self-assembly in solution, but should be equally correct for self-assembly at interfaces. The overall entropy reduction is partitioned into translational, rotational, vibrational, and conformational entropy:

$$\Delta S_{\text{total}} = \Delta S_{\text{translation}} + \Delta S_{\text{rotation}} + \Delta S_{\text{vibration}} + \Delta S_{\text{conformation}} \tag{3.2}$$

Statistical mechanics text books help to derive equations for the different contributions from the partition function of a system of non-interacting particles. This leads to

$$\Delta S_{\text{translation}} = R \ln \left[\frac{e^{5/2}}{c} \left(\frac{\sqrt{2\pi m k_{\text{B}} T}}{h} \right)^3 \right] \tag{3.3}$$

for translational entropy, which is the Sackur-Tetrode equation. Here, h is Planck's constant, k_{B} the Boltzmann constant, R the gas constant, and T the absolute temperature. Euler's number is denoted by e , m is the solute's mass, and c is the solute concentration. As it turns out, the concentration of the solute in solution as measured in *molecules/volume* is not an adequate measure, since translational entropy is systematically overestimated. Whitesides and coworkers propose a free-volume model, in which the actual volume of the solution is reduced by an amount proportional to the volume which the solvent molecules occupy.[37] The resulting effective concentration is thus much higher, and translational entropy respectively lower. This approach seems to yield reasonable accordance of calculated translational entropy values with experimental data. For particles with finite dimension, i.e., non point-like particles, rotational entropy is likewise derived in textbooks and reads

$$\Delta S_{\text{rotation}} = R \ln \left[\frac{8\pi^2 e^{3/2}}{\gamma} \left(\frac{\sqrt{2\pi k_{\text{B}} T}}{h} \right)^3 \sqrt{I_1 I_2 I_3} \right]. \tag{3.4}$$

γ considers the symmetry of the molecule, and I_1, I_2, and I_3 are its principle moments of inertia. The fact that molecules can also vibrate is considered in $\Delta S_{\text{vibration}}$. The associated entropy loss is given by

$$\Delta S_{\text{vibration}} = R \sum_{\alpha} \left[\frac{h\nu_\alpha / k_{\text{B}} T}{e^{\frac{h\nu_\alpha}{k_{\text{B}} T}} - 1} - \ln \left(1 - e^{-\frac{h\nu_\alpha}{k_{\text{B}} T}} \right) \right] \tag{3.5}$$

as a sum over all vibrational modes α with frequency ν_α. Most molecular vibrational modes like bond stretches are likely not affected by self-assembly. Furthermore, the majority of intramolecular vibrations are of high frequency as compared to thermal energy, and thus contribute only negligible to entropy, especially in comparison to translational and rotational entropy. The effect of $\Delta S_{\text{vibration}}$ can hence be considered to be rather small. Most molecules studied by STM are small and rigid so that they do not posses the ability to significantly change their conformation. This results in $\Delta S_{\text{conformation}}$ being equal to zero. The two major contributions to entropy which change upon self-assembly are thus translational entropy $\Delta S_{\text{translation}}$ and rotational entropy $\Delta S_{\text{rotation}}$, and Equation 3.2 reduces to

$$\Delta S_{\text{total}} = \Delta S_{\text{translation}} + \Delta S_{\text{rotation}}. \tag{3.6}$$

The above equations help to estimate the entropy loss of the overall system when molecules adsorb from solution into a monolayer. In order to reach a minimum in Gibbs free energy, this loss has to be compensated for by a decreasing enthalpy, that is, favorable contributions from molecular interactions at the surface.
A different formalism which models the thermodynamics at the liquid/solid interface is offered by the groups of Lackinger, de Feyter, and Samorì.[39–41] The chemical potentials of the adsorbant in solution as well as in the monolayer are compared, and its difference related to Gibbs free energy. Self-assembly is a spontaneous process if the chemical potential in solution μ_{solution} is initially higher than the chemical potential in the monolayer $\mu_{\text{monolayer}}$. The change in free energy then reads

$$\Delta G = (\mu_{\text{monolayer}} - \mu_{\text{solution}}) \Delta n, \tag{3.7}$$

where Δn is the number of molecules adsorbed from solution into the monolayer. In equilibrium $\Delta G = 0$, which means that $\mu_{\text{monolayer}} = \mu_{\text{solution}}$. The chemical potentials depend on the number of molecules in the respective phase (i.e., $\mu_{\text{monolayer}} = \mu_{\text{monolayer}}(n)$ and $\mu_{\text{solution}} = \mu_{\text{solution}}(N - n)$ with N being the total number of dissolved molecules). For a given volume V of solution the number of solute molecule N yields the concentration $c = N/V$, and for an ideal solution the chemical potential can be written as

$$\mu = \mu_0 + RT \ln \frac{N}{V} = \mu_0 + RT \ln c = \mu(c). \tag{3.8}$$

Concentration dependencies of the monolayer morphology can usually be described along these lines. It is noteworthy that translational entropy $S_{\text{translation}}$ likewise depends on concentration and that a higher concentration results in a lower entropy penalty. This favors adsorption from solutions with high concentration. Higher concentrations also indicate higher chemical potential, which consequently facilitates the adsorption of a molecule from solution into the monolayer. The two descriptions in terms of entropy and chemical potential thus yield the same qualitative behavior. Thermodynamic equilibrium is reached once enough molecules are adsorbed from solution to equalize μ_{solution} and $\mu_{\text{monolayer}}$, so that $\Delta G = 0$.
For the adsorption of two different types of molecules 1 and 2 from solution in order to form binary monolayers, Equation 3.7 has to be rewritten as

$$\Delta G = \left[\mu_{\text{monolayer},1} - \mu_{\text{solution}}(c_1)\right] n_1 + \left[\mu_{\text{monolayer},2} - \mu_{\text{solution}}(c_2)\right] n_2 \tag{3.9}$$

with n_1 and n_2 being the number of adsorbed molecules of type 1 and 2, respectively. This approach has proven to describe adequately the relation between monolayer morphology (stochiometry) and relative concentrations c_1/c_2[39]. A large value of c_1/c_2 favors monolayers with a large number of molecules of type 1, while a small value induces the adsorption of more molecules of type 2. The ratio of concentrations c_1/c_2 is thus reflected in the relative number of adsorbed molecules 1 and 2 in the monolayer. De Feyter and coworkers propose a set of equations which allows to calculate relative coverages of two competing monolayer polymorphs formed by the same adsorbant.[40] In equilibrium, the chemical potentials are related as (also compare Equation 3.9 for $\Delta G = 0$)

$$l\mu_{\mathrm{l}} = h\mu_{\mathrm{h}} + (l-h)\mu_{solution}. \tag{3.10}$$

The indices h and l denote each one type of polymorph, and the factors h and l are the number of molecules adsorbed in the respective polymorph. In addition to Equation 3.10, they postulate that the chemical potentials of molecules in one polymorph can be calculated using

$$\mu_l = \mu_{0,\mathrm{l}} + RT \ln Y_{\mathrm{l}} \text{ and } \mu_{\mathrm{h}} = \mu_{0,\mathrm{h}} + RT \ln Y_{\mathrm{h}}, \tag{3.11}$$

where Y_{l} and Y_{h} are the fractions of the monolayer area occupied by the respective polymorph. After some calculus, this leads to

$$\frac{Y_{\mathrm{h}}}{Y_{\mathrm{l}}^{(l/h)}} = \exp\left[\frac{(\mu_{\mathrm{solution}} - \mu_{0,\mathrm{h}}) - \frac{l}{h}(\mu_{\mathrm{solution}} - \mu_{0,\mathrm{l}})}{k_{\mathrm{B}}T}\right] c^{(1-\frac{l}{h})}, \tag{3.12}$$

which describes the relative coverage of both polymorphs as a function of concentration and temperature. Equation 3.12 points out the importance of temperature on the self-assembly and polymorph selection process: at higher temperatures, that polymorph is favored which has the higher chemical potential. A control of temperature allows to tune relative coverages in systems where two or more different polymorphs are similar in free energy. The observation of coexistence of two polymorphs over a wide range of concentrations is actually related to similar free energies of both polymorphs.[40] If one polymorph was energetically much more stable at a given concentration than the other, solely the former structure would be observable at the surface. Similar free energies, on the other hand, allow for coexistence of polymorphs. Despite various theoretical attempts to predict the morphology of a self-assembled monolayer for a given molecule in a specific solvent, no exact model is available. Many crucial factors contribute to the self-assembly process which complicate a simple description. However, thermodynamic descriptions are getting more and more sophisticated and in general provide the right trends in polymorph selection at least for special cases of molecular self-assembly.

3.2 Kinetics

Interfacial self-assembly of molecules is a time dependent process which does not occur instantaneously.[42] It takes a certain amount of time before surface-coverage reaches its equilibrium state. This equilibration time is governed by a variety of parameters like adsorption and desorption rates. At the liquid/solid interface, for example, the adsorption of molecules is limited by diffusion of molecules in the bulk solution towards the surface. Also, not all molecules in the proximity of the surface possess an energy high enough to surmount a possible adsorption barrier. Finally, the on-surface diffusion rate plays an important role in reaching an equilibrium state of the monolayer. A balance between adsorption rate A and diffusion rate of molecules on the surface D is thus responsible for the formation of different structures.[12,26] For small ratios A/D, molecules are free to explore the energy landscape of the surface before eventually binding in the most favorable geometry/arrangement to another molecule. Nucleation is slow, and the resulting structure is thermodynamically controlled since sufficient time enables molecules to relax into their energetically preferable state. In the inverse situation, for large ratios A/D, nucleation of thermodynamically not optimal structures may result due to the high rate by which new molecules are added to the structure. In vacuum, this means that sublimation rate and substrate temperature are the two predominant experimental parameters. High fluxes of molecules result in high adsorption rates, just as a low surface temperature does. Surface diffusion, and thus the mobility of the molecules, strongly depends on temperature. At the liquid/solid interface, on the other hand, the amount of molecules impinging onto a surface depends on the concentration of solute in solution and on the solute's mobility.

At the vacuum/solid interface the adsorption rate is defined as the product of the flux of molecules from the deposition source and the sticking coefficient of molecules on the surface. Molecules once adsorbed on the surface stay there until they desorb with a typical desorption rate, meaning that they are lost into the vastness of vacuum. The desorption rate, which depends on the size of the molecule, temperature, and desorption barriers, seems to be rather small for sufficiently large molecules. This circumstance permits the imaging of monolayers under vacuum conditions. At the liquid/solid interface the situation is more complicated: adsorption is governed by the amount of molecules in the proximity of the surface, and is thus directly dependent on the concentration in solution. Adsorption induces a decrease in local concentration in a layer close to the surface (interfacial layer), followed by diffusion from the bulk solution into this layer in order to equilibrate concentration. Subsequent adsorption

on the surface is thus limited by the rate at which molecules are supplied to the interfacial layer. In general, the time evolution of the surface coverage θ of interacting particles reads as follows:[43]

$$\frac{\partial\theta}{\partial t} = k_\mathrm{a} c_\mathrm{int}(1-\theta) - k_\mathrm{d,0}\theta \exp\frac{U(x)}{k_\mathrm{B}T} + \frac{\partial}{\partial x}\left[\frac{D}{k_\mathrm{B}T}\frac{\partial U(x)}{\partial x}\theta(1-\theta) + D\frac{\partial\theta}{\partial x}\right]. \tag{3.13}$$

Here, c_int is the solute concentration in the interfacial layer, k_a the adsorption constant, $k_\mathrm{D} = k_\mathrm{d,0}\exp\left[U(x)/k_\mathrm{B}T\right]$ the desorption constant, and $U(x)$ the interaction potential of the molecules at the surface, with x representing the spatial coordinates describing the plane of the surface. The existence of the spatially varying potential induces a force $F = -\partial U(x)/\partial x$, which results in a flow of adsorbed particles on the surface. In addition, a difference in local coverage produces a diffusional flow. These two flows account for the term in square brackets in Equation 3.13. Assuming non-interacting particles, $U(x) = 0$, and uniform (spatially homogeneous) coverage, $\partial\theta/\partial x = 0$, Equation 3.13 reduces to

$$\frac{\partial\theta}{\partial t} = k_\mathrm{a} c_\mathrm{int}(1-\theta) - k_\mathrm{d,0}\theta, \tag{3.14}$$

which yields as a solution in equilibrium with $\partial\theta/\partial t = 0$ the Langmuir adsorption isotherm

$$\theta = \frac{1}{1 + (\frac{k_\mathrm{d,0}}{k_\mathrm{a} c_\mathrm{int}})}. \tag{3.15}$$

It is clear from the above equations that the concentration close to the interface c_int is a coverage determining parameter, and that the rate by which molecules from the bulk solution far away from the interface are delivered to the interfacial layer is of great importance. Furthermore, not necessarily all molecules which imping onto the surface are adsorbed when an adsorption activation barrier acts against adsorption. For physisorption, i.e., weak adsorption, no activation barrier is present. Chemisorbed molecules, on the other hand, might have to overcome such an activation barrier. A potential adsorption barrier can be included as a parameter into the adsorption constant k_a. The higher the barrier, the lower k_a and vice versa. In consequence, only those molecules adsorb whose energy (kinetic and internal degrees of freedom)

is sufficient to surpass the barrier, and hence are able to form a nucleus for further growth of the monolayer. Physisorption will be characterized by rather large k_a as compared to activated chemisorption.
In the early stages of monolayer formation, the concentration close to the interface c_int is smaller than the bulk concentration c. As stated above, the concentration of solvent in the interfacial layer is reduced due to adsorption. The balance of the concentration with solute molecules from the bulk is given by Fick's law of diffusion:

$$\frac{\partial c(z)}{\partial t} = d\frac{\partial^2 c(z)}{\partial z^2}, \tag{3.16}$$

where d is the diffusivity constant of the solute molecule in the bulk solvent, and the coordinate z points along the surface normal. The resulting flux F towards the surface is given by[44]

$$F = -d\frac{\partial c(z)}{\partial z}, \tag{3.17}$$

and depends on the concentration gradient perpendicular to the surface. The evolution of the local concentration in the interfacial layer is therefore limited by the flux of particles towards the surface, which itself depends on the diffusivity in solution. Solving Equation 3.8 for c, differentiating with respect to z and inserting in Equation 3.17 yields

$$F = -\frac{dc}{RT}\frac{\partial \mu}{\partial z}. \tag{3.18}$$

The flux F of molecules delivered to the interfacial layer is driven by a gradient in the chemical potential perpendicular to the surface. This gradient is built up by a difference in chemical potential of the interfacial layer with respect to the bulk solution, and it is non-zero until the monolayer growth has been completed. This formula allows to take into account the effect of solvent viscosity η on self-assembly by considering the Stokes-Einstein equation for the diffusivity d

$$d = \frac{k_\mathrm{B}T}{6\pi r\eta}, \tag{3.19}$$

where the solute molecule is approximated by a sphere of radius r. Consequently,

$$F \propto \frac{c}{\eta}\frac{\partial \mu}{\partial z}. \tag{3.20}$$

High bulk concentrations and low solvent viscosities result in a high flux of adsorbant molecules towards the surface. A low flux, as a consequence of a low diffusivity and high solvent viscosity, may hamper the formation of a particular polymorph in favor of another. In this case, the resulting polymorph would be kinetically controlled and would not necessarily correspond to the thermodynamically most stable state. For example, Matzger and coworkers report on the formation of a self-assembled monolayer at the liquid/solid interface, which given sufficient equilibration time transforms into a different polymorph.[45] The quickly forming polymorph seems to have a larger nucleation/growth rate, but is not necessarily the thermodynamically stable one. After some time, the slower growing and energetically more stable polymorph forms, and eventually covers the whole surface. This finding underlines the importance of kinetics in monolayer growth and exemplifies that an interpretation of self-assembly in terms of thermodynamics is not always sufficient. Equation 3.20 together with Equation 3.19 also points out that the adsorbant's size might be important in molecular self-assembly from solution. The larger the molecule, the slower it moves in solution, and the lower is its adsorption rate. This might be of importance in coassembly of two molecules of different sizes from the same solution.
Many kinetic parameters like on-surface diffusivity constants of the adsorbant, bulk solution mobility of the solute, and adsorption and desorption rates are of significance in molecular self-assembly. It is therefore important to understand in which way and to what extend each of the above described parameters influences a given system, and not to restrict the interpretation of experimental results merely to thermodynamic considerations.

Chapter 4

Molecular Self-Assembly

Self-assembly of molecules depends on various parameters. These can be separated into two different sets: internal and external parameters. Geometry* and functionalization† of a molecule can be attributed to the internal parameters since they are inherent to the building block constituting the final self-assembled structure. Additional characteristics and properties of a single molecule can be added to this category. The environment in which self-assembly takes place defines the external parameters. These include temperature, deposition mechanism (OMBE in vacuum or adsorption from solution), deposition rate, the type of surface, type of solvent, and solute concentration. Further external parameters can contribute to this list, like external electric or magnetic fields, which will not be discussed here. However, in many cases the division into two separate types of parameters appears too strict, and interferences can occur, i.e., the importance of an internal parameter can depend on an external parameter. The promotion or hindering of certain molecular interactions by a certain choice of solvent is an example for the interaction of external and internal parameters. The following sections describe parameters which were found to decisively influence self-assembly of molecules on surfaces.

*Here, the geometry of a molecule refers to the arrangement of its atoms in space. The geometry of a molecule thus implies its point group. This is intentionally separated from the term "(chemical) structure", which presumes special functions (interactions) of atoms or groups of atoms.

†Functionalization includes all chemical properties of a molecule which are not represented by its geometry.

4.1 Molecular Building Blocks

Molecules are the basic building units of the self-assembled monolayers presented in this work, and encode an important part of information about the morphology of the monolayer. The information is primarily present in their geometry and in their functional groups facilitating molecular interactions. Therefore, altering these parameters of a molecule allows to tune the monolayer morphology (see for example [41,46–49]). Crystal engineering in two dimensions is hence not much different to the engineering of three dimensional bulk crystals of organic molecules, where the properties of the molecules dictate their arrangement, symmetry, and unit cell parameters of the crystal. However, 2D crystals show a reduced number of possible arrangements of molecules within unit cells as compared to 3D crystals. This is due to the reduced dimensionality and related to the fact that the number of space groups in 2D (17) is greatly reduced as compared to 3D (230).

A series of experiments has shown that supramolecular open-pore networks can be synthesized by self-assembly of tricarboxylic acids with threefold symmetry.[29] The pore size of the network is closely related to the lateral extension of the molecule and increases with the size of the molecule. As depicted in Figure 4.1, molecules with identical symmetry and functionalization but increasing size assemble in isostructural monolayers with increasing pore size. Trimesic acid (TMA), as the smallest of the molecules, forms hexagonal networks with a lattice parameter of 1.7 nm (Figure 4.1 a), while the homologous molecules 1,3,5-benzenetribenzoic acid (BTB) and 4-{2-{3,5-bis[2-(4-carboxyphenyl)-1-ethynyl]-2,4,6-trimethyl-phenyl}-1-ethynyl} (MeCPEBA) form networks with lattice parameters of 3.2 nm (Figure 4.1 b) and 4.1 nm (Figure 4.1 c). All three molecules adsorb planar on the graphite surface, facilitating hydrogen bonds with neighboring molecules through their carboxylic groups. Each vertex of the hexagonal network is formed by one molecule, so that six molecules complete one hexagonal unit. The information about the monolayer encoded in the molecule is its size, and changing this characteristic of the molecule while keeping its functionalization constant means programming it to form a different monolayer. However, competing molecular interactions can hamper the formation of a monolayer of anticipated and desired morphology, and careful design of the molecular building block is necessary. This illustrates that information is encoded not only in the geometry of a molecule, but also in its functionalization. An example of how the balance between hydrogen bonds and aromatic interactions of a molecule influences self-assembly is described in the next section.

All three molecules, TMA, BTB, and MeCPEBA were used in different studies prob-

ing different parameters of molecular self-assembly. TMA dissolved in phenyloctane as solvent was used to show that depending on the preparation of the solution a structure with unusual high packing inside the 2D crystal can be created (*cf.* List of Publications, publication number 4). The hexagonal structure of BTB was observed at the liquid/solid interface in experiments which were mainly concerned with the effect of temperature on self-assembly (publication number 5). It was shown that one can reversibly switch between two different polymorphs of the monolayer by changing the temperature. The molecule MeCPEBA was used as a reference to a similar molecule, investigating relative strengths of different molecular interactions. The results are presented in publication number 1 (see also the following section).

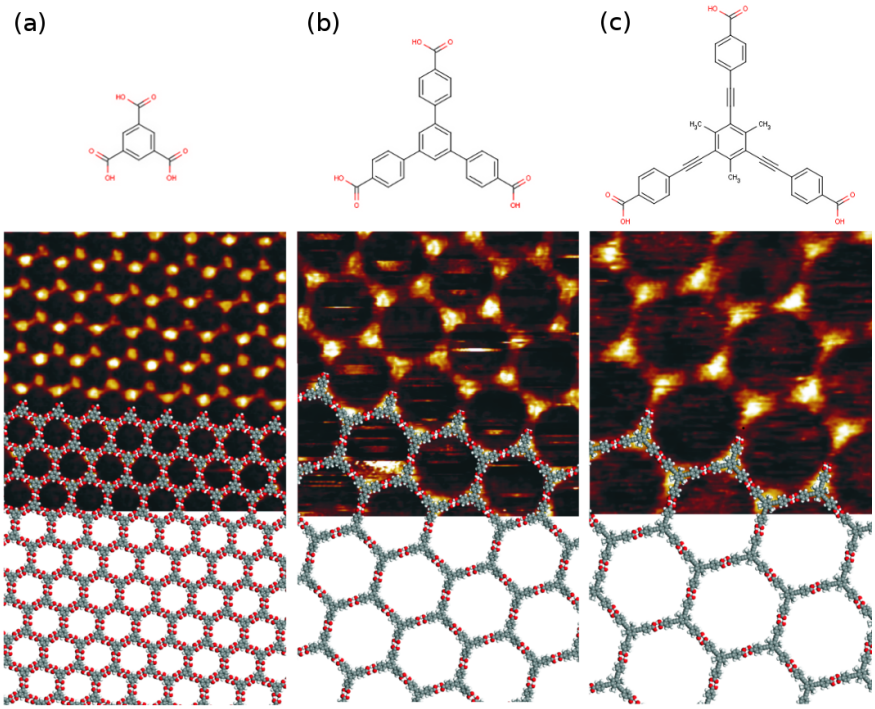

Figure 4.1 – Molecular models (upper row), and STM topographs of hexagonal open-pore networks with overlayed models. (a) TMA with a lattice parameter of 1.7 nm , topograph 13 × 13 nm^2 (b) BTB with a lattice parameter of 3.2 nm , topograph 13 × 13 nm^2 (c) MeCPEBA with a lattice parameter of 4.1 nm , topograph 12 × 12 nm^2 All images were acquired at the nonanoic acid/graphite interface.

4.2 Intermolecular Bonds

Similarly important as the geometry of the molecule are mutual molecular interactions. Supramolecular self-assemblies are usually stabilized by relatively weak bonds, which include van der Waals bonds[47,50,51], hydrogen bonds[29,52–55], and aromatic in-

teractions.[56–60] Likewise, metal-organic bonds[11,61], electrostatic[62], and substrate mediated interactions[63,64] can be the stabilizing forces in the formation of monolayers.

The competition between hydrogen bonds and aromatic interactions can be exemplified by two similar molecules: MeCPEBA, which forms hexagonal networks (see Figure 4.2 c), and 4-{2-{3,5-bis[2-(4-carboxyphenyl)-1-ethynyl]phenyl}-1-ethynyl}benzoic acid (CPEBA, Figure 4.2 a). The only difference between these two molecules are three methyl groups on the 2,4, and 6 positions of the inner phenyl ring of MeCPEBA, whereas CPEBA is saturated at these positions with hydrogen. Adsorption of CPEBA from the same solvent (nonanoic acid), under the same conditions which favor the formation of the hexagonal network from MeCPEBA, yields a completely different structure in STM topographs (Figure 4.2 b). The emerging row structure of CPEBA can be explained by a stacking of molecules along the rows in a non-planar manner, i.e., with their molecular planes not aligned parallel to the surface. Each molecule adsorbs in a tilted edge-on arrangement on the graphite forming an angle of roughly 35°with the surface. The extended electronic π-systems of the planar molecules are stabilizing the row structure *via* aromatic interactions. Lateral interrow stabilization by two O−H···O hydrogen bonds is feasible. In contrast, the aromatic stacking interaction is sterically hampered by the bulky methyl groups in MeCPEBA, which do not allow the π-orbitals to interact in a favorable way. Face-to-Face interactions of MeCPEBA molecules is diminished due to the methyl groups, and planar adsorption of MeCPEBA on the surface is enforced by suppression of aromatic interactions. It is interesting to observe that a slight structural modification not affecting the functional groups of a molecule can lead to a drastic change in morphology of the corresponding monolayer.

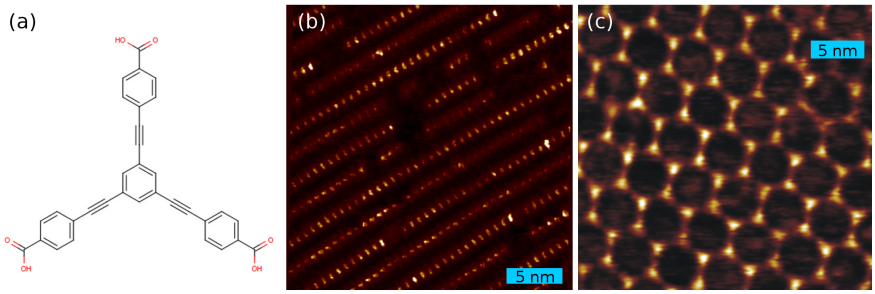

Figure 4.2 – STM topographs of two akin molecules assembling into two morphologically completely different monolayers: CPEBA (model in (a)) self-assembles into a row structure with non-planar adsorption (b). In (c), MeCPEBA (see Figure 4.1 c) forms a hexagonal network. While the row structure is stabilized by aromatic interactions, hydrogen bonds interlink molecules in the hexagonal structure.

Yet another parameter which influences the self-assembly of CPEBA is the type of solvent, as detailed in publication number 1 and section 4.5. The comparative study of MeCPEBA and CPEBA in publication 1 also shows that π-stacked molecular aggregates of CPEBA are likely to form already in solution, not just at the surface.

4.3 Reversibility of Bonds

All molecular networks at the liquid/solid or the vacuum/solid interface are stabilized by some kind of intermolecular bond, and in many cases, especially in supramolecular chemistry, these bonds are rather weak. Networks crosslinked by weak interactions can be stable at room temperature, but a rupture of intermolecular bonds might be achievable if the binding energy is not too large. This results in reversibility of the intermolecular bonds, which in consequence leads to the possibility of detachment of molecules from the network. As a result, a route is opened for error-correction within the network: a defect in the monolayer can easily be healed by detachment of misplaced molecules, the rearrangement of the network into an energetic minimum, and a subsequent reattachment of additional molecules in the correct topology. Usually, energetic minima correspond to ordered structures. The long-range order commonly observed in self-assembled molecular networks can be attributed to the intrinsic possibility of error-correction based on the reversibility of the molecular bonds. On the other hand, when intermolecular bonds become too strong, the error-correcting mechanism is not operational anymore. This happens for example in the covalent coupling of on-surface generated radicals of molecules, where the covalent bond is much stronger than the above cited interactions. Once covalent bonds in a network of molecules are formed, thermal energy is not sufficient to cleave these bonds, and a disordered network remains disordered. Error-correction of covalent bonds requires temperatures at which organic molecules are no longer stable. Temperature is thus a parameter that allows to control the error-correction mechanism, which can be suppressed at low temperature.

An example which illustrates the necessity of bond reversibility in order to form networks with long-range order are the molecules BTB and 1,3,5-tris(4-bromophenyl)benzene (TBB, Figure 4.3 c). TBB is isostructural to BTB with the outer carboxylic groups replaced by three bromine atoms. When BTB is evaporated onto a graphite surface at room temperature, a hexagonal network with long range order is formed with few defects (Figure 4.3 a). This situation is completely altered when TBB is evaporated under the same conditions onto a Cu(111) surface (Fig-

ure 4.3 b). Due to the catalytic properties of the surface, the bromine atoms are cleaved homolytically from the molecule, leaving the triple radicals free to form metal-organic bonds with accessible copper adatoms provided by the surface. The resulting metal-organic network, where two radicals share one metal atom, shows an open-pore structure, but without long range order. Pores can be constituted by as little as four molecules up to eight molecules, while long range order would require uniformly four or six molecules per pore. A reorganization of the adsorbed molecules is inhibited by the strength of the phenyl radical-copper atom bond, which is mainly covalent in nature. A comparison of these room temperature experiments exemplifies how important a self-repair mechanism in molecular self-assembly is: molecular interactions whose energetic strength is large compared to thermal energy are not reversible and hinder the formation of ordered structures.

However, random and glassy networks without long range order can also assembly when bond-reversibility is present.[65–69]

TBB was used in a study on on-surface polymerization of organic molecules. While Figure 4.3 b stems from this study, Figure 4.3 a is an unpublished topograph (courtesy of Hermann Walch). The influence of substrate type and temperature on polymerization reactions on surfaces is presented in publications number 2 and 6.

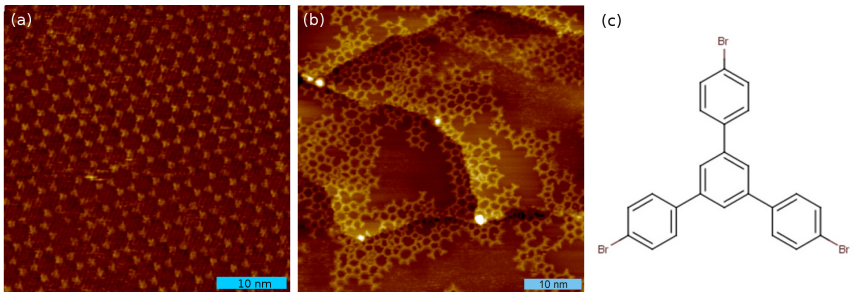

Figure 4.3 – STM topographs of (a) BTB and (b) TBB. Weak molecular bonds like hydrogen bonds allow for the formation of ordered monolayers like those of BTB (*cf.* Figure 4.1 b) on graphite in UHV (a). TBB (model in (c)) after dehalogenation on Cu(111) assembles into disordered structures (b), which are stabilized by much stronger metal-organic bonds.

4.4 Temperature

Temperature is one of the most important, yet one of the least studied parameters in self-assembly at the liquid/solid interface. Its significance becomes clear from Equation 3.2 and Equation 3.8, which both depend on temperature. High temperatures favor states of a system with high entropy and can shift the relative chemical po-

tentials of molecules in different phases. Likewise, it influences the reaction kinetics. Examples for temperature dependence include annealing effects in thiol-based monolayers[70–73], sample preparation and measurement at elevated temperatures,[41,74–76] and irreversible phase transitions in supramolecular self-assembly.[77,78] At the liquid/solid interface, the above discussed molecule BTB shows a reversible phase transition between two polymorphs when assembling from solutions of three different types of carboxylic acids (heptanoic, octanoic, and nonanoic acid). At low temperatures (25°C) in heptanoic acid, the smallest of the three solvent molecules, a polymorph with row-like appearance is observed in STM topographs (similar to Figure 4.4, right image). In octanoic acid, the row polymorph coexists with the hexagonal structure (*cf.* left image Figure 4.4). In nonanoic acid, only the hexagonal structure exists. Heating the system results in a transition from the row to the hexagonal structure in octanoic acid at about 43°C , whereas the same transition occurs in nonanoic acid at about 52°C The transition can be explained be a detailed analysis of both contributors to free energy of the respective phase, namely enthalpy and entropy. Adsorbed BTB molecules and coadsorbed solvent molecules increase the overall entropy of the system while decreasing its enthalpy. It is plausible that desorbing coadsorbed solvent molecules at elevated temperatures destabilize the hexagonal phase and favor a transition to the row structure.

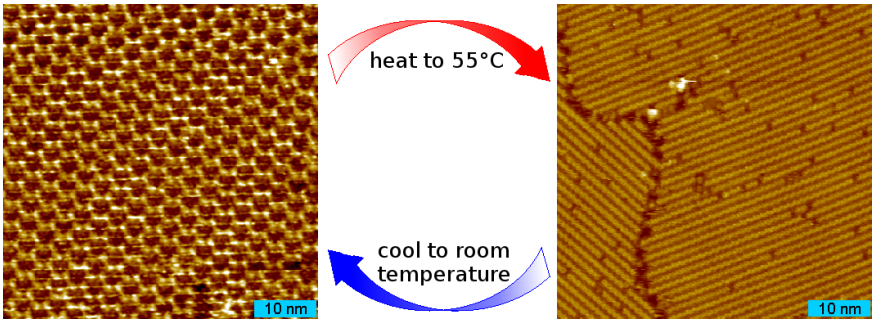

Figure 4.4 – STM topographs of BTB at the nonanoic acid/graphite interface acquired at room temperature (left) and at 55°C (right). The phase transition from the hexagonal phase to the row structure is reversible.

Temperature dependent phenomena can also be observed under UHV conditions.[79–83] In many cases, sublimation of molecules onto a cooled surface results in the formation of monolayers with different morphology than those which form at room temperature. These low-temperature phases are usually kinetically trapped in metastable states. A certain amount of energy input is required to surmount the kinetic barrier to induce a phase transition to a more stable phase. Post-deposition annealing or evaporation onto heated surfaces are suitable methods to induce phase transitions. The molecule TBB sublimed onto Ag(111) held at 80K assembles into a

network with hexagonal unit cell. Annealing the sample to room temperature results in a phase transition which is not reversible, so that imaging the annealed surface shows an altered morphology of the monolayer (*cf.* Figure 4.5 (topograph (b) was recorded at 80K to ensure higher drift stability of the STM)). Since the number of molecules on the surface does not change upon annealing, the difference in entropy between both phases is presumably small, although the less ordered high temperature phase is likely to have a higher entropy. The phase transition can also be explained by a decrease in enthalpy, i.e., by an optimization of molecular interactions. The high temperature phase is thermodynamically more stable as indicated by the irreversibility of the transition. The preferred formation of the low-temperature phase might be due to kinetic barriers which hinder the assembly into the thermodynamically stable phase, possibly a result of low on-surface diffusivity.
The importance of temperature on molecular self-assembly at the liquid/solid interface is exemplified for BTB in publication number 5. This study also includes a discussion of the influence of solvent and concentration. The UHV results on temperature dependence depicted in Figure 4.5 constitute part of the studies of polymerization on surfaces (number 2 and 6).

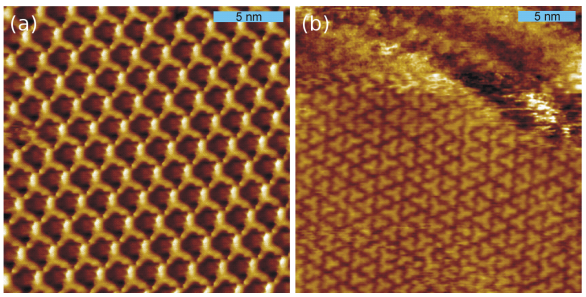

Figure 4.5 – STM topographs of TBB imaged (a) as deposited onto a cooled Ag(111) surface (80K), and (b) after annealing to room temperature. The phase transition from an ordered hexagonal to a less ordered polymorph is not reversible, and the high temperature phase prevails upon cooling.

4.5 Solvent

Solvent effects have been widely studied in solution based molecular self-assembly, and it is commonly reported that different solvents can induce the formation of different polymorphs (see for example[47,84–90] and[28] for a review). Solubility of the solute in a particular solvent plays an important role, but also other parameters like viscosity influence self-assembly. Up to now, no conclusive theory exists which explains the solvent's influence. It is likely that it can be broken down to thermodynamic parameters

like solvation enthalpy, hydrophobic forces, affinity of solvent molecules to the substrate, or kinetic parameters like viscosity and thus mobility of the solute in solution. Again, BTB can serve as an illustrative example: when adsorption takes place from heptanoic acid, the above discussed row structure is formed (Figure 4.6 a). Nonanoic acid as solvent, on the other hand, yields the hexagonal network (Figure 4.6 c). As an intermediate case, self-assembly from octanoic acid results in the coexistence of both polymorphs (Figure 4.6 b). Although the structural difference in the homologues heptanoic, octanoic, and nonanoic acid seems rather small and only consists in one additional methylene group (chemical formulas read $C_6H_{13}COOH$, $C_7H_{15}COOH$, and $C_8H_{17}COOH$, respectively; see Figure 4.7 a for a model of nonanoic acid), the impact on the characteristics of the solvents, and consequently on self-assembly, cannot be neglected.

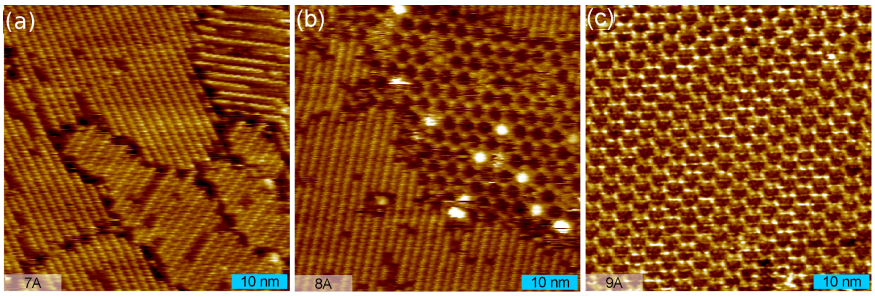

Figure 4.6 – STM topographs of BTB dissolved in carboxylic acids: (a) Saturated heptanoic acid solution favors assembly of the row structure. (b) A hexagonal structure coassembles from octanoic acid solution. (c) In nonanoic acid, only the hexagonal structure is observable.

Depending on the solvent, CPEBA likewise assembles either in a row structure or in a hexagonal structure. Nonanoic acid and 3-phenylbutyric acid (Figure 4.7 a and b) promote assembly into the row structure (Figure 4.7 e), while 1,3-dibromobenzene and 1,2,4-trichlorobenzene (Figure 4.7 c and d) yield the hexagonal phase (Figure 4.7 f). Solute-solvent interactions are likely responsible for this behavior: the first two solvents interact mainly by hydrogen bonding with CPEBA, which allows for aromatic stacking of the solute in solution and a non-planar adsorption on the surface. The resulting stacks are stabilized by an interaction of the extended electronic π-systems of the molecules. The latter two solvents do not posses the necessary functional groups, and thus the ability, to interact *via* hydrogen bonds. Instead, an interaction of the solvent's and solute's π-electrons is favored. As a result, the stacking of CPEBA is inhibited, and the molecules adsorb in a planar manner on the surface, affording the hexagonal network stabilized by hydrogen bonds.

Yet a last example is MeCPEBA when adsorbing from carboxylic acids as solvents. Heptanoic, octanoic, as well as nonanoic acid favor the formation of the same oblique

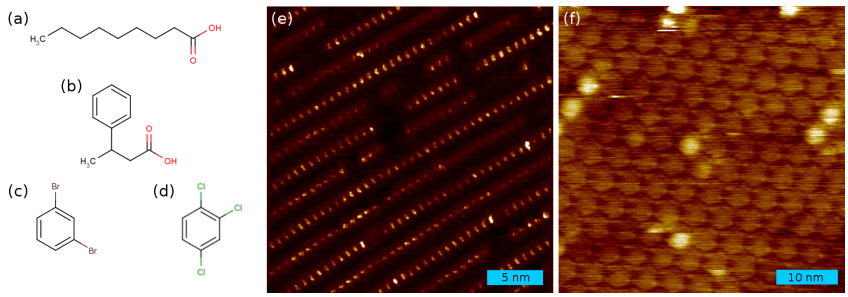

Figure 4.7 – Schema of solvents: (a) nonanoic acid, (b) 3-phenylbutyric acid, (c) 1,3-dibromobenzene, and (d) 1,2,4-trichlorobenzene. STM topographs of (e) CPEBA in nonanoic acid showing the monolayer comprised of molecular rows and (d) CPEBA in 1,2,4-trichlorobenzene with a hexagonal arrangement of molecules.

structure (*cf.* Figure 4.8 a for an STM topograph recorded in nonanoic acid). Here, nonanoic acid solutions represent a special case: various polymorphs can be observed in coexistence at the same interface. The formation of the previously described hexagonal network (Figure 4.8 c) is accompanied by the formation of the oblique structure and another densely packed structure (Figure 4.8 b). Thus, one and the same solvent can lead to self-assembly of molecules into different polymoporphs, which can also be observed for BTB upon dilution of a heptanoic acid solution (*vide infra*). Although the reasons for this finding are not fully understood, concentration effects, viscosity, or solvent coadsorption may be held responsible for the solvent induced polymorphism. The first of the discussed cases of BTB at the carboxylic acid/graphite interface is part of publication 5. The second example, CPEBA *vs.* MeCPEBA, is one of the main findings which led to publication 1. Both solute/solute and solute/solvent molecular interactions are found to be important, not just the interplay of the adsorbed species at the interface (*cf.* section 4.2). Topographs (a) and (b) of Figure 4.8 are unpublished and were acquired during the experiments leading to publication 1.

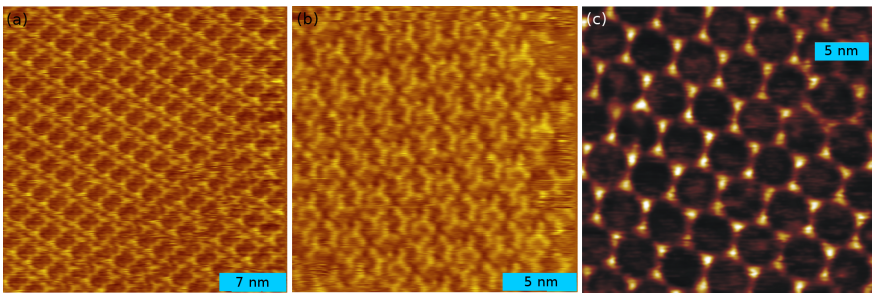

Figure 4.8 – STM topographs of self-assembled monolayers of MeCPEBA in nonanoic acid. (a) Oblique structure with rectangular pores. The same polymorph of MeCPEBA can be observed with heptanoic acid and octanoic acid solutions. (b) Close-packed structure without pores. (c) Hexagonal open-pore network.

4.6 Concentration

As a general trend it is reported that high solute concentrations yield more densely packed structures during self-assembly on a surface than low concentrations.[40,49,91] The solute's concentration in solution is therefore reflected in the interface concentration of the adsorbate. Observations of the BTB in heptanoic acid/graphite interface are in accord with these findings: saturated solutions favor the adsorption in the row structure, thereby maximizing the number of molecules adsorbed on the surface. Lowering the concentration to 50% saturation results in the coexistence of the row structure with the hexagonal structure. Upon further dilution to 10% saturation the hexagonal structure is observed predominantly (Figure 4.9). Detailed models describing the concentration dependence are given in chapter 3.
The observations described above on concentration dependence are part of publication number 5. This publication also covers how polymorph selection by changing concentration is related to the influence of the type of solvent (*cf.* section 4.5). The main topic of the publication is the influence of temperature, which allows to switch between one polymorph and the other. Thus, three parameters (solvent, concentration, and temperature) can be used to influence the morphology of the monolayer, which underlines the complex interplay between external influences on molecular self-assembly.

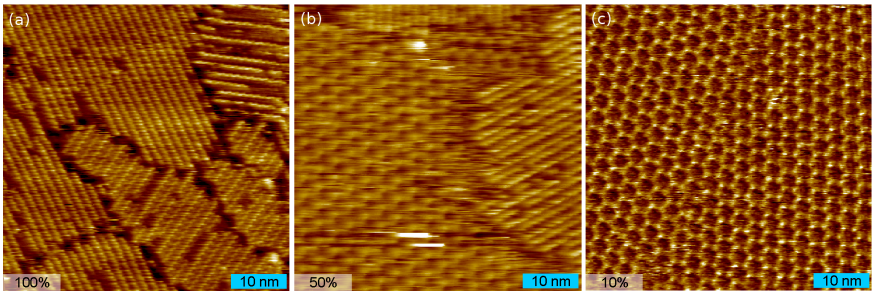

Figure 4.9 – (a) STM topograph of BTB monolayer on graphite assembled from saturated heptanoic acid solution. Exclusively the row structure is observed. (b) 50% saturated solution. Row and hexagonal structure coexist. (c) 10% saturated solution. Almost solely the hexagonal network is formed.

4.7 Vacuum/Solid Interface

The primary reason why experimentally challenging ultra-high vacuum studies cannot be neglected as a complementary method to experimentally simpler solution/solid studies is the feasibility of samples which cannot be prepared and treated under ambient conditions. This includes the preparation of a great variety of clean and atomically flat metal surfaces in UHV, whereas ambient studies are mostly performed on rather inert substrates like graphite(001), Au(111), or MoS_2(001). Further advantages of UHV experiments are variable temperature studies over a wide temperature interval (from $\sim$ 1000K down to mK), which includes the possibility to image single molecules and probe surfaces/interfaces/single molecules by STS. However, the extension of the accessible number of substrates is accompanied by further experimental modifications: molecular self-assembly on surfaces in vacuum by means of molecular beam deposition is substantially different from its analogue in solution. While in the latter case a dynamic equilibrium between adsorbed and soluted molecules crucially influences the structure formation and dynamics at the surface, deposited molecules at the vacuum/solid interface usually remain at the surface, especially if stabilized by incorporation into a supramolecular structure. No adsorption/desorption equilibrium dynamically stabilizes the structure, and also self-healing mechanisms are restricted. Although both environments are completely different, the morphology of many monolayers seems to be similar in vacuum and in solution. This points towards a substantial influence of the building block's intrinsic parameters on self-assembly. An example is the molecule BTB, which at the nonanoic acid/graphite interface assembles into the hexagonal open-pore structure (Figure 4.10 a), just like at the vacuum/graphite interface (Figure 4.10 b). BTB molecules adsorb planar onto the surface and two neighboring molecules interact with their carboxylic groups stabilizing the structure *via* hydrogen bonds. These observations underline the importance of the internal parameters like molecular geometry and intermolecular interactions, which allow for the self-assembly into the same structures in completely different environments. Nevertheless, it cannot be generalized that both preparation methods for molecular monolayers must always show the same morphology. TMA at the liquid/graphite interface assembling from carboxylic acids as solvents usually forms one of two different polymorphs.[84] This is in contrast to UHV experiments on Au(111), where sublimed TMA molecules assemble in a multitude of different polymorphs. These include those polymorphs observed at the liquid/solid interface, and are shown to depend on the surface concentration of molecules (although the influence of the substrate might also be

relevant).[92] Yet other studies with different molecules discuss similarities between deposition from solution or under UHV conditions.[93]

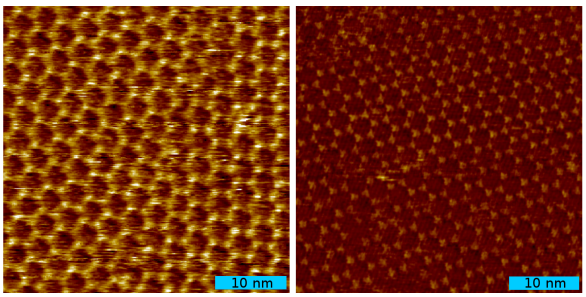

Figure 4.10 – (a) STM topograph of BTB assembled from diluted heptanoic acid solution onto graphite. (b) The same hexagonal structure can also be observed in vacuum, when sublimed onto graphite *via* OMBE

4.8 Substrate

The influence of the substrate is best probed at the vacuum/solid interface, for the number of available clean and easily prepared substrates under ambient conditions is quite limited (dominantly graphite, rather seldom Au(111) or MoS_2). Variations in adsorbate-substrate interactions and anisotropic diffusion account for a different assembly behavior on different surfaces. Also, electronic interactions between surface states and molecular orbitals might govern molecule-substrate interactions and thus self-assembly. An extreme case of substrate-dependent self-assembly is given for surface-induced chemical reactions in the adsorbate, which change the molecular structure and enhance or hinder certain molecular interactions. TBB adsorbed on inert graphite surfaces self-assembles into well-ordered domains of 2D molecular crystals (Figure 4.11 a). This is explained by an adsorption of intact TBB molecules on graphite and subsequent assembly, where molecule-molecule interactions dominate and stabilize the structure by weak halogen-halogen or halogen-hydrogen interactions. Similar experimental conditions but exchanging graphite for Ag(110) results in the assembly of porous networks with no long-range order (Figure 4.11 b). On Ag(110), the bromine-phenyl bond is cleaved so that split-off bromine atoms and the molecular cores adsorb separately. The observed networks are molecular triradicals linked by adatoms (freely diffusing substrate atoms loosely bound to the crystalline surface) or surface atoms of the respective substrate. The strong phenyl-metal interaction hinders self-assembly into an ordered structure, which explains the occurrence of a glassy network. In contrast, the adsorption of TBB on Ag(111) favors assembly of intact molecules into different polymorphs, leaving the molecule chemically unchanged

(Figure 4.11 c). Although being comprised of the same element, the Ag(110) surface promotes a different kind of adsorption behavior than the Ag(111) surface.
Exemplifying the decisive role of crystallographic surface orientation for surface chemistry is included in publications 2 and 6. Both publications describe how the substrate's ability to induce homolytic scission of a covalent bond in a molecule can lead to the formation of metal-organic complexes. The metal-organic complexes can be converted into covalently bonded structures upon annealing, thereby releasing the coordinating metal atom from in between two radicals (publication 2). The suppression of the bond breaking at low temperatures is discussed in publication 6.

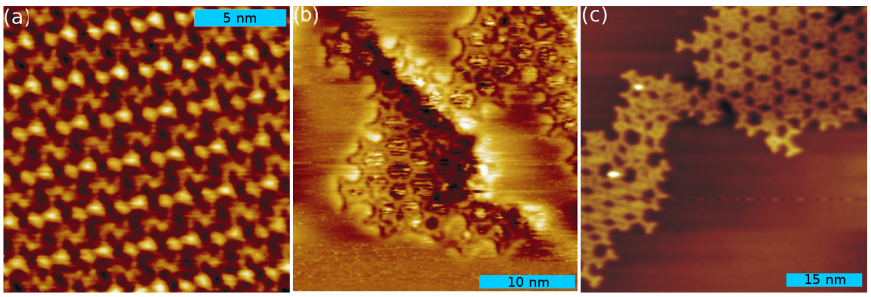

Figure 4.11 – STM topographs of TBB monolayers on (a) graphite, (b) Ag(110), and (c) Ag(111). Sublimation parameters were similar in all three cases. The substrate greately influences the morphology of the monolayer.

Chapter 5

Conclusion

Understanding surface-bound molecular self-assembly is an important requirement for the rational structuring and functionalization of surfaces. Molecular monolayers can be designed to create open-pore networks which allow for selective coadsorption of specific guest molecules, or permit changing the affinity of a surface *via* the adsorption of functionalized molecules. This work's primary focus is to elucidate different parameters which influence self-assembly of molecules. These parameters include amongst others temperature, solvent, concentration, substrate (both material and crystallographic orientation), and molecular interactions. Various examples of molecular self-assembly investigated by STM are presented and explained.

A first short part discusses the concept of self-assembly in the context of molecular adsorption on surfaces, for which the STM has proven to be a suitable instrument for imaging and characterization. A brief introduction on the mechanisms of tunneling through molecular interfaces is given in the following part of this work, enlightening some of the important features of STM and helping to interpret the contrast of STM images. It is shown that molecular orbitals which lie within an energy interval defined by an applied bias between tip and sample contribute to the tunneling current. Two different cases are discussed. One of strong adsorption of the molecule on the surface, resulting in an hybridized density of states of surface bands and molecular orbitals, and one of weak adsorption, in which case isolated and almost unperturbed molecular orbitals can be imaged.

Self-assembled monolayers in their thermodynamic equilibrium state correspond to a minimum in Gibbs free energy. They are thus mainly driven by thermodynamics, although kinetic factors like adsorption and desorption rates are non-negligible. The importance of thermodynamics and kinetics is considered in the third part of this work. Detailed calculations on enthalpy and entropy changes upon self-assembly have to be conducted in order to decipher the thermodynamic driving forces. While enthalpy can partially be accessed by quantum chemical calculations, entropy changes can be estimated using established formulas. From these two quantities, a change in

free energy, and thus the relative stability of different polymorphs, can be calculated when molecules assemble on a surface. The kinetics of adsorption, i.e., adsorption and desorption rates and lateral surface diffusion of the adsorbate, are equally important in defining the outcome of the self-assembly process. Higher fluxes seem to stabilize densely-packed polymorphs, while lower fluxes nucleate less dense structures like open-pore networks. Accordingly, a delicate balance between thermodynamics and kinetics is driving the self-assembly, and only by understanding these factors a systematic approach to the engineering of molecular interfaces becomes feasible.
Parameters which influence self-assembly are divided into two categories: internal and external. The internal parameters are encoded into the molecular building blocks and include inter- and intramolecular interactions and the geometry of the molecules. The environment in which the molecules assemble is defined by the external parameters and include solvent or vacuum, surface, temperature, and concentration in solution. All of these parameters can be used to steer the final structure of the self-assembled monolayer. For example, by an adequate choice of molecular building blocks, a molecular network with cavities can be created. Tuning intermolecular interactions can modify the morphology of the monolayer, and also temperature can be used to reversibly switch between different polymorphs. Reversibility of the bonds linking the fundamental building blocks of the self-assembled structure is of paramount importance for the generation of ordered monolayers. This is accented by the observation of strongly bonded metal-organic systems. Once the intermolecular bond is formed, mediated by a metal atom or cluster, the non-reversibility of the covalent bond leads to the formation of disordered layers. Non-reversibility is a major problem in the synthesis of surface-bound two dimensional polymers, since it inhibits the formation of polymers with long range order.
The controlled engineering of surfaces at the very small scale using molecules is still not accomplished, since a detailed understanding of the involved processes in molecular self-assembly is missing. The present work is an attempt to unravel some of its influencing parameters and factors. However, further work has to be done before conclusive knowledge permits the specific design and fabrication of molecular monolayers. One of the next prominent steps in supramolecular chemistry is to find conditions under which ordered covalent networks can be formed at surfaces. This would pave the way towards the synthesis of two-dimensional polymers, reticulating the unique properties of common organic polymers into a new class of materials.

List of Figures

Bibliography

[1] M. D. Ward. Directing the Assembly of Molecular Crystals. *MRS Bulletin*, 30:705–712, 2005.

[2] J. C. Love, L. A. Estroff, J. K. Kriebel, R. G. Nuzzo, and G. M. Whitesides. Self-Assembled Monolayers of Thiolates on Metals as a Form of Nanotechnology. *Chemical Reviews*, 105:1103–1170, 2005.

[3] C. M. Dobson. Protein Folding and Misfolding. *Nature*, 426:884–890, 2003.

[4] M. Vendruscolo, J. Zurdo, C. E. MacPhee, and C. M. Dobson. Protein Folding and Misfolding: A Paradigm of Self-Assembly and Regulation in Complex Biological Systems. *Philosophical Transactions: Mathematical, Physical and Engineering Sciences*, 361:1205–1222, 2003.

[5] H. Tien. The Lipid Bilayer Concept and its Experimental Realization: from Soap Bubbles, Kitchen Sink, to Bilayer Lipid Membranes. *Journal of Membrane Science*, 189:83–117, 2001.

[6] Z. Mao, H. Xu, and D. Wang. Molecular Mimetic Self-Assembly of Colloidal Particles. *Advanced Functional Materials*, 20:1053–1074, 2010.

[7] J. Lobo-Checa, M. Matena, K. Müller, J. H. Dil, F. Meier, L. H. Gade, T. A. Jung, and M. Stöhr. Band Formation from Coupled Quantum Dots Formed by a Nanoporous Network on a Copper Surface. *Science*, 325:300–303, 2009.

[8] J. Yoon, W. Lee, and E. L. Thomas. Self-Assembly of Block Copolymers for Photonic-Bandgap Materials. *MRS Bulletin*, 30:721–726, 2005.

[9] H. Cölfen and S.-H. Yu. Biomimetic Mineralization/Synthesis of Mesoscale Order in Hybrid Inorganic-Organic Materials via Nanoparticle Self-Assembly. *MRS Bulletin*, 30:727–735, 2005.

[10] J. V. Barth. Molecular Architectonic on Metal Surfaces. *Annual Review of Physical Chemistry*, 58:375–407, 2007.

[11] S. Stepanow, N. Lin, and J. V. Barth. Modular Assembly of Low-Dimensional Coordination Architectures on Metal Surfaces. *Journal of Physics: Condensed Matter*, 20:184002, 2008.

[12] A. Kühnle. Self-assembly of Organic Molecules at Metal Surfaces. *Current Opinion in Colloid & Interface Science*, 14:157–168, 2009.

[13] T. Kudernac, S. Lei, J. A. A. W. Elemans, and S. de Feyter. Two-dimensional Supramolecular Self-Assembly: Nanoporous Networks on Surfaces. *Chemical Society Reviews*, 38:402–421, 2009.

[14] L. Bartels. Tailoring Molecular Layers at Metal Surfaces. *Nature Chemistry*, 2:87–95, 2010.

[15] H. I. Li, K. Pussi, K. J. Hanna, L. L. Wang, D. D. Johnson, H. P. Cheng, H. Shin, S. Curtarolo, W. Moritz, J. A. Smerdon, R. McGrath, and R. D. Diehl. Surface Geometry of C_{60} on Ag(111). *Physical Review Letters*, 103:056101, 2009.

[16] W. Moritz, J. Landskron, and M. Deschauer. Perspectives for surface structure analysis with low energy electron diffraction. *Surface Science*, 603(10-12):1306–1314, June 2009.

[17] S. A. Burke, J. M. Topple, and P. Grutter. Molecular Dewetting on Insulators. *Journal of Physics: Condensed Matter*, 21:423101, 2009.

[18] J. Barth. Transport of Adsorbates at Metal Surfaces: from Thermal Migration to hot Precursors. *Surface Science Reports*, 40:75–149, 2000.

[19] M. Lackinger, T. Müller, T. G. Gopakumar, F. Müller, M. Hietschold, and G. W. Flynn. Tunneling Voltage Polarity Dependent Submolecular Contrast of Naphthalocyanine on Graphite. A STM Study of Close-Packed Monolayers under Ultrahigh-Vacuum Conditions. 108(7):2279–2284, 2004.

[20] J. Repp, G. Meyer, S. M. Stojković, A. Gourdon, and C. Joachim. Molecules on Insulating Films: Scanning-Tunneling Microscopy Imaging of Individual Molecular Orbitals. *Physical Review Letters*, 94:026803, 2005.

[21] W. H. Soe, C. Manzano, A. de Sarkar, N. Chandrasekhar, and C. Joachim. Direct Observation of Molecular Orbitals of Pentacene Physisorbed on Au(111) by Scanning Tunneling Microscope. *Physical Review Letters*, 102, 2009.

[22] F. Rosei, M. Schunack, Y. Naitoh, P. Jiang, A. Gourdon, E. Laegsgaard, I. Stensgaard, C. Joachim, and F. Besenbacher. Properties of Large Organic Molecules on Metal Surfaces. *Progress in Surface Science*, 71:95–146, 2003.

[23] J. A. A. W. Elemans and S. de Feyter. Structure and function revealed with submolecular resolution at the liquid-solid interface. *Soft Matter*, 5(4):721–735, 2009.

[24] J. D. Halley and D. A. Winkler. Consistent Concepts of Self-Organization and Self-Assembly. *Complexity*, 14:10–17, 2008.

[25] S. de Feyter and F. C. de Schryver. Self-Assembly at the Liquid/Solid Interface: STM Reveals. *The Journal of Physical Chemistry B*, 109:4290–4302, 2005.

[26] J. V. Barth, G. Costantini, and K. Kern. Engineering Atomic and Molecular Nanostructures at Surfaces. *Nature*, 437:671–679, 2005.

[27] J. A. A. W. Elemans, S. Lei, and S. de Feyter. Molecular and Supramolecular Networks on Surfaces: From Two-Dimensional Crystal Engineering to Reactivity. *Angewandte Chemie International Edition*, 48:7298–7332, 2009.

[28] Y. Yang and C. Wang. Solvent Effects on Two-Dimensional Molecular Self-Assemblies Investigated by Using Scanning Tunneling Microscopy. *Current Opinion in Colloid & Interface Science*, 14:135–147, 2009.

[29] M. Lackinger and W. M. Heckl. Carboxylic Acids: Versatile Building Blocks and Mediators for Two-Dimensional Supramolecular Self-Assembly. *Langmuir*, 25:11307–11321, 2009.

[30] S. Datta. Electrical Resistance: an Atomistic View. *Nanotechnology*, 15:S433–S451, 2004.

[31] J. Bardeen. Tunnelling from a Many-Particle Point of View. *Physical Review Letters*, 6:57–59, 1961.

[32] J. Tersoff and D. R. Hamann. Theory of the Scanning Tunneling Microscope. *Physical Review B*, 31:805–813, 1985.

[33] J. Lagoute, K. Kanisawa, and S. Fölsch. Manipulation and Adsorption-Site Mapping of Single Pentacene Molecules on Cu(111). *Physical Review B*, 70:245415, 2004.

[34] B. C. Stipe, M. A. Rezaei, and W. Ho. A Variable-Temperature Scanning Tunneling Microscope Capable of Single-Molecule Vibrational Spectroscopy. *Review of Scientific Instruments*, 70:137–143, 1999.

[35] J. Frohn, J. F. Wolf, K. Besocke, and M. Teske. Coarse Tip Distance Adjustment and Positioner for a Scanning Tunneling Microscope. *Review of Scientific Instruments*, 60:1200–1201, 1989.

[36] M. Roos, A. Breitruck, H. E. Hoster, and R. J. Behm. Entropic Stabilization of Large Adsorbates on Weakly Binding Substrates - a Thermal Desorption and Scanning Tunneling Microscopy Study. *Physical Chemistry Chemical Physics*, 12:818–822, 2010.

[37] M. Mammen, E. I. Shakhnovich, J. M. Deutch, and G. M. Whitesides. Estimating the Entropic Cost of Self-Assembly of Multiparticle Hydrogen-Bonded Aggregates Based on the Cyanuric Acid.Melamine Lattice. *The Journal of Organic Chemistry*, 63:3821–3830, 1998.

[38] E. Krissinel and K. Henrick. Inference of Macromolecular Assemblies from Crystalline State. *Journal of Molecular Biology*, 372:774–797, 2007.

[39] L. Kampschulte, T. L. Werblowsky, R. S. K. Kishore, M. Schmittel, W. M. Heckl, and M. Lackinger. Thermodynamical Equilibrium of Binary Supramolecular Networks at the Liquid-Solid Interface. *Journal of the American Chemical Society*, 130:8502–8507, 2008.

[40] S. Lei, K. Tahara, F. C. de Schryver, M. van der Auweraer, Y. Tobe, and S. de Feyter. One Building Block, Two Different Supramolecular Surface-Confined Patterns: Concentration in Control at the Solid-Liquid Interface. *Angewandte Chemie International Edition*, 47:2964–2968, 2008.

[41] C.-A. Palma, J. Björk, M. Bonini, M. S. Dyer, A. Llanes-Pallas, D. Bonifazi, M. Persson, and P. Samorì. Tailoring Bicomponent Supramolecular Nanoporous Networks: Phase Segregation, Polymorphism, and Glasses at the Solid-Liquid Interface. *Journal of the American Chemical Society*, 131:13062–13071, 2009.

[42] J. F. Baret. Kinetics of Adsorption from a Solution. Role of the Diffusion and of the Adsorption-Desorption Antagonism. *The Journal of Physical Chemistry*, 72:2755–2758, 1968.

[43] A. Mikhailov and G. Ertl. Pattern Formation by Adsorbates with Attractive Lateral Interactions. *Chemical Physics Letters*, 238:104–109, 1995.

[44] Z. Adamczyk. Nonequilibrium Surface Tension for Mixed Adsorption Kinetics. *Journal of Colloid and Interface Science*, 120:477–485, 1987.

[45] K. Kim, K. E. Plass, and A. J. Matzger. Kinetic and Thermodynamic Forms of a Two-Dimensional Crystal. *Langmuir*, 19:7149–7152, 2003.

[46] M. Lackinger, S. Griessl, T. Markert, F. Jamitzky, and W. M. Heckl. Self-Assembly of Benzene-Dicarboxylic Acid Isomers at the Liquid Solid Interface: Steric Aspects of Hydrogen Bonding. *The Journal of Physical Chemistry B*, 108:13652–13655, 2004.

[47] K. Tahara, S. Furukawa, H. Uji-i, T. Uchino, T. Ichikawa, J. Zhang, W. Mamdouh, M. Sonoda, F. C. De Schryver, S. De Feyter, and Y. Tobe. Two-Dimensional Porous Molecular Networks of Dehydrobenzo[12]annulene Derivatives via Alkyl Chain Interdigitation. *Journal of the American Chemical Society*, 128:16613–16625, 2006.

[48] A. Langner, S. L. Tait, N. Lin, C. Rajadurai, M. Ruben, and K. Kern. Self-Recognition and Self-Selection in Multicomponent Supramolecular Coordination Networks on Surfaces. *Proceedings of the National Academy of Sciences*, 104:17927–17930, 2007.

[49] K. Tahara, S. Okuhata, J. Adisoejoso, S. Lei, T. Fujita, S. de Feyter, and Y. Tobe. 2D Networks of Rhombic-Shaped Fused Dehydrobenzo[12]annulenes: Structural Variations under Concentration Control. *Journal of the American Chemical Society*, 131:17583–17590, 2009.

[50] S. Furukawa, H. Uji-i, K. Tahara, T. Ichikawa, M. Sonoda, F. C. de Schryver, Y. Tobe, and S. de Feyter. Molecular Geometry Directed Kagomé and Honeycomb Networks: Toward Two-Dimensional Crystal Engineering. *Journal of the American Chemical Society*, 128:3502–3503, 2006.

[51] Q. Chen, H. Yan, C. Yan, G. Pan, L. Wan, G. Wen, and D. Zhang. STM Investigation of the Dependence of Alkane and Alkane ($C_{18}H_{38}$, $C_{19}H_{40}$) Derivatives Self-Assembly on Molecular Chemical Structure on HOPG Surface. *Surface Science*, 602:1256–1266, 2008.

[52] J. V. Barth, J. Weckesser, C. Cai, P. Günter, L. Bürgi, O. Jeandupeux, and K. Kern. Building Supramolecular Nanostructures at Surfaces by Hydrogen Bonding. *Angewandte Chemie International Edition*, 39:1230–1234, 2000.

[53] S. B. Lei, C. Wang, S. X. Yin, H. N. Wang, F. Xi, H. W. Liu, B. Xu, L. J. Wan, and C. L. Bai. Surface Stabilized Porphyrin and Phthalocyanine Two-Dimensional Network Connected by Hydrogen Bonds. *The Journal of Physical Chemistry B*, 105:10838–10841, 2001.

[54] J. A. Theobald, N. S. Oxtoby, M. A. Phillips, N. R. Champness, and P. H. Beton. Controlling Molecular Deposition and Layer Structure with Supramolecular Surface Assemblies. *Nature*, 424:1029–1031, 2003.

[55] K. Kannappan, T. L. Werblowsky, K. T. Rim, B. J. Berne, and G. W. Flynn. An Experimental and Theoretical Study of the Formation of Nanostructures of Self-Assembled Cyanuric Acid Through Hydrogen Bond Networks on Graphite. *The Journal of Physical Chemistry B*, 111:6634–6642, 2007.

[56] S. Weigelt, C. Busse, M. Nielsen, K. V. Gothelf, E. Lægsgaard, F. Besenbacher, and T. R. Linderoth. Influence of Molecular Geometry on the Adsorption Orientation for Oligophenylene-Ethynylenes on Au(111). *The Journal of Physical Chemistry B*, 111:11342–11345, 2007.

[57] H. Wang, T. E. Kaiser, S. Uemura, and F. Würthner. Perylene Bisimide J-Aggregates with Absorption Maxima in the NIR. *Chemical Communications*, pages 1181–1183, 2008.

[58] A. Cristadoro, M. Ai, H. J. Räder, J. P. Rabe, and K. Müllen. Electrical Field-Induced Alignment of Nonpolar Hexabenzocoronene Molecules into Columnar Structures on Highly Oriented Pyrolitic Graphite Investigated by STM and SFM. *The Journal of Physical Chemistry C*, 112:5563–5566, 2008.

[59] S.-L. Lee, N.-T. Lin, W.-C. Liao, C.-H. Chen, H.-C. Yang, and T.-Y. Luh. Oligomeric Tectonics: Supramolecular Assembly of Double-Stranded Oligobisnorbornene through pi-pi Stacking. *Chemistry - A European Journal*, 15:11594–11600, 2009.

[60] J. Reichert, A. Schiffrin, W. Auwaerter, A. Weber-Bargioni, M. Marschall, M. Dell'Angela, D. Cvetko, G. Bavdek, A. Cossaro, A. Morgante, and J. V. Barth. l-Tyrosine on Ag(111): Universality of the Amino Acid 2D Zwitterionic Bonding Scheme? *ACS Nano*, 4:1218–1226, 2010.

[61] D. Kühne, F. Klappenberger, R. Decker, U. Schlickum, H. Brune, S. Klyatskaya, M. Ruben, and J. V. Barth. High-Quality 2D Metal-Organic Coordination Network Providing Giant Cavities within Mesoscale Domains. *Journal of the American Chemical Society*, 131(11):3881–3883, 2009.

[62] M. Böhringer, W.-D. Schneider, and R. Berndt. Real Space Observation of a Chiral Phase Transition in a Two-Dimensional Organic Layer. *Angewandte Chemie International Edition*, 39:792–795, 2000.

[63] G. Pawin, K. L. Wong, K.-Y. Kwon, and L. Bartels. A Homomolecular Porous Network at a Cu(111) Surface. *Science*, 313:961–962, 2006.

[64] Y. Wang, X. Ge, C. Manzano, J. Kröger, R. Berndt, W. A. Hofer, H. Tang, and J. Cerda. Supramolecular Patterns Controlled by Electron Interference and Direct Intermolecular Interactions. *Journal of the American Chemical Society*, 131:10400–10402, 2009.

[65] H. Zhou, H. Dang, J.-H. H. Yi, A. Nanci, A. Rochefort, and J. D. Wuest. Frustrated 2D Molecular Crystallization. *Journal of the American Chemical Society*, 129:13774–13775, 2007.

[66] R. Otero, M. Lukas, R. E. A. Kelly, W. Xu, E. Laegsgaard, I. Stensgaard, L. N. Kantorovich, and F. Besenbacher. Elementary Structural Motifs in a Random Network of Cytosine Adsorbed on a Gold(111) Surface. *Science*, 319:312–315, 2008.

[67] M. O. Blunt, J. C. Russell, M. Giménez-López, J. P. Garrahan, X. Lin, M. Schröder, N. R. Champness, and P. H. Beton. Random Tiling and Topological Defects in a Two-Dimensional Molecular Network. *Science*, 322:1077–1081, 2008.

[68] J. P. Garrahan, A. Stannard, M. O. Blunt, and P. H. Beton. Molecular Random Tilings as Glasses. *Proceedings of the National Academy of Sciences*, 106:15209–15213, 2009.

[69] M. Marschall, J. Reichert, A. Weber-Bargioni, K. Seufert, W. Auwaerter, S. Klyatskaya, G. Zoppellaro, M. Ruben, and J. V. Barth. Random Two-Dimensional String Networks Based on Divergent Coordination Assembly. *Nature Chemistry*, 2:131–137, 2010.

[70] R. Valiokas, M. Östblom, S. Svedhem, S. C. T. Svensson, and B. Liedberg. Temperature-Driven Phase Transitions in Oligo(ethylene glycol)-Terminated Self-Assembled Monolayers. *The Journal of Physical Chemistry B*, 104:7565–7569, 2000.

[71] R. Yamada, H. Wano, and K. Uosaki. Effect of Temperature on Structure of the Self-Assembled Monolayer of Decanethiol on Au(111) Surface. *Langmuir*, 16:5523–5525, 2000.

[72] C.-J. Li, Q.-D. Zeng, Y.-H. Liu, L.-J. Wan, C. Wang, C.-R. Wang, and C.-L. Bai. Evidence of a Thermal Annealing Effect on Organic Molecular Assembly. *ChemPhysChem*, 4:857–859, 2003.

[73] W. Azzam, A. Bashir, A. Terfort, T. Strunskus, and Ch Wöll. Combined STM and FTIR Characterization of Terphenylalkanethiol Monolayers on Au(111): Effect of Alkyl Chain Length and Deposition Temperature. *Langmuir*, 22:3647–3655, 2006.

[74] L. Askadskaya and J. P. Rabe. Anisotropic Molecular Dynamics in the Vicinity of Order-Disorder Transitions in Organic Monolayers. *Physical Review Letters*, 69:1395–1398, 1992.

[75] D. Bléger, D. Kreher, F. Mathevet, A.-J. Attias, G. Schull, A. Huard, L. Douillard, C. Fiorini-Debuischert, and F. Charra. Surface Noncovalent Bonding for Rational Design of Hierarchical Molecular Self-Assemblies. *Angewandte Chemie International Edition*, 46:7404–7407, 2007.

[76] W. A. English and K. W. Hipps. Stability of a Surface Adlayer at Elevated Temperature: Coronene and Heptanoic Acid on Au(111). *The Journal of Physical Chemistry C*, 112:2026–2031, 2008.

[77] X.-H. Kong, K. Deng, Y.-L. Yang, Q.-D. Zeng, and C. Wang. Effect of Thermal Annealing on Hydrogen Bond Configurations of Host Lattice Revealed in VOPc/TCDB Host-Guest Architectures. *The Journal of Physical Chemistry C*, 111:9235–9239, 2007.

[78] C. Marie, F. Silly, L. Tortech, K. Müllen, and D. Fichou. Tuning the Packing Density of 2D Supramolecular Self-Assemblies at the Solid-Liquid Interface Using Variable Temperature. *ACS Nano*, 4:1288–1292, 2010.

[79] M. Ruben, D. Payer, A. Landa, A. Comisso, C. Gattinoni, N. Lin, J.-P. P. Collin, J.-P. P. Sauvage, A. De Vita, and K. Kern. 2D Supramolecular Assemblies of Benzene-1,3,5-Triyl-Tribenzoic Acid: Temperature-Induced Phase Transformations and Hierarchical Organization with Macrocyclic Molecules. *Journal of the American Chemical Society*, 128:15644–15651, 2006.

[80] T. Classen, M. Lingenfelder, Y. Wang, R. Chopra, C. Virojanadara, U. Starke, G. Costantini, G. Fratesi, S. Fabris, S. de Gironcoli, S. Baroni, S. Haq, R. Raval, and K. Kern. Hydrogen and Coordination Bonding Supramolecular Structures of Trimesic Acid on Cu(110). *The Journal of Physical Chemistry A*, 111:12589–12603, 2007.

[81] M. Matena, T. Riehm, M. Stöhr, T. A. Jung, and L. H. Gade. Transforming Surface Coordination Polymers into Covalent Surface Polymers: Linked Polycondensed Aromatics Through Oligomerization of N-Heterocyclic Carbene Intermediates. *Angewandte Chemie International Edition*, 47:2414–2417, 2008.

[82] M. Matena, A. Llanes-Pallas, M. Enache, T. Jung, J. Wouters, B. Champagne, M. Stöhr, and D. Bonifazi. Conformation-Controlled Networking of H-Bonded Assemblies on Surfaces. *Chemical Communications*, pages 3525–3527, 2009.

[83] L. Merz, M. Parschau, L. Zoppi, K. K. Baldridge, J. S. Siegel, and K.-H. Ernst. Reversible Phase Transitions in a Buckybowl Monolayer. *Angewandte Chemie International Edition*, 48:1966–1969, 2009.

[84] M. Lackinger, S. Griessl, W. M. Heckl, M. Hietschold, and G. W. Flynn. Self-Assembly of Trimesic Acid at the Liquid-Solid Interface - A Study of Solvent-Induced Polymorphism. *Langmuir*, 21:4984–4988, 2005.

[85] Lorenz Kampschulte, Markus Lackinger, Anne-Kathrin Maier, Ravuri S. Kishore, Stefan Griessl, Michael Schmittel, and Wolfgang M. Heckl. Solvent Induced Polymorphism in Supramolecular 1,3,5-Benzenetribenzoic Acid Monolayers. *The Journal of Physical Chemistry B*, 110:10829–10836, 2006.

[86] W. Mamdouh, H. Uji-i, J. S. Ladislaw, A. E. Dulcey, V. Percec, F. C. de Schryver, and S. de Feyter. Solvent Controlled Self-Assembly at the Liquid-Solid Interface Revealed by STM. *Journal of the American Chemical Society*, 128:317–325, 2006.

[87] X. Shao, X. Luo, X. Hu, and K. Wu. Solvent Effect on Self-Assembled Structures of 3,8-Bis-hexadecyloxy-benzo[c]cinnoline on Highly Oriented Pyrolytic Graphite. *The Journal of Physical Chemistry B*, 110:1288–1293, 2006.

[88] Y. Li, Z. Ma, G. Qi, Y. Yang, Q. Zeng, X. Fan, C. Wang, and W. Huang. Solvent Effects on Supramolecular Networks Formed by Racemic Star-Shaped Oligofluorene Studied by Scanning Tunneling Microscopy. *The Journal of Physical Chemistry C*, 112:8649–8653, 2008.

[89] H. Walch, A.-K. Maier, W. M. Heckl, and M. Lackinger. Isotopological Supramolecular Networks from Melamine and Fatty Acids. *The Journal of Physical Chemistry C*, 113:1014–1019, 2009.

[90] T. Takami, U. Mazur, and K. W. Hipps. Solvent-Induced Variations in Surface Structure of a 2,9,16,23-Tetra-tert-butyl-phthalocyanine on Graphite. *The Journal of Physical Chemistry C*, 113:17479–17483, 2009.

[91] C. Meier, M. Roos, D. Künzel, A. Breitruck, H. E. Hoster, K. Landfester, A. Gross, R. J. Behm, and U. Ziener. Concentration and Coverage Dependent Adlayer Structures:

From Two-Dimensional Networks to Rotation in a Bearing. *The Journal of Physical Chemistry C*, 114:1268–1277, 2010.

[92] Y. Ye, W. Sun, Y. Wang, X. Shao, X. Xu, F. Cheng, J. Li, and K. Wu. A Unified Model: Self-Assembly of Trimesic Acid on Gold. *The Journal of Physical Chemistry C*, 111:10138–10141, 2007.

[93] H. E. Hoster, M. Roos, A. Breitruck, C. Meier, K. Tonigold, T. Waldmann, U. Ziener, K. Landfester, and R. J. Behm. Structure Formation in Bis(terpyridine) Derivative Adlayers: Molecule-Substrate versus Molecule-Molecule Interactions. *Langmuir*, 23:11570–11579, 2007.

List of Publications

The following pages contain a chronological list of publications which were published as part of the doctoral program.

1. **Aromatic Interaction *vs.* Hydrogen Bonding in Self-Assembly at the Liquid-Solid Interface**
Rico Gutzler, Sophie Lappe, Kingsuk Mahata, Michael Schmittel, Wolfgang M. Heckl, and Markus Lackinger
Chemical Communications **6**, 680 (2009)

2. **Surface Mediated Synthesis of 2D Covalent Organic Frameworks: 1,3,5-Tris(4-Bromophenyl)Benzene on Graphite(001), Cu(111), and Ag(110)**
Rico Gutzler, Hermann Walch, Georg Eder, Stephan Kloft, Wolfgang M. Heckl, and Markus Lackinger
Chemical Communications **29**, 4456 (2009)

3. **Combination of a Knudsen Effusion Cell With a Quartz Crystal Microbalance: *In Situ* Measurement of Molecular Evaporation Rates With a Fully Functional Deposition Source**
Rico Gutzler, Wolfgang M. Heckl, and Markus Lackinger
Review of Scientific Instruments **81**, 015108 (2010)

4. **Influence of Solvophobic Effects on Self-Assembly of Trimesic Acid at the Liquid-Solid Interface**
Nguyen T. N. Ha, Thiruvancheril G. Gopakumar, Rico Gutzler, Markus Lackinger, Hao Tang, and Michael Hietschold
Journal of Physical Chemistry C **114**, 3531 (2010)

5. **Reversible Phase Transitions in Self-Assembled Monolayers at the Liquid-Solid Interface: Temperature-Controlled Opening and Closing of Nanopores**
Rico Gutzler, Thomas Sirtl, Jürgen F. Dienstmaier, Kingsuk Mahata, Wolfgang M. Heckl, Michael Schmittel, and Markus Lackinger
Journal of the American Chemical Society **132**, 5084 (2010)

6. **Material and Orientation Dependent Activity for Heterogeneously Catalyzed Carbon-Bromine Bond Homolysis**
Hermann Walch, Rico Gutzler, Thomas Sirtl, Georg Eder, and Markus Lackinger
Journal of Physical Chemistry C **114**, 12604 (2010)

Aromatic interaction *vs.* hydrogen bonding in self-assembly at the liquid–solid interface†

Rico Gutzler,*[a] Sophie Lappe,[a] Kingsuk Mahata,[b] Michael Schmittel,[b] Wolfgang M. Heckl[ac] and Markus Lackinger*[a]

Received (in Cambridge, UK) 25th July 2008, Accepted 24th November 2008
First published as an Advance Article on the web 12th December 2008
DOI: 10.1039/b812890a

Interfacial self-assembly of specific monolayer structures from solution on a graphite surface can be steered by tuning the interplay between solute–solute and solute–solvent interactions.

Molecular self-assembly on surfaces is a promising route for the efficient production of functional nanostructures. Non-covalent interactions such as dispersion forces,[1] hydrogen bonds,[2] coordination bonds,[3] and aromatic interactions[4] routinely drive self-assembly processes on surfaces. Therefore, carboxylic groups are prominent synthons, facilitating, for instance, self-assembly of trimesic acid and 1,3,5-benzenetribenzoic acid.[5–9] Nevertheless, weaker aromatic interactions can also play a major role for supramolecular arrangements.[10,11] Since in many important systems, most prominent in DNA,[12] the interplay between H-bonds and aromatic interactions determines the structure, it is of particular interest to study competition and cooperation.

Solvent effects on molecular self-assembly have been investigated in various studies.[6,8,13,14] Here, we demonstrate that not only solute–solvent interactions can catalyze the formation of a particular structure but also solute–solute interactions. In the system presented, defining supramolecular units of the monolayer structure are already preformed in solution and not exclusively in the adsorbed state.

Self-assembly of two compounds at the liquid–solid interface is investigated by STM with the tip immersed into solution. Molecule **I** (4-{2-{3,5-bis[2-(4-carboxyphenyl)-1-ethynyl] phenyl}-1-ethynyl}benzoic acid) is synthesized by the reported method,[15] synthesis of **II** (4-{2-{3,5-bis[2-(4-carboxyphenyl)-1-ethynyl]-2,4,6-trimethyl-phenyl}-1-ethynyl} benzoic acid) is described in the ESI.† Interfacial monolayers of compound **I** (*cf.* Fig. 1(a), R = H) are studied on graphite in four different solvents: nonanoic acid (NA), 1,2,4-trichlorobenzene (TCB), 3-phenylbutyric acid (PBA) and 1,3-dibromobenzene (DBB) (*cf.* Fig. 1(b)–(e)). In NA molecule **I** forms a row structure as

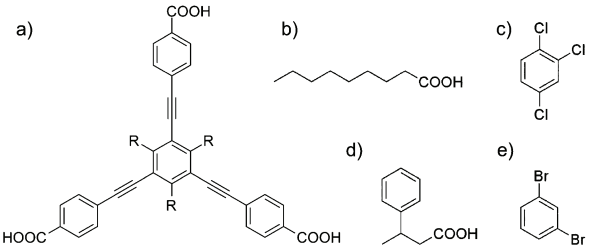

Fig. 1 Chemical structures of molecules and solvents: (a) **I**: R = H, **II**: R = CH_3, (b) nonanoic acid (NA), (c) 1,2,4-trichlorobenzene (TCB), (d) 3-phenylbutyric acid (PBA), (e) 1,3-dibromobenzene (DBB).

depicted in Fig. 2(a), with two molecules per unit cell. Due to different adsorption sites on the graphite substrate every other row appears higher (brighter). Lattice parameters account to 3.8 × 0.8 nm^2 and 84° with a row spacing of 1.9 nm. The observed rows can be explained by π–π stacking of molecules along an axis parallel to the surface. The same stacking was found in the bulk crystal structure of *sym*-triphenethynyl benzene (= **I** without carboxylic groups).[16]

Both cases exemplify the importance of π–π interactions for the crystallization of molecules with a fairly extended aromatic system, both in the bulk structure and on a surface. Yet, the situation at the liquid–solid interface is completely altered just by utilizing a different solvent.

Both with TCB and DBB as solvents, an entirely different monolayer structure with a hexagonal unit cell and a lattice parameter of 4.1 nm emerges (*cf.* Fig. 2(b) and Fig. S2, ESI†). This structure is consistent with planar adsorption of **I** and intermolecular bonding through twofold H-bonds between carboxylic groups. Similar chickenwire networks have previously been observed for smaller tricarboxylic acids.[5–9] Based on this analogy, a nanoporous network with a periodic arrangement of cavities was expected. Instead, a hexagonal arrangement of ~3.3 nm wide protrusions is observed. This contrast, however, is in accordance with formation of the chickenwire structure and co-adsorption of 19 solvent molecules within the cavities where the pristine substrate is exposed to solution (see Fig. 2(b) and Fig. S10, ESI† for a model).

In the following, we offer evidence that the formation of dissimilar monolayer structures of **I** in different solvents originates from pre-aggregation in hydrogen bonding solvents. Thus, in NA compound **I** forms molecular stacks already in solution which adsorb and seed the row structure, whereas in TCB and DBB monomers of **I** adsorb in a planar manner on

[a] *Department of Earth and Environmental Sciences and Center for NanoScience (CeNS), Ludwig-Maximilians-University, Theresienstraße 41, 80333 Munich, Germany.*
E-mail: rico.gutzler@lrz.uni-muenchen.de.
E-mail: markus@lackinger.org; Fax: +49 (0)89 2180 4334; Tel: +49 (0)89 2180 4317
[b] *Center of Micro and Nanochemistry and Engineering, Organische Chemie I, University Siegen, Adolf-Reichwein-Straße 2, 57068 Siegen, Germany*
[c] *Deutsches Museum, Museumsinsel 1, 80538 Munich, Germany*
† Electronic supplementary information (ESI) available: Synthesis of **II**, detailed description of experimental procedures and calculations, additional STM data and UV/Vis spectra. See DOI: 10.1039/b812890a

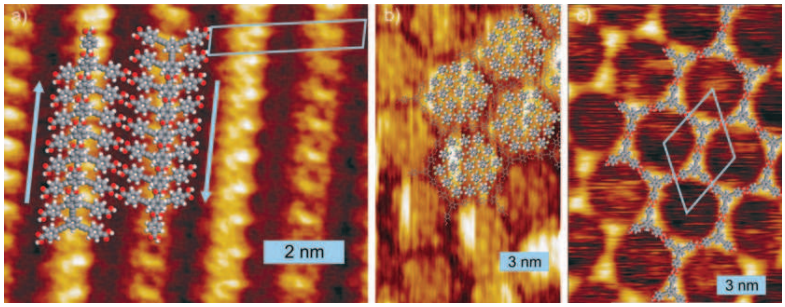

Fig. 2 Simulated structures superimposed on STM topographs and scaled accordingly (unit cells are indicated by blue lines): (a) row structure of nearly upright standing molecules **I** in NA (1.2 V; 20 pA); molecules in adjacent rows are tilted by 36° with respect to the substrate in opposite directions as indicated by the arrows. (b) Hexagonal structure of **I** in TCB (1.1 V; 70 pA). Within one cavity, 19 TCB molecules are co-adsorbed in a hexagonal arrangement. (c) Hexagonal structure of **II** in NA (1.1 V; 66 pA). The basic unit is an H-bonded dimer as seen in the indicated unit cell (same as in (b)). The color scale corresponds to a height difference of 0.60, 0.75, and 1.00 (arb. units) for (a), (b), and (c), respectively.

the surface resulting in a hexagonal structure stabilized by intermolecular H-bonding.

Non-protic aromatic solvents without functional groups for H-bonds, such as TCB and DBB, are well suited to inhibit any π–π stacking of solute molecules in solution, thus facilitating planar adsorption. In contrast, a protic, non-aromatic solvent such as NA does not efficiently solvate individual molecules of **I**.

Its main interaction with finite stacks of **I**, which are stabilized by intermolecular π–π interactions, is *via* H-bonding to the peripheral carboxylic groups. Thus, although not incorporated into the structure, the solvent plays a crucial role in defining the outcome of the self-assembly process.

PBA as solvent, exhibiting both aromatic character and H-bond capabilities, represents an interesting case to evaluate the relative importance of both contributors. Self-assembly of **I** in PBA resulted exclusively in the row structure, demonstrating the energetic supremacy of the solvent's H-bonding to stabilize the stack structure.

The rather high defect density in the row structure, mainly a single or a few missing molecules, provides further indirect evidence for our model. Formation of the ordered row structure should be driven by preformation of molecular stacks in solution and adsorption of the stacks is controlled by inter-row cross-linking *via* H-bonds. However, the stacks are immobile along the rows, which inhibits dense packing and causes the observed gaps. Since most aggregates in solution are too large to fit into the resulting gaps within the rows and the monomer concentration in protic solvents is negligible, these defects cannot be healed out efficiently.

Interestingly, the hexagonal structure can also be enforced in NA by means of a minor chemical modification of **I** not even affecting the functional groups. Compound **II** differs from **I** by methylation of the inner benzene ring (R = CH_3). Experimentally observed STM images are presented in Fig. 2(c). The monolayer is non-densely packed and represents a periodic arrangement of ~3.3 nm wide cavities with hexagonal symmetry and a lattice parameter of 4.1 nm. In contrast to Fig. 2(b) the cavities appear lower (darker) than the supramolecular network because solute or solvent molecules which are likely to adsorb within the cavities are too mobile to be imaged with the STM. Since **I** and **II** are identical with regard to outer dimensions and functionalization, the lattice parameters of their hexagonal structures are equal within experimental accuracy. Owing to the bulkiness of the methyl group the aromatic interaction is considerably weakened and inhibits stacking of **II**, even in solvents without aromatic interaction as NA. The methyl groups are also expected to weaken the interaction of the molecule with the graphite substrate, however, intermolecular H-bonds stabilize the interfacial monolayer. Likewise, STM experiments with compound **II** in TCB reveal solvent co-adsorption within the cavities of a hexagonal network, though molecular resolution could not be obtained (*cf.* Fig. S5, ESI†).

Further experimental evidence for aggregation of compound **I** in NA has been acquired by concentration dependent UV/Vis spectroscopy. The spectra exhibit two distinct peaks whose relative intensities are concentration dependent (*cf.* Fig. 3(a)). The peak at $\lambda_{monomer}$ = 323 nm is assigned to monomers, whereas the hypsochromically shifted absorbance peak at $\lambda_{aggregate}$ = 304 nm results from aggregates. Hypsochromic shifts have previously been observed for π-stacked aromatic molecules[17,18] and are theoretically grounded on a molecular exciton model.[19] Lowering the concentration of **I** in NA results in a diminishing intensity of the aggregate related peak relative to the monomeric peak in agreement with the law of mass action. In contrast, for compound **II** in NA the relative intensities of the two absorption peaks at λ_1 = 320 nm and λ_2 = 334 nm (Fig. 3(b)) are independent of concentration. This finding is in accordance with the absence of aggregation of **II** in NA.

STM experiments with diluted solutions down to 1% with respect to saturation always resulted in the row structure,

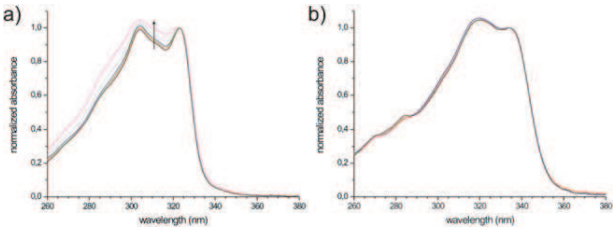

Fig. 3 UV/Vis spectra of **I** in NA (a) and **II** in NA (b) normalized to the intensity of the absorption maxima at larger wavelength. Concentration was varied from 75% saturation to 5% saturation in (a) and 100% to 25% saturation in (b). The arrow on the left hand side indicates the direction of increasing concentration.

thereby demonstrating the predominance of aggregates. No interfacial solute monolayers could be observed any more for even lower concentrations.

Experiments with mixtures of protic and non-protic solvents further support the hypothesis of solvent dependent aggregation. When 1 mL of a clear 1 molar solution of **I** in a 1 : 1 mixture of benzene and CF_3COOH was treated with extra acid (addition of 0.2 mL of neat CF_3COOH) the solution became turbid as observed by the naked eye, a clear indication for aggregate formation.

It is imperative to note that an aged solution of **II** in NA (stored for nine months at room temperature) yielded the row structure. However, sonication of the solution at 50 °C for 15 min restored the commonly observed hexagonal structure. Thus, although sterically disfavored by the methyl group, the row structure is caused by the presence of weakly bound stacks of compound **II** in solution that formed in a slow process over months. Yet, compared to compound **I**, steric hindrance considerably weakens the π–π stacking; consequently aggregates can easily be broken up by sonication, which was not possible for compound **I**.

In order to support the experimental findings, force-field and DFT calculations were performed. Experimental unit cell parameters were used as a constraint for force-field calculations; results are overlaid in Fig. 2(a)–(c). Geometry optimized structures of isolated molecules were obtained by DFT/B3LYP calculations. The distance between two carbon atoms in adjacent carboxylic groups of **I** was found to be ~1.7 nm, a value quite close to the inter-row spacing of ~1.9 nm. For the row structure, a herringbone like arrangement is proposed which facilitates H-bonds between neighboring molecules in adjacent rows. These H-bonds also account for the 0.2 nm difference between molecular size and row spacing.[20] According to the proposed model, bright spots at the center of the rows originate from carboxylic groups pointing off the surface. Within the rows, molecules are tilted by ~36° with respect to the substrate such that the upper phenyl ring is close to the C–C triple bond of the intra-row neighbor, similarly observed in the solid state.[16] The measured distance between the phenyl ring and the triple bond of 3.7 Å corresponds to the expected distance for π–π stacks.[21] The basic unit of the hexagonal structure is an H-bonded dimer. Interconnecting those dimers through H-bonds in an energetically favorable 180° geometry yields the chickenwire network. The bond length and size of the calculated dimer of both molecules **I** and **II** exactly match the STM data.

Aromatic bonding is to a large part responsible for the planar adsorption of aromatic molecules on graphite.[5] Here we demonstrate that π–π stacking can also dominate interactions between adsorbates. Since the structure defining molecular aggregates are already preformed in solution, the outcome of the self-assembly process can be steered by choice of solvent. Moreover, minor chemical substitutions can considerably alter the competition between H-bonding and π–π interaction. Methylation of an otherwise planar aromatic molecule imposes sterical hindrance for aromatic stacking, leading to a predominance of H-bonding and formation of the associated interfacial monolayer. For self-assembly processes from solution, a detailed understanding of solute–solvent interaction is desirable in order to eventually control the result.

Financial support by the Deutsche Forschungsgemeinschaft (SFB 486), the Bayerische Forschungsstiftung and the Nanosystems Initiative Munich (NIM) is gratefully acknowledged.

Notes and references

1 M. Pokrifchak, T. Turner, I. Pilgrim, M. R. Johnston and K. W. Hipps, *J. Phys. Chem. C*, 2007, **111**, 7735–7740.
2 J. A. Theobald, N. S. Oxtoby, M. A. Phillips, N. R. Champness and P. H. Beton, *Nature*, 2003, **424**, 1029–1031.
3 S. Stepanow, M. Lingenfelder, A. Dmitriev, H. Spillmann, E. Delvigne, N. Lin, X. Deng, C. Cai, J. V. Barth and K. Kern, *Nat. Mater.*, 2004, **3**, 229–233.
4 S. Weigelt, C. Busse, M. Nielsen, K. V. Gothelf, E. Laegsgaard, F. Besenbacher and T. R. Linderoth, *J. Phys. Chem. B*, 2007, **111**, 11342–11345.
5 M. Li, K. Deng, Y.-L. Yang, Q.-D. Zeng, M. He and C. Wang, *Phys. Rev. B*, 2007, **76**, 155438.
6 M. Lackinger, S. Griessl, W. M. Heckl, M. Hietschold and G. W. Flynn, *Langmuir*, 2005, **21**, 4984–4988.
7 M. Ruben, D. Payer, A. Landa, A. Comisso, C. Gattinoni, N. Lin, J.-P. Collin, J.-P. Sauvage, A. De Vita and K. Kern, *J. Am. Chem. Soc.*, 2006, **128**, 15644–15651.
8 L. Kampschulte, M. Lackinger, A. K. Maier, R. S. K. Kishore, S. Griessl, M. Schmittel and W. M. Heckl, *J. Phys. Chem. B*, 2006, **110**, 10829–10836.
9 Y. Ye, W. Sun, Y. Wang, X. Shao, X. Xu, F. Cheng, J. L. Li and K. Wu, *J. Phys. Chem. C*, 2007, **111**, 10138–10141.
10 P. Yan, A. Chowdhury, M. W. Holman and D. M. Adams, *J. Phys. Chem. B*, 2005, **109**, 724–730.
11 B. H. Hong, J. Y. Lee, C. Lee, J. C. Kim, S. C. Bae and K. S. Kim, *J. Am. Chem. Soc.*, 2001, **123**, 10748–10749.
12 C. F. Matta, N. Castillo and R. J. Boyd, *J. Phys. Chem. B*, 2006, **110**, 563–578.
13 C.-J. Li, Q.-D. Zeng, C. Wang, L.-J. Wan, S.-L. Xu, C.-R. Wang and C.-L. Bai, *J. Phys. Chem. B*, 2003, **107**, 747–750.
14 N. Katsonis, H. Xu, R. M. Haak, T. Kudernac, Ž. Tomović, S. George, M. Van der Auweraer, A. P. H. J. Schenning, E. W. Meijer, B. L. Feringa and S. De Feyter, *Angew. Chem., Int. Ed.*, 2008, **47**, 4997–5001.
15 R. K. Castellano and J. Rebek, Jr., *J. Am. Chem. Soc.*, 1998, **120**, 3657–3663.
16 F. Ponzini, R. Zagha, K. Hardcastle and J. S. Siegel, *Angew. Chem., Int. Ed.*, 2000, **39**, 2323–2325.
17 T. Seki, S. Yagai, T. Karatsu and A. Kitamura, *J. Org. Chem.*, 2008, **73**, 3328–3335.
18 F. Würthner, S. Yao, T. Debaerdemaeker and R. Wortmann, *J. Am. Chem. Soc.*, 2002, **124**, 9431–9447.
19 M. Kasha, H. R. Rawls and M. Ashraf El-Bayoumi, *Pure Appl. Chem.*, 1965, **11**, 371–392.
20 S. Raub and C. M. Marian, *J. Comput. Chem.*, 2007, **28**, 1503–1515.
21 M. O. Sinnokrot, E. F. Valeev and C. D. Sherrill, *J. Am. Chem. Soc.*, 2002, **124**, 10887–10893.

Supporting Information

Aromatic Interaction vs. Hydrogen Bonding in Self-Assembly at the Liquid-Solid Interface

Rico Gutzler*[a], Sophie Lappe[a], Kingsuk Mahata[b], Michael Schmittel[b], Wolfgang M. Heckl[a,c], and Markus Lackinger[a]

Department of Earth and Environmental Sciences and Center for NanoScience (CeNS), Ludwig-Maximilians-University, Theresienstraße 41, 80333 Munich, Germany; Center of Micro and Nanochemistry and Engineering, Organische Chemie I, University Siegen, Adolf-Reichwein-Straße 2, 57068 Siegen, Germany; Deutsches Museum, Museumsinsel 1, 80538 Munich, Germany

Contents

I. Synthesis of Chemical Compound II

4-{2-{3,5-Bis[2-(4-carboxyphenyl)-1-ethynyl]-2,4,6-trimethylphenyl}-1-ethynyl}benzoic acid

Scheme 1

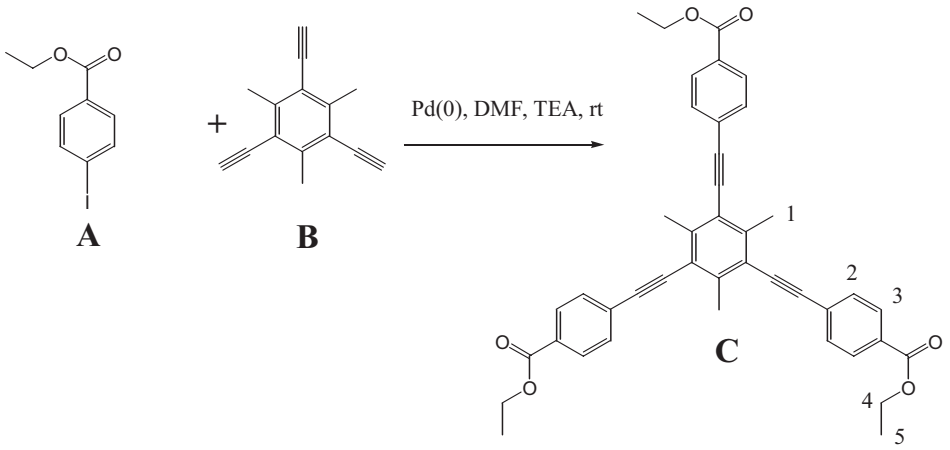

Preparation of C: To a solution of ethyl 4-iodobenzoate (**A**, 1.15 g, 4.16 mmol) in triethylamine (20 mL) and DMF (20 mL), triethynylmesitylene (**B**, 200 mg, 1.04 mmol) and $Pd(PPh_3)_4$ (120 mg, 104 μmol) were added under N_2. The resulting mixture was stirred at room temperature for 20 h. The reaction mixture was dissolved in CH_2Cl_2 (100 mL) and washed with water (2 × 100 mL). The organic phase was dried over $MgSO_4$ and filtered. After removal of the solvents the crude product was purified by column chromatography (silica, ethylacetate:hexane, 1:4) to afford the product as a white solid (490 mg, 77%). MP: 162 °C. IR (KBr): $\tilde{\nu}$ = 3424 (w), 2980 (w), 2203 (w), 17186 (s), 1605 (s), 1506 (w), 1404 (w), 1366 (w), 1271 (s), 1174 (m), 1105 (s), 1019 (m), 854 (m), 767 (s), 694 (w), 526 (w). ^{1}H-NMR (400 MHz, $CDCl_3$): δ = 1.41 (t, *J* = 7.1 Hz, 9H, 5-H), 2.73 (s, 9H, 1-H), 4.40 (q, *J*

= 7.1 Hz, 6H, 4-H), 7.58 (d, *J* = 8.3 Hz, 6H, 2-H), 8.02 (d, *J* = 8.3 Hz, 6H, 3-H). ^{13}C-NMR (100 MHz, $CDCl_3$): δ = 14.4, 20.5, 61.3, 89.6, 97.1, 121.2, 128.0, 129.7, 130.0, 131.4, 143.0, 166.1. Anal calcd for $C_{42}H_{36}O_6$: C, 79.22; H, 5.70; found: C, 79.81; H, 5.69.

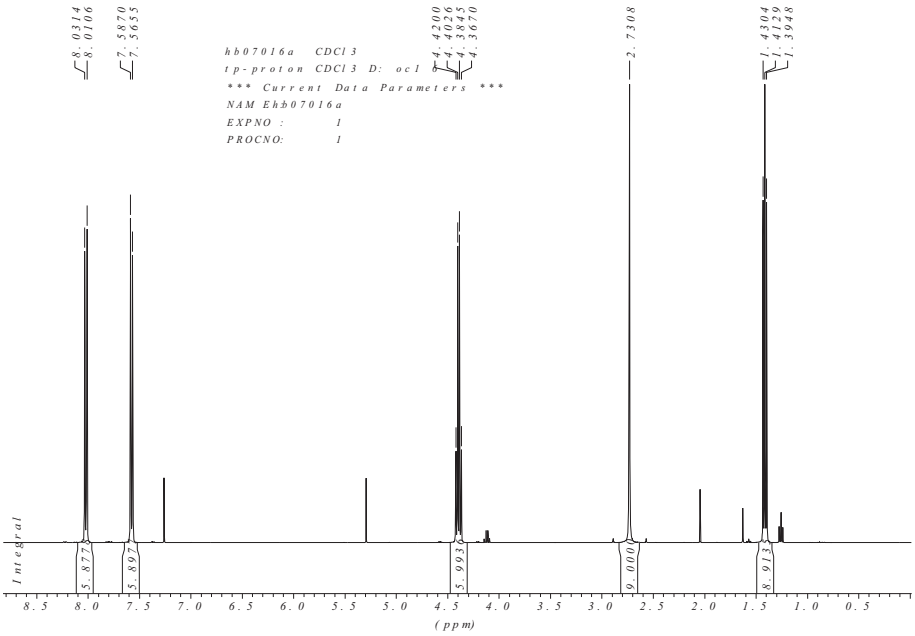

^{1}H-NMR spectrum of compound **C**

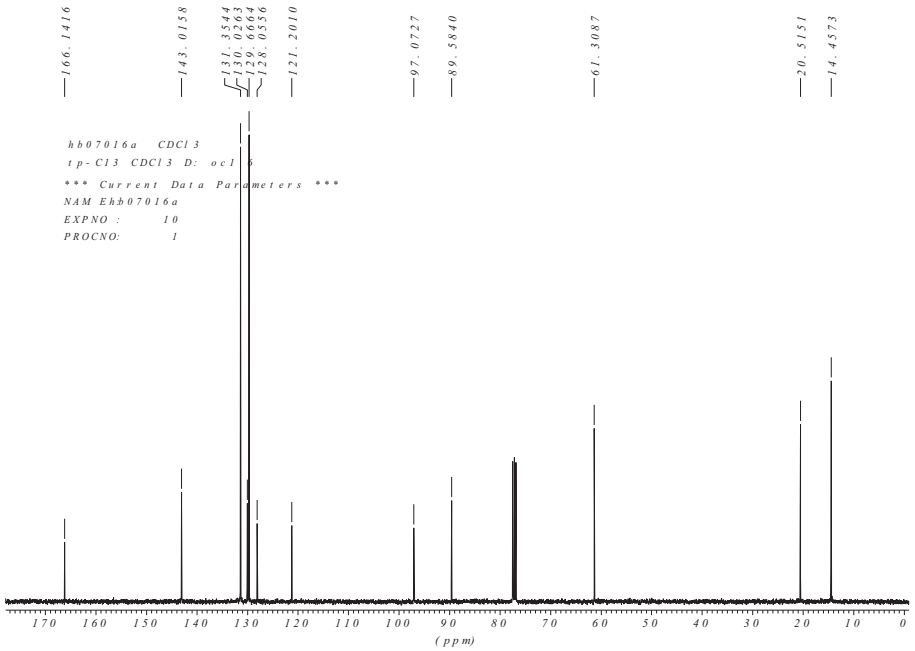

^{13}C-NMR spectrum of compound **C**

Scheme 2

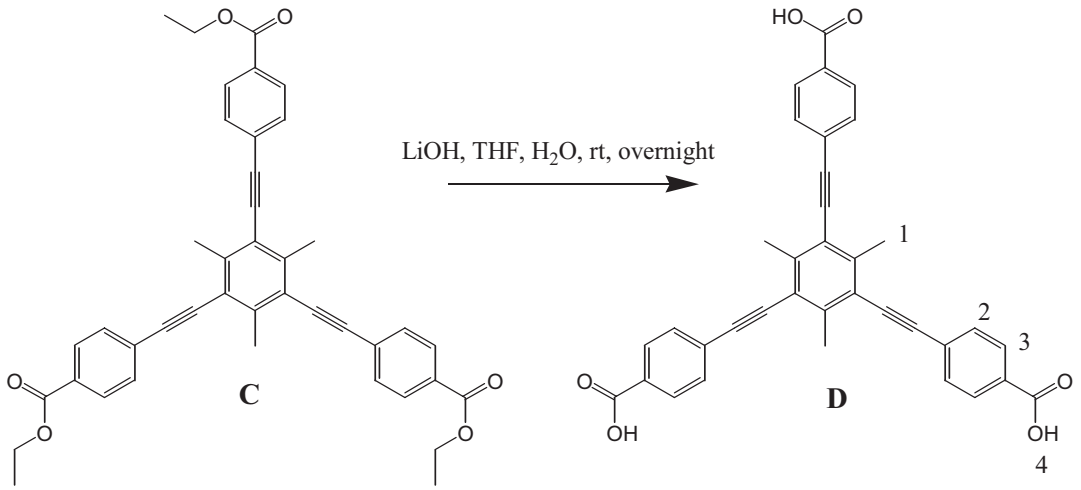

Preparation of D: Ester **C** (430 mg, 675 μmol) was dissolved in a mixture of THF (12 ml) and H_2O (1.8 mL). Then, LiOH monohydrate (568 mg, 13.5 mmol) was added and the mixture was stirred at room temperature while H_2O (6 mL) was added over a period of 1 hour. After the mixture had been stirred at room temperature overnight, 30 mL of THF was added. Then 100 mL of 1 M HCl was added to this solution and the precipitate was filtered by suction. The solid was washed with 100 mL of 1 M HCl and 100mL of acetone to afford product **D** as a white powder (340 mg, 0.615 mmol, 91%). MP: >300 °C. IR (KBr): $\tilde{\nu}$ = 3445 (w), 2850 (w), 2525 (w), 2361 (w), 2200 (w), 1686 (s), 1604 (s), 1558 (m), 1417 (s), 1311 (m), 1275 (s), 1172 (m), 1106 (w), 1015 (w), 854 (m), 768 (s), 690 (w), 551 (w), 510 (w). ^{1}H-NMR (400 MHz, DMSO-d_6): δ = 2.74 (s, 9H, 1-H), 7.72 (d, *J* = 8.3 Hz, 6H, 2-H), 7.99 (d, *J* = 8.3 Hz, 6H, 3-H), 13.22 (br s, 3H, 4-H). ^{13}C-NMR (100 MHz, DMSO-d_6): δ = 20.2, 88.6, 97.1, 120.6, 126.5, 129.6, 130.8, 131.4, 142.6, 166.7. Anal calcd for $C_{36}H_{24}O_6$*1.25H_2O: C, 75.19; H, 4.64; found: C, 75.15; H, 4.40.

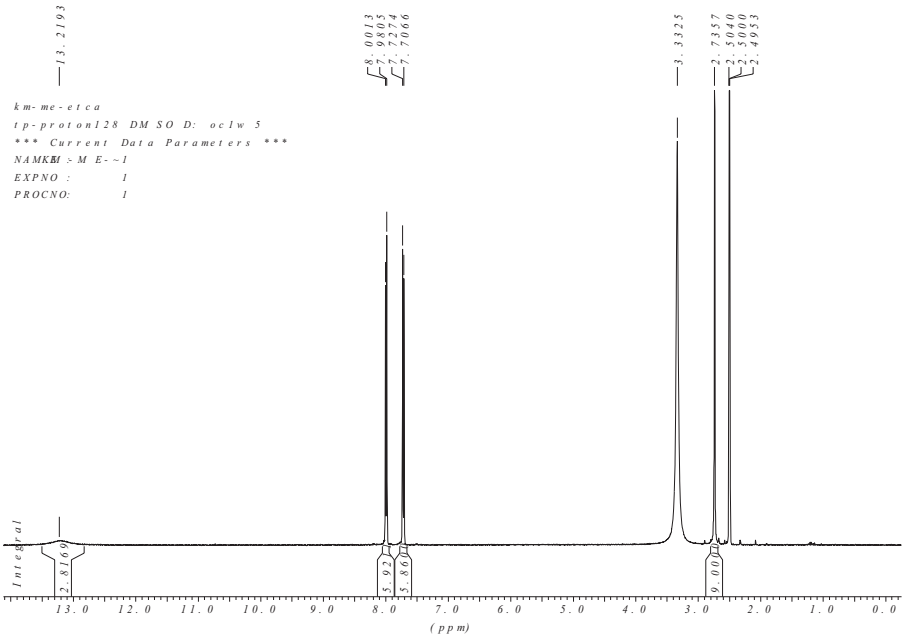

^{1}H-NMR spectrum of compound **D**

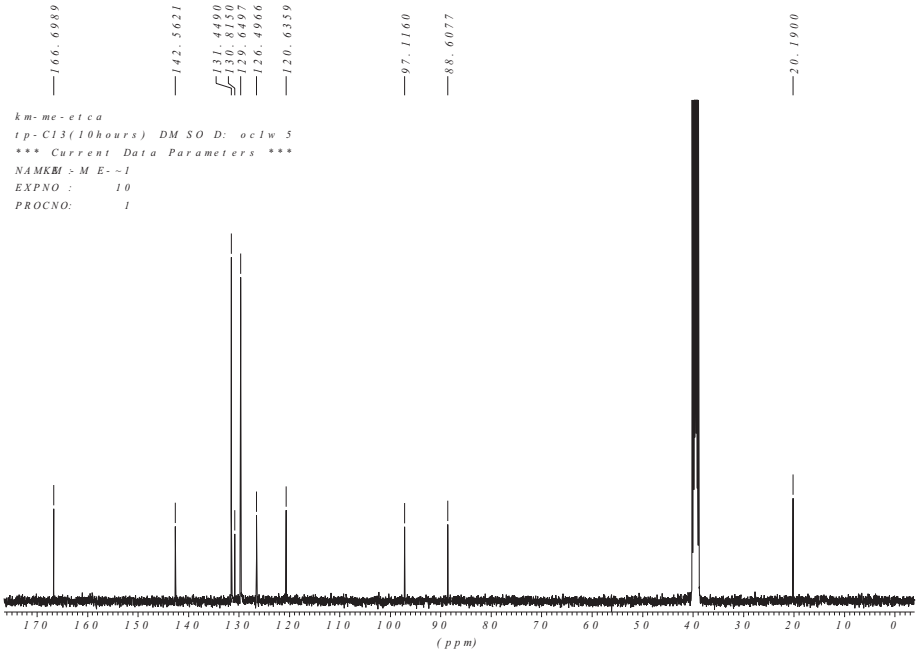

^{13}C-NMR spectrum of compound **D**

II. Experimental details and additional STM topographs

STM experiments were performed with a home-built instrument at ambient temperature (20-25 °C). Solvents were purchased from Aldrich and used as received. STM tips were cut mechanically from platinum/irdium wire (80% Pt / 20% Ir, diameter = 0.25 mm). Molecules **I** and **II** were dissolved in all solvents until saturation. Prior to imaging, a drop (~2.5 μL) of saturated solution was applied to a freshly cleaved (0001) surface of HOPG (Highly Oriented Pyrolytic Graphite). STM experiments were carried out at the liquid-solid interface with the tip immersed into solution in constant-current mode. Atomically resolved graphite images were used for lateral calibration.

UV/vis absorption spectra were recorded with the USB4000 spectrometer from Ocean Optics and a deuterium tungsten lamp as excitation source. Due to high absorbance of the solute molecules a quartz glass cuvette with an optical path length of 1 mm was used. Absorption spectra of pure nonanoic acid were used as a reference.

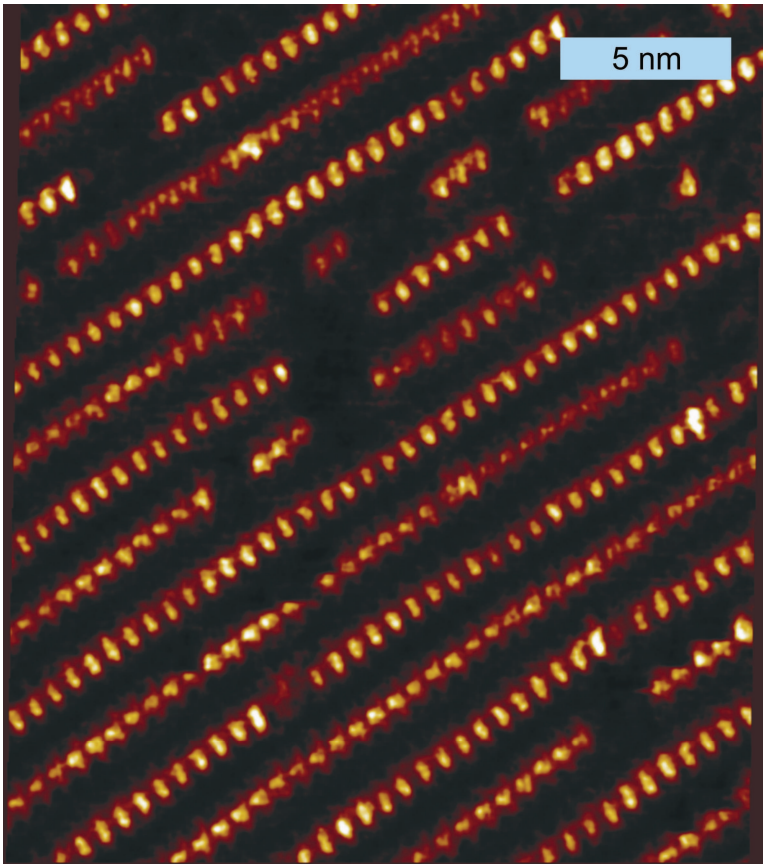

Figure S1. STM topograph of self-assembled monolayers of molecule **I** dissolved in NA (1.2 V; 20 pA). Interrow spacing is 1.9 nm. A high number of defects can be observed and is typical for this self-assembled monolayer.

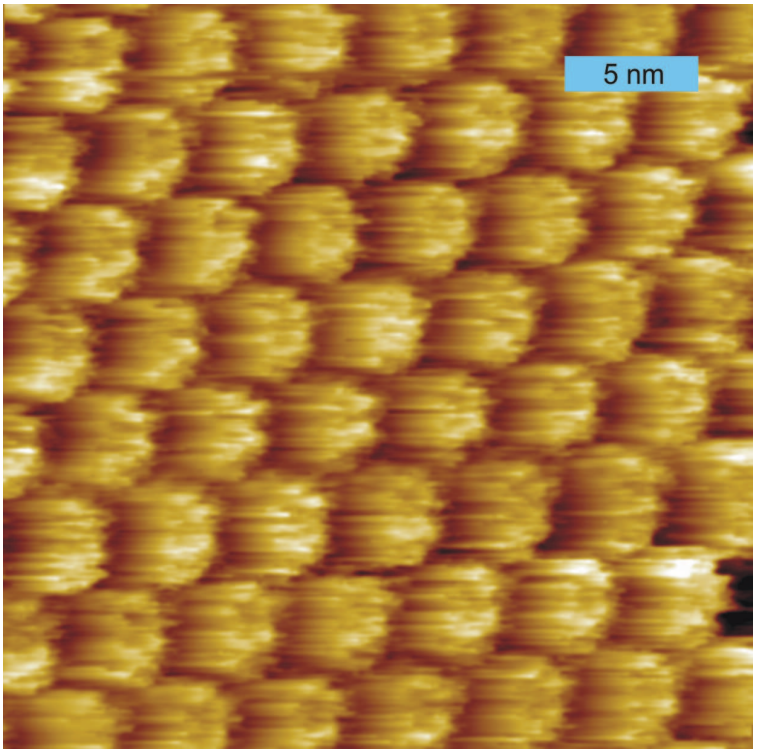

Figure S2. STM topograph of self-assembled monolayers of molecule **I** dissolved in DBB (1.2 V; 100 pA). The lattice parameter of this hexagonal structure accounts to 4.1 nm and is equal to the value of the hexagonal structure of compound **I** in TCB. This class of aromatic nonprotic solvents interacts with the solute through aromatic interactions and is able to break up preformed solute aggregations in solution. Consequently, monomeric adsorption results and the H-bonded chickenwire structure can form.

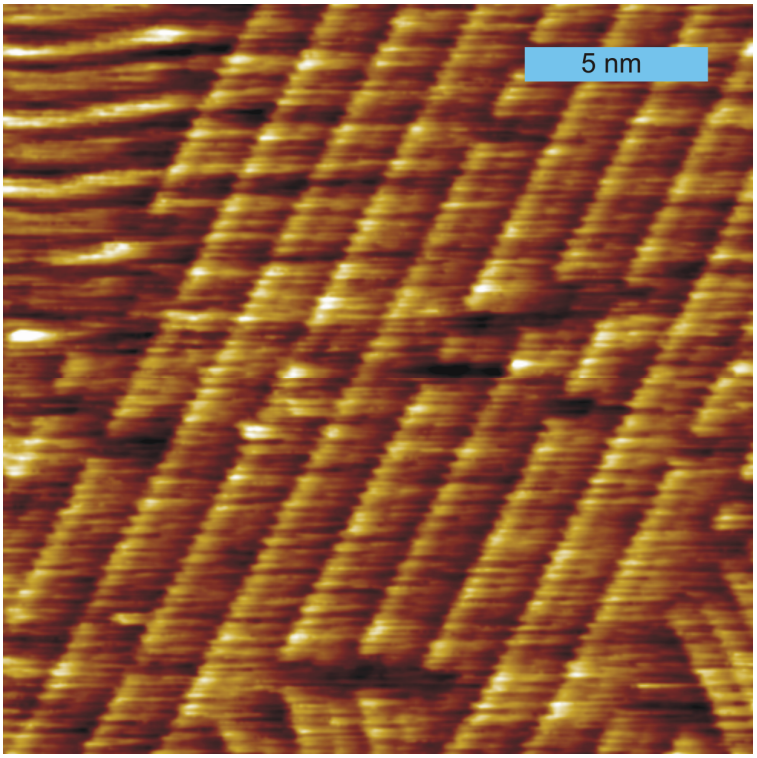

Figure S3. STM topograph of self-assembled monolayers of molecule **I** dissolved in PBA (1.3 V; 23 pA). The same row structure with a row spacing of 1.9 nm is observed in NA. Although the phenyl ring of the solvent might interact with the aromatic system of the solute, the interaction is too weak to cause monomeric dissolution and consequently precipitation of the H-bonded chickenwire structure.

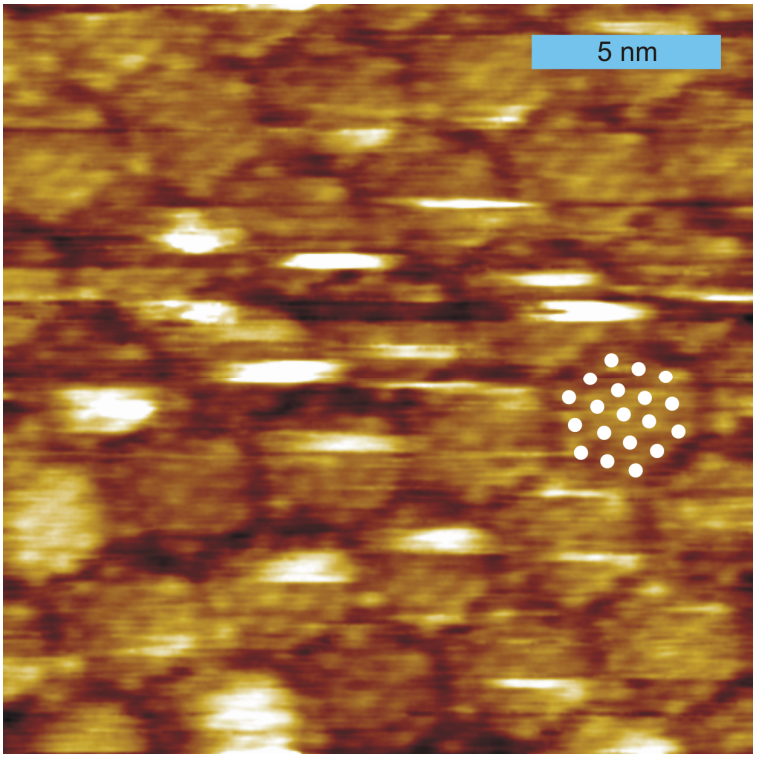

Figure S4. High resolution STM image of self-assembled monolayers of molecule **I** in TCB. Within each cavity 19 bright spots can be identified as indicated by the white dots. The close packed arrangement of the dots exhibits hexagonal symmetry and the size of one dot corresponds to the size of a TCB molecule. This contrast can be explained by planar co-adsorption of 19 solvent molecules within the cavity, thus each bright dot corresponds to one TCB molecule.

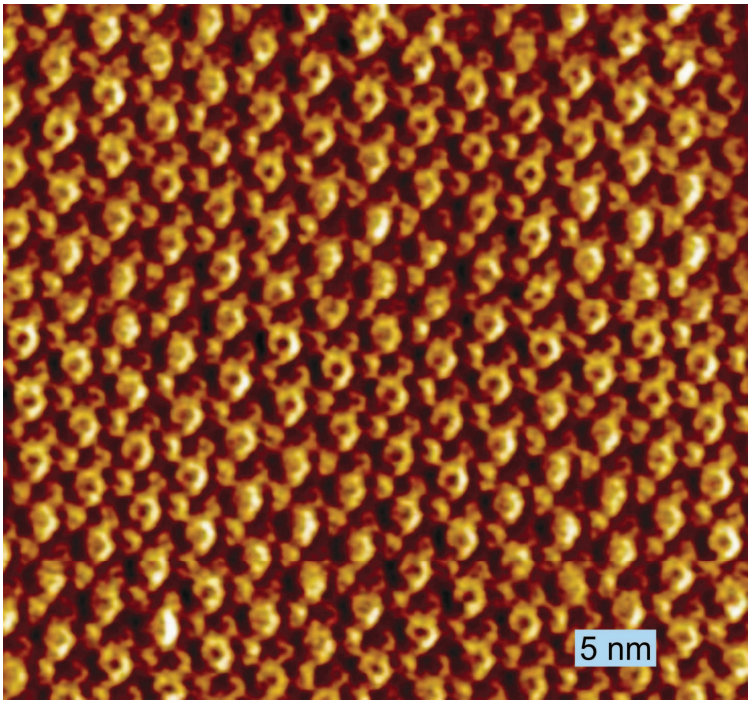

Figure S5. STM topograph of self-assembled monolayer of molecule **II** in TCB (1.1 V; 70 pA). As in Fig. S4, the cavities of the hexagonal arrangement appear brighter than the surrounding molecules **II** themselves. This can be explained by co-adsorption of solvent molecules within the cavities of the open pore network. Molecular resolution of co-adsorbed solvent molecules could not be achieved.

III. Additional UV/vis absorption spectroscopy data

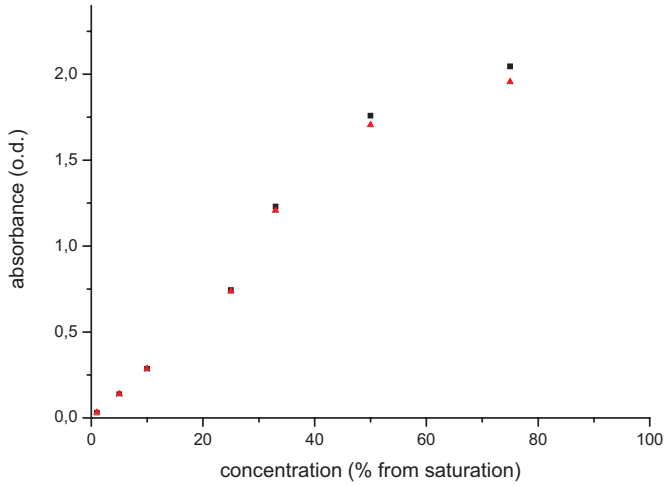

Figure S6. Lambert-Beer plot of molecule **I** dissolved in nonanoic acid. Black squares correspond to the absorbance at λ = 304 nm (aggregate related peak) and red triangles to the absorbance at λ = 323 nm (monomer related peak) (see also Fig. 3 main text). Absorbance is plotted as measured with a 1 mm cuvette.

IV. Theoretical Calculations

The Consistent Valence Force Field (CVFF) was applied to model monolayers of adsorbed molecules on graphite using the Cerius[2] (Version 4.5, MSI) software package. The use of the CVFF was motivated by previous works on structure optimization of organic monolayers on graphite.[1] Here, periodic boundary conditions were employed with the experimental unit cells as a constraint. The graphite substrate was approximated by two layers and atomic positions in the second layer were fixed. Values for the unit cell parameters were deduced from split images, where one part of the image depicts the adsorbate layer and in the other part the graphite substrate was atomically resolved. Molecules were arranged on the surface without further constraints. An energy difference of $< 2\times10^{-5}$ kcal/mol between single steps served as a convergence criteria.

The geometry of isolated molecules **I** and **II** was optimized using density functional theory (DFT) implemented in the Gaussian03 software package.[2] For this purpose, the B3LYP functional was used with the 6-31G(d) basis set. Convergence RMS force criterion was set to 3×10^{-4} Hartree/Bohr.

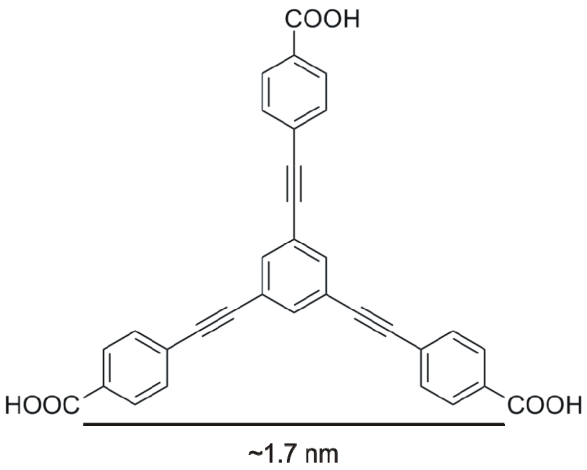

Figure S7. Schematic drawing indicating the distance between two carboxylic groups (carbon atoms were used as reference) of molecule **I** as calculated by DFT calculations.

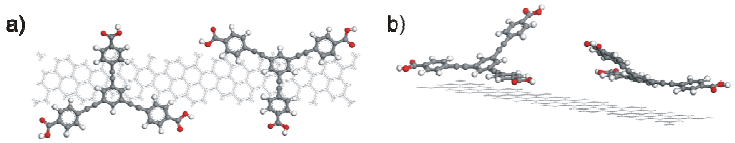

Figure S8. ***(a)*** Top view and ***(b)*** side view of a dimer of molecule **I** in the row structure on HOPG after geometry optimization by force-field calculation. Molecules in adjacent rows are tilted in opposite directions. The tilting angle of the molecule with respect to the substrate is ~36°. The distance of the upper phenyl ring of a molecule to the C-C triple bond of its intra-row neighbor accounts to ~3.7 Å which allows for aromatic interaction. Unit cell: 3.8 nm × 0.8 nm, 84°.

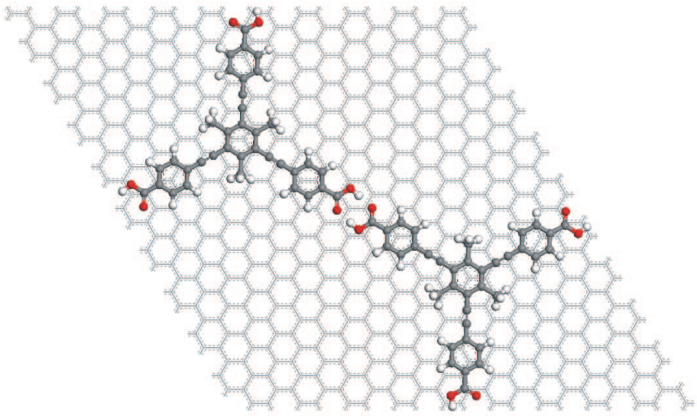

Figure S9. Top view of a dimer of molecule **II** on HOPG after geometry optimization by force-field calculations. Three pairs of hydrogen bonds per molecule stabilize the hexagonal structure. Unit cell: 4.1 nm × 4.1 nm, 60°.

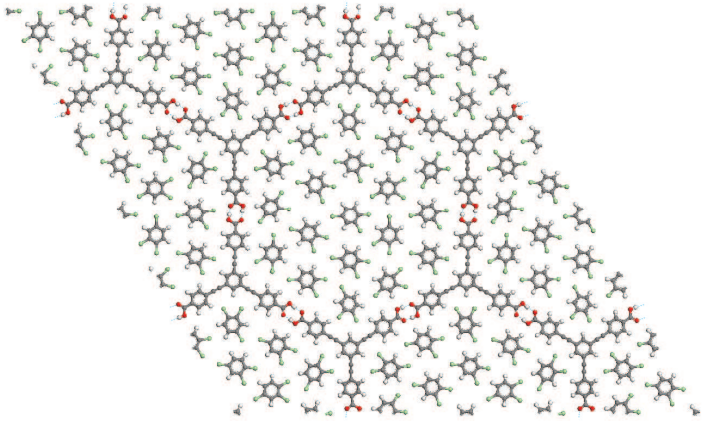

Figure S10. Force field calculation of a model with 19 co-adsorbed TCB solvent molecules within the cavities of an H-bonded network of molecule **I**. Four unit cells (4.1 nm × 4.1 nm, 60°).

V. References

1. Yin, S. X.; Wang, C.; Xu, Q. M.; Lei, S. B.; Wan, L. J.; Bai, C. L. *Chem. Phys. Lett.* **2001,** 348, (3-4), 321-328.
2. Frisch, M. J.; Trucks, G. W.; Schlegel, H. B.; Scuseria, G. E.; Robb, M. A.; Cheeseman, J. R.; Montgomery, J., J. A.; Vreven, T.; Kudin, K. N.; Burant, J. C.; Millam, J. M.; Iyengar, S. S.; Tomasi, J.; Barone, V.; Mennucci, B.; Cossi, M.; Scalmani, G.; Rega, N.; Petersson, G. A.; Nakatsuji, H.; Hada, M.; Ehara, M.; Toyota, K.; Fukuda, R.; Hasegawa, J.; Ishida, M.; Nakajima, T.; Honda, Y.; Kitao, O.; Nakai, H.; Klene, M.; Li, X.; Knox, J. E.; Hratchian, H. P.; Cross, J. B.; Bakken, V.; Adamo, C.; Jaramillo, J.; Gomperts, R.; Stratmann, R. E.; Yazyev, O.; Austin, A. J.; Cammi, R.; Pomelli, C.; Ochterski, J. W.; Ayala, P. Y.; Morokuma, K.; Voth, G. A.; Salvador, P.; Dannenberg, J. J.; Zakrzewski, V. G.; Dapprich, S.; Daniels, A. D.; Strain, M. C.; Farkas, O.; Malick, D. K.; Rabuck, A. D.; Raghavachari, K.; Foresman, J. B.; Ortiz, J. V.; Cui, Q.; Baboul, A. G.; Clifford, S.; Cioslowski, J.; Stefanov, B. B.; Liu, G.; Liashenko, A.; Piskorz, P.; Komaromi, I.; Martin, R. L.; Fox, D. J.; Keith, T.; Al-Laham, M. A.; Peng, C. Y.; Nanayakkara, A.; Challacombe, M.; Gill, P. M. W.; Johnson, B.; Chen, W.; Wong, M. W.; Gonzalez, C.; Pople, J. A., *Gaussian 03, Revision C.02,* **2004**, Gaussian, Inc., Wallingford CT, USA

Surface mediated synthesis of 2D covalent organic frameworks: 1,3,5-tris(4-bromophenyl)benzene on graphite(001), Cu(111), and Ag(110)†

Rico Gutzler,*[a] Hermann Walch,[a] Georg Eder,[a] Stephan Kloft,[a] Wolfgang M. Heckl[ab] and Markus Lackinger*[a]

Received (in Cambridge, UK) 7th April 2009, Accepted 28th May 2009
First published as an Advance Article on the web 12th June 2009
DOI: 10.1039/b906836h

The on surface synthesis of a two-dimensional (2D) covalent organic framework from a halogenated aromatic monomer under ultra-high vacuum conditions is shown to be dependent on the choice of substrate.

The synthesis of 2D covalent organic frameworks (COF) on surfaces has recently gained much attention.[1] Commonly, these novel polymers are built by sublimation of appropriate monomers onto metallic substrates under ultra-high vacuum (UHV) conditions and subsequent annealing.[2–6] Many other studies investigated the formation of covalent structures from smaller building blocks and demonstrated the importance of the substrate both for the confinement of molecular motion in two dimensions and as a catalyst for activation.[7–10]

Here, we report on the reticular synthesis of 2D COFs built up from conjugated subunits (phenyl rings) only. The halogen substituted polyaromatic monomer is thermally sublimed onto various substrates under UHV conditions at room temperature. Without providing additional activation energy, the formation of radicals is observed on Cu(111) and Ag(110). Deposition of the same compound on graphite(001) results in non-covalent self-assembly of well ordered networks stabilized by halogen–hydrogen bonds. These results demonstrate the decisive role of the substrate for homolysis of covalent carbon–halogen bonds at room temperature and subsequent association of radicals.

Our strategy for the synthesis of 2D COFs consists of the deposition of a suitable organic compound and its subsequent substrate mediated homolysis. Intermolecular colligation occurs through radical addition at elevated temperatures. For formation of 2D open-pore networks from a single kind of molecule the building block must at least be a triradical, *i.e.* exhibit three potential binding sites. Comparatively weak carbon–halogen bonds are well suited as predetermined breaking points and from solution chemistry Cu catalysts are known to facilitate homolysis.[11] The molecule of choice is 1,3,5-tris-(4-bromophenyl)benzene (TBB, *cf.* Fig. 1a). TBB is an appropriate candidate because the homolytic bond dissociation energy of its C–Br bonds (3.2 eV) is substantially lower than that of the C–C link between phenyl rings (4.8 eV).[12,13]

Evaporation of a TBB monolayer on graphite(001) results in an ordered structure (*cf.* Fig. 1b and c). Although no submolecular resolution is achieved, the long range order and the mutual arrangement of molecules within the monolayer indicate non-covalent self-assembly of intact TBB molecules.

In agreement with molecular mechanics simulations, molecules arrange in chains of dimers which are stabilized by Br···H–C hydrogen bonds. Similar binding motifs have been reported for comparable systems[14–16] and also stabilize the bulk structure of TBB.[17] The contrast modulation, *i.e.* every other row appears brighter, is caused by different adsorption sites on the graphite lattice. Annealing of the graphite sample to ~320 °C for 10 min results in complete desorption of the TBB monolayer, thereby demonstrating the inferior stability of this non-covalent network.

Open-pore networks can clearly be identified in the STM topographs obtained for submonolayer coverage of TBB on Cu(111) (Fig. 2) and Ag(110) (*cf.* Fig. S1, ESI†). These

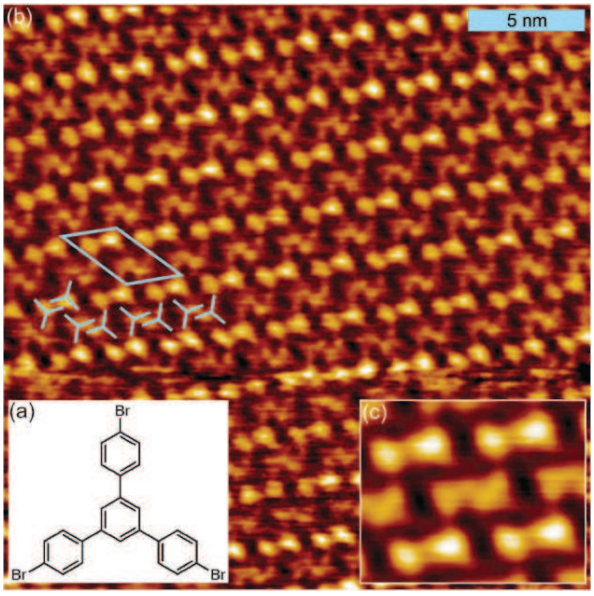

Fig. 1 (a) Structure of 1,3,5-tris(4-bromophenyl)benzene (TBB). (b) STM topograph of a TBB monolayer on graphite (V = 1.9 V, I = 76 pA). Unit cell is indicated by blue lines (a = 3.4 nm, b = 2.5 nm, α = 44°) and accommodates four molecules, symbolized by blue tripods. (c) Mesh-averaged image (4.1 × 5.0 nm^2) of (b).

[a] *Department of Earth and Environmental Sciences and Center for NanoScience (CeNS), Ludwig-Maximilians-University, Theresienstrasse 41, 80333, Munich, Germany. E-mail: rico.gutzler@lrz.uni-muenchen.de, markus@lackinger.org; Tel: +49 89 21804317*
[b] *Deutsches Museum, Museumsinsel 1, 80538, Munich, Germany*
† Electronic supplementary information (ESI) available: Experimental details, calculations, thermogravimetric analysis, additional STM data, and UV/Vis spectra. See DOI: 10.1039/b906836h

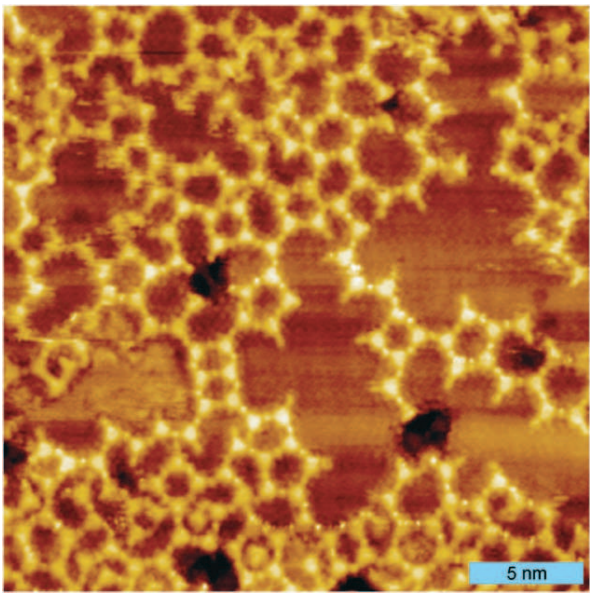

Fig. 2 TBB protopolymer on Cu(111) before annealing ($V = -1.85$ V, $I = 248$ pA). Spherical protrusions between radicals are clearly observable.

networks are composed of polygons, predominantly hexagons and pentagons but also heptagons, octagons and other polygons. The experimentally determined values for the center-to-center distance between adjacent molecules for room temperature deposition are 1.49 nm ± 0.10 nm for Cu(111) and 1.57 nm ± 0.06 nm for Ag(110) and are equal for both substrates within the error margin. These values are somewhat larger than anticipated for a covalent C–C link between adjacent molecules. In the topograph of the TBB network on Cu(111) (Fig. 2), bright protrusions can clearly be discerned between adjacent molecules. These spherical features are attributed to single copper atoms which coordinate two or occasionally three radicals. Similar systems based on halogenated benzene derivatives were reported to assemble in a first step into so-called protopolymers where two radicals are linked *via* a metal atom.[7,18] This preceding formation of a metal coordination complex between on surface-generated radicals and substrate atoms is also likely to be observed here. Coordinating atoms could not be resolved on Ag(110), but the spacing clearly indicates formation of protopolymers as well. In this respect, no difference between the two metal substrates was found, although (110) surfaces exhibit a pronounced anisotropy. In most cases the network structures are attached to step edges, hence it is probable that growth is initiated by attachment of a free radical to a step edge (Fig. S1, ESI†).

In order to verify whether protopolymers can eventually be converted into COFs, annealing experiments have been carried out with the Cu(111) surface. Fig. 3a depicts an STM topograph of a tempered sample. After annealing to 300 °C the distance between two interconnected molecules is reduced to 1.24 nm ± 0.06 nm (Fig. 3a). Accordingly, the linescan in Fig. 3b yields a size of 2.2 nm for each hexagon. The STM contrast of the network after annealing at 300 °C (Fig. 3a) is very different from the network before annealing (Fig. 2). The bright features in between two molecules are absent in the

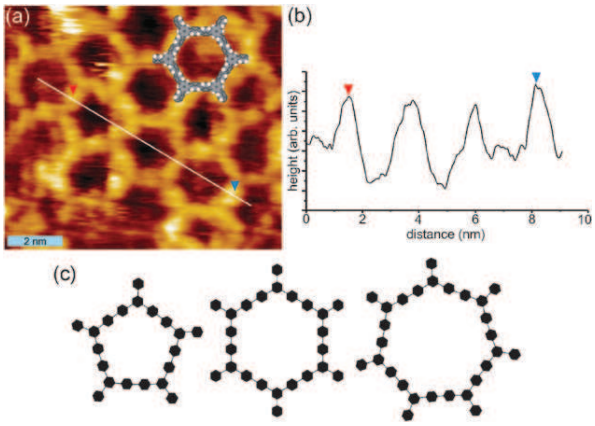

Fig. 3 TBB covalent organic framework on Cu(111) (a) evaporation temperature of 140 °C for 8 minutes ($V = +3.2$ V, $I = 233$ pA) and subsequent annealing to 300 °C. A scaled hexagonal ring is overlaid. (b) Linescan as indicated in (a) across three rings yielding a center-to-center distance of 2.2 nm for a single ring. (c) Principally encountered binding motifs: pentagon, hexagon and heptagon. Bonds between phenyl rings are distorted by $\Delta\alpha$.

post-annealing topograph, indicating a physical change in the monolayer. More importantly, the reduced size (both the lattice constant and the spacing of adjacent molecules) upon annealing indicates the transition from a protopolymer to a 2D COF. Lipton-Duffin *et al.* found for polymerization experiments with *p*-diiodobenzene that the phenyl–phenyl spacing is reduced by 0.12 nm upon transition from a protopolymer to an actual covalent linkage.[7] This value is consistent with our observations. The necessity of an additional annealing step to finally induce covalent linkage was also experienced by other groups for comparable systems.[7,19]

The distance between two monomers in the post-annealing network is also in accordance with both DFT and molecular mechanics simulations of an infinite layer of TBB molecules covalently linked at the 4′-position (1.28 nm, experimental: 1.24 nm ± 0.06 nm). A hypothetical hexagonal network based on intact TBB subunits pointing head-to-head with their bromine atoms would necessarily result in a considerably larger center-to-center distance of ~1.75 nm as estimated by molecular mechanics calculations and can thus be excluded.

The high defect density, that is the frequent occurrence of polygons different from hexagons, can be explained by considering the energy necessary to bend one bond between two phenyl groups: due to the threefold symmetry of TBB, a hexagonal ring comprising six molecules would yield the lowest-energy geometry because all newly formed links exhibited an ideal bonding angle of 180°. All other polygons experience slightly higher stress due to distortion of the bond angle. Assuming regularity and rigid phenyl rings, each bond between two phenyl rings in the polygon is distorted from its optimal equilibrium angle on average by $\Delta\alpha = 60°(6 - N)/(3N)$, where N is the number of molecules in the ring (Fig. 3c). The change $\Delta\alpha$ is small and accounts to 4°, 0°, and −2.9° for pentagon, hexagon, and heptagon, respectively, yielding only a small additional energy contribution. This small deviation from the equilibrium geometry is responsible for the high number of polygons different from hexagons. Since colligation of free

radicals is virtually barrier free and only diffusion limited, kinetic effects can result in suboptimal binding geometries where the binding angle can deviate from 180°. This leads to a reduced order and high defect densities.

Interestingly, the chemical activity of the substrate has a major contribution to cleavage of the C–Br bond. The activation of TBB molecules, that is generation of triple radicals by cleavage of all three covalent C–Br bonds, requires a metallic substrate. In general, the binding energy of halides chemisorbed to metal surfaces is particularly strong and was found to be in the order of 1.5 eV. Thus, a low free energy of the final state certainly promotes homolytic fission of C–Br bonds in TBB. Physisorption of halides on graphite would render homolysis strongly endothermic. In some STM topographs on metal surfaces, circular features appear after deposition of TBB and can be attributed to adsorbed Br atoms.

For the likewise covalently linked structures prepared from Br substituted tetraphenyl porphyrins and dibromoterfluorene on catalytically less active Au(111) surfaces, significantly higher temperature thresholds of 315 °C and 250 °C for thermal activation are reported.[2,20] The first compound is much heavier than TBB and the temperature for bond cleavage is in the regime of the sublimation temperature, thus activation can already occur in the crucible. In contrast, for TBB thermal evaporation of non-activated species is easily possible. The distinct substrate dependence clearly demonstrates that homolysis takes place on the surface and not in the crucible as observed for other systems.[2,6] Furthermore, UV/Vis spectroscopy independently confirms that the TBB molecules are intact prior to sorption on the surface and do not dissociate at the sublimation temperatures of 140–160 °C (*cf.* ESI†).

Thermal stability of the COFs on Cu(111) has been verified by further annealing experiments and subsequent STM characterization. Annealing of the Cu(111) sample at 400 °C caused degradation of the networks and STM images no longer exhibit open-pore structures (see Fig. S2, ESI†, for a degraded network). Thermogravimetric analysis of pure TBB reveals an onset for decomposition at a temperature of around 250 °C (*cf.* ESI†), which is somewhat lower than for the COF. Its higher thermal stability can be attributed to the absence of comparatively weak C–Br bonds in the monolayer, strong intermolecular bonds, and interaction with the substrate.

In this work, we demonstrate the formation of substrate supported 2D COFs by addition of on surface-generated triple radicals. Experiments on different surfaces unveil the important role of the substrate for the main activation step, homolytic fission of C–Br bonds. On metal substrates where the split-off Br-atoms are stabilized by strong chemisorption, homolysis takes place without providing additional activation energy. Chemically inert graphite surfaces cannot promote homolysis, thus cannot initiate formation of covalent bonds. However, due to preceding formation of a protopolymer through metal coordination of radicals, an additional thermal activation is required to transfer the networks eventually into COFs. In this respect it would be highly interesting to find either a system, a method, or conditions where on one hand the substrate is catalytically effective for homolysis but on the other hand formation of protopolymers is suppressed. The immediate formation of covalent bonds would definitely change the association kinetics and will thus possibly also influence the ordering.

Financial support by Deutsche Forschungsgemeinschaft (SFB 486) and Nanosystems Initiative Munich (NIM) is gratefully acknowledged. Georg Eder acknowledges support by the Hanns-Seidel-Stiftung.

Notes and references

1 D. F. Perepichka and F. Rosei, *Science*, 2009, **323**, 216–217.
2 L. Grill, M. Dyer, L. Lafferentz, M. Persson, M. V. Peters and S. Hecht, *Nat. Nanotechnol.*, 2007, **2**, 687–691.
3 M. Treier, N. V. Richardson and R. Fasel, *J. Am. Chem. Soc.*, 2008, **130**, 14054–14055.
4 M. In't Veld, P. Iavicoli, S. Haq, D. B. Amabilino and R. Raval, *Chem. Commun.*, 2008, 1536–1538.
5 S. Weigelt, C. Busse, C. Bombis, M. M. Knudsen, K. V. Gothelf, E. Laegsgaard, F. Besenbacher and T. R. Linderoth, *Angew. Chem., Int. Ed.*, 2008, **47**, 4406–4410.
6 N. A. A. Zwaneveld, R. Pawlak, M. Abel, D. Catalin, D. Gigmes, D. Bertin and L. Porte, *J. Am. Chem. Soc.*, 2008, **130**, 6678–6679.
7 J. A. Lipton-Duffin, O. Ivasenko, D. F. Perepichka and F. Rosei, *Small*, 2009, **5**, 592–597.
8 M. Matena, T. Riehm, M. Stöhr, T. A. Jung and L. H. Gade, *Angew. Chem., Int. Ed.*, 2008, **47**, 2414–2417.
9 S. Weigelt, C. Bombis, C. Busse, M. M. Knudsen, K. V. Gothelf, E. Laegsgaard, F. Besenbacher and T. R. Linderoth, *ACS Nano*, 2008, **2**, 651–660.
10 S. Weigelt, J. Schnadt, A. K. Tuxen, F. Masini, C. Bombis, C. Busse, C. Isvoranu, E. Ataman, E. Laegsgaard, F. Besenbacher and T. R. Linderoth, *J. Am. Chem. Soc.*, 2008, **130**, 5388–5389.
11 S. V. Ley and A. W. Thomas, *Angew. Chem., Int. Ed.*, 2003, **42**, 5400–5449.
12 R. J. Kominar, M. J. Krech and S. J. W. Price, *Can. J. Chem.*, 1978, **56**, 1589–1592.
13 M. Szwarc, *Nature*, 1948, **161**, 890–891.
14 G. R. Desiraju and R. Parthasarathy, *J. Am. Chem. Soc.*, 1989, **111**, 8725–8726.
15 H. F. Lieberman, R. J. Davey and D. M. T. Newsham, *Chem. Mater.*, 2000, **12**, 490–494.
16 O. Navon, J. Bernstein and V. Khodorkovsky, *Angew. Chem., Int. Ed. Engl.*, 1997, **36**, 601–603.
17 L. M. C. Beltran, C. Cui, D. H. Leung, J. Xu and F. J. Hollander, *Acta Crystallogr., Sect. E*, 2002, **58**, O782–O783.
18 G. S. McCarty and P. S. Weiss, *J. Am. Chem. Soc.*, 2004, **126**, 16772–16776.
19 M. Xi and B. E. Bent, *Surf. Sci.*, 1992, **278**, 19–32.
20 L. Lafferentz, F. Ample, H. Yu, S. Hecht, C. Joachim and L. Grill, *Science*, 2009, **323**, 1193–1197.

Supplementary Material (ESI) for Chemical Communications

Supporting Information

Substrate Mediated Synthesis of 2D Covalent Organic Frameworks

Rico Gutzler*[a], Hermann Walch[a], Georg Eder[a], Stephan Kloft[a], Wolfgang M. Heckl[a,b], and Markus Lackinger[a]

Department of Earth and Environmental Sciences and Center for NanoScience (CeNS), Ludwig-Maximilians-University, Theresienstrasse 41, 80333 Munich, Germany; Deutsches Museum, Museumsinsel 1, 80538 Munich, Germany

Contents

I. Experimental procedures

All experiments are carried out under UHV conditions (base pressure $<5.0 \times 10^{-10}$ mbar) at room temperature with two different STMs. One instrument is a commercial STM from Omicron whereas the other one a home-built beetle type STM as described elsewhere.[1] Both STMs are laterally calibrated by atomically resolved graphite images. 1,3,5-Tris(4-bromophenyl)benzene (TBB) is supplied by Sigma-Aldrich with a purity of 97% and extensively (>48 h) outgassed in UHV at 140°C. TBB is deposited from Knudsen cells with a crucible temperature in the range from 140 °C to 160 °C. The graphite surface is cleaned prior to experiments by annealing up to 500 °C for 30 minutes. Ag(110) and Cu(111) surfaces are cleaned by repeated cycles of sputtering and annealing. Cleanliness of the substrate is checked prior to evaporation by STM. During deposition, the substrate is held at room temperature. Thermal stability of 2D COFs is verified by annealing of a previously characterized sample and subsequent repeated STM measurements.

II. Additional STM data

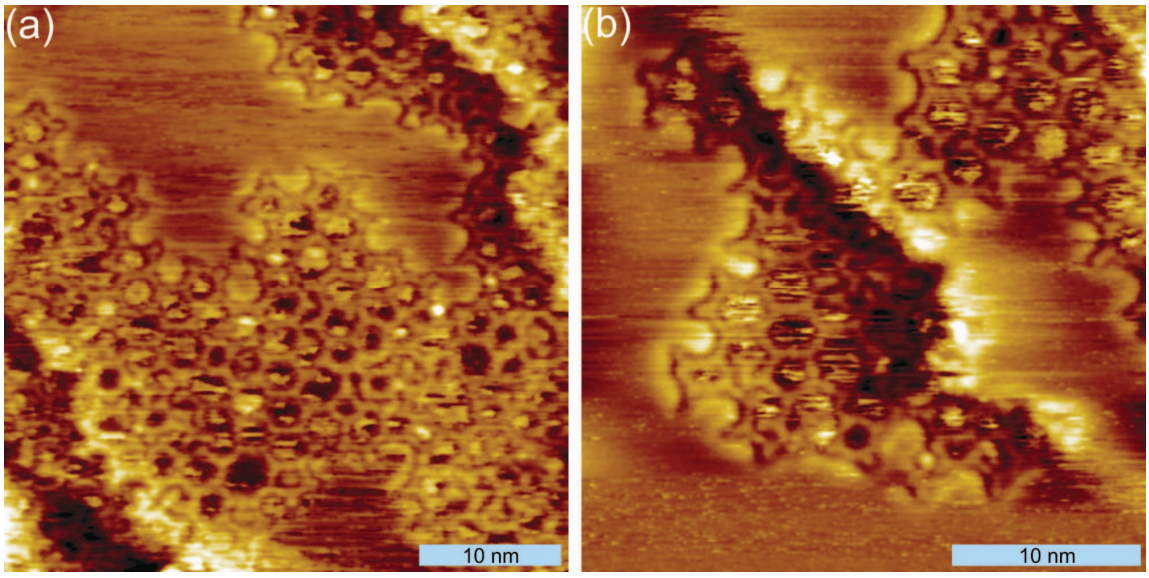

Figure S1. TBB evaporated on Ag(110) at 140 °C for 10 min **(a)** V = 1.2 V, I = 110 pA **(b)** V = 1,2 V, I = 123 pA. Both topographs show open-pore structures with high defect density. The contrast within the cavities can be attributed to coadsorbed molecules or split-off bromine atoms.

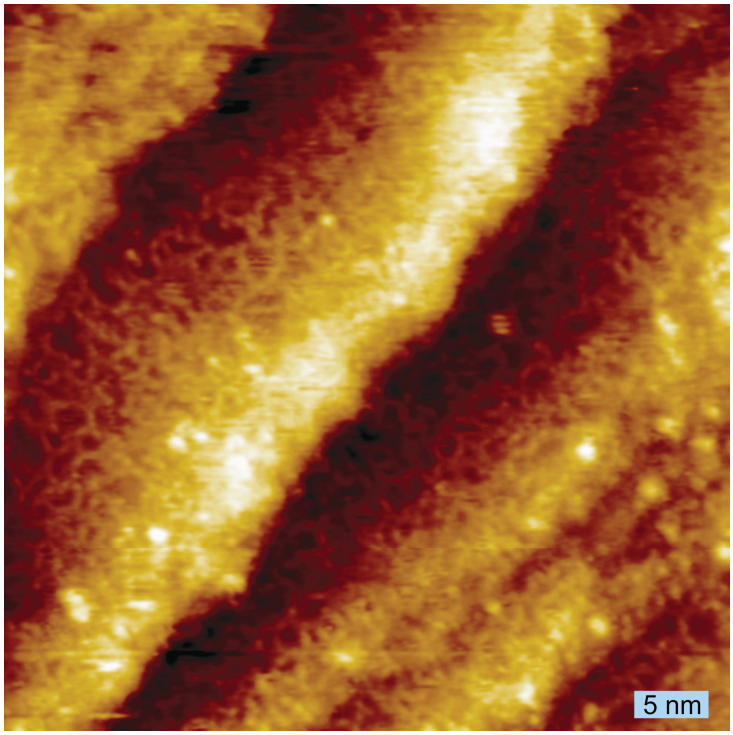

Figure S2. TBB evaporated on Cu(111) and annealed to 400 °C for 20 min (V = 1.3 V, I = 170 pA). The formerly covalent network is degraded and no ordered structure can be observed.

III. Forcefield and DFT calculations

The geometry of covalent organic frameworks is optimized by means of molecular mechanics simulations, conducted with the Cerius[2] (Version 4.5, MSI) software package and the Dreiding forcefield.[2] Periodic boundary conditions are applied to a hexagonal lattice with p6 symmetry and the lattice parameter is varied in order to find the minimum energy configuration. Free standing monolayers, i.e. without substrate influence are simulated. An energy difference of $< 2\times10^{-5}$ kcal/mol between single steps serves as a convergence criteria in all calculations.

The minimum energy is found for a lattice parameter of 2.21(2) nm (cf. Fig. S3) in agreement with the experimentally deduced value of 2.2 nm. Fig. S3 depicts the calculated values for the total energy as a function of lattice parameter. This lattice parameter corresponds to a distance of 1.28 nm between adjacent molecules.

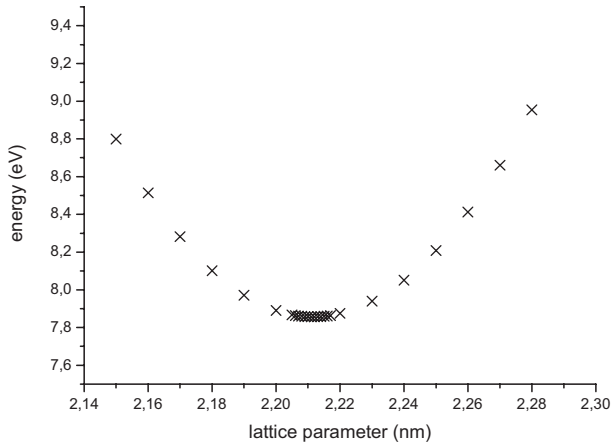

Figure S3. Calculated energy per unit cell for the geometry optimized framework as a function of lattice parameter according to molecular mechanics simulations. The isolated monolayer is fixed to p6 symmetry. A lattice parameter of 2.21(2) nm yields the minimum energy.

The geometry of an ideal hexagonal 2D COF is also optimized by density functional theory (DFT) calculations implemented in the Gaussian03 software package.[3] For this purpose, the B3LYP functional with 6-31G(d) basis set is used. Periodic boundary conditions are employed, the substrate is neglected. The input geometry is that of the previously force-field optimized geometry with p6 symmetry. Lattice parameter and angle are allowed to vary. Standardized convergence criteria as preset in Gaussian03 are used. The structure optimization yields lattice parameter of 2.245 nm and 2.243 nm and an angle of 120.02°. Adjacent phenyl rings are tilted by ~60° with respect to each other because of steric hindrance. Since the rotational barrier for a biphenyl is relatively low, interaction with the substrate is likely to cause planar adsorption as experimentally observed in the STM topographs.

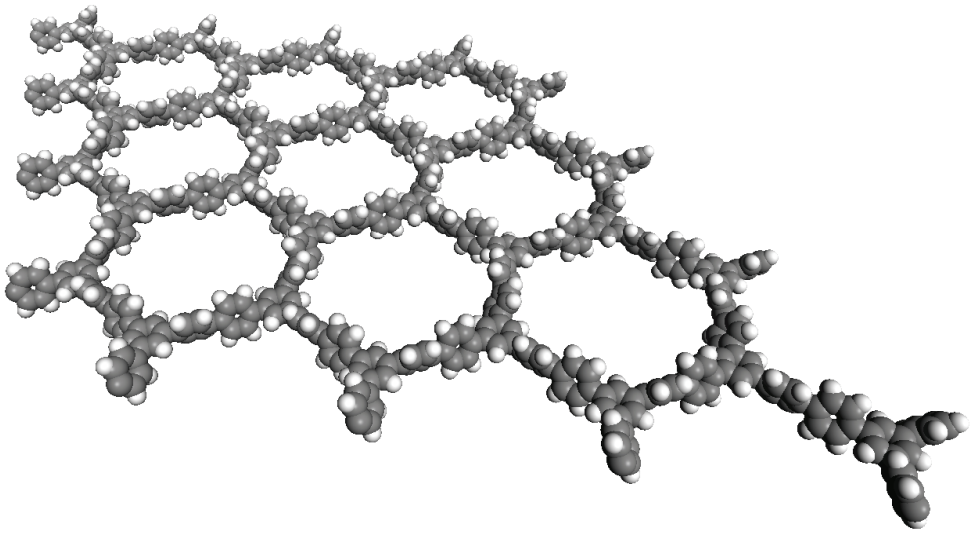

Figure S4. Model of an ideal hexagonal covalent organic framework. The geometry corresponds to the output of the DFT calculation with the above stated lattice parameters. Phenyl rings are tilted by about 60° with respect to each other.

IV. Thermogravimetric analysis

In an inert atmosphere, approximately 50 mg of TBB are heated with a rate of 1 °C per minute and the weight loss recorded. Degradation sets in at about 250 °C and is largely completed at ~375 °C. A residual of 4% of the original weight of sample remains. The temperature range for deposition by means of vacuum sublimation is 140° - 160°C as indicated by the colored bar in Fig S5 and is significantly lower than the decomposition temperature. Thus, the conclusion that intact molecules arrive at the surface can be drawn.

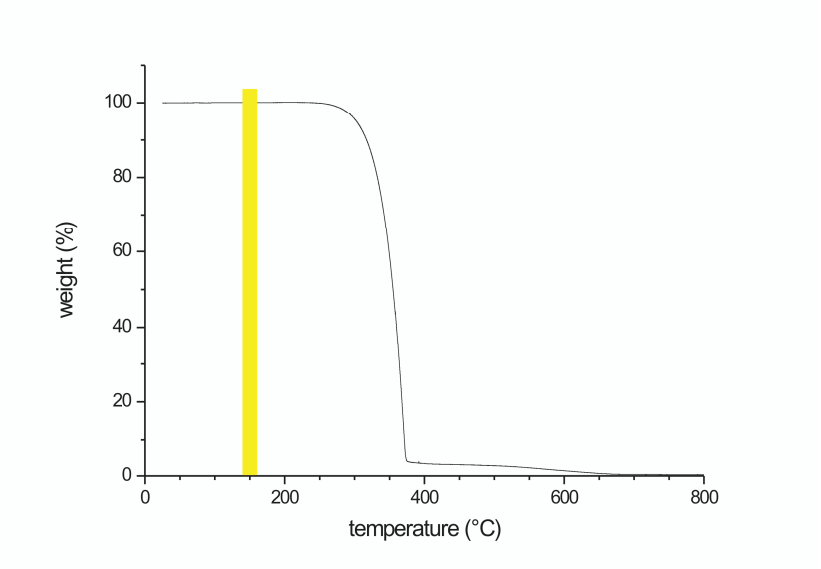

Figure S5. Thermogravimetric analysis of TBB. The colored area indicates the temperature range applied for thermal sublimation.

V. UV/Vis spectra

In order to support the hypothesis that TBB molecules remain intact upon vacuum sublimation, UV/Vis spectroscopy is conducted with n-hexane as solvent. A quartz glass cuvette with an optical path length of 1 mm is used. Unsubstituted 1,3,5-triphenylbenzene (TPB) serves as a control substance. Because of its significantly higher solubility, TPB solutions are diluted by a factor 30, whereas for TBB saturated solutions are used. Three different TBB solutions are prepared and compared: TBB as provided, TBB sublimated once onto the shutter, TBB residuals from the crucible of the Knudsen cell.

In the wavelength range from 200 nm to 500 nm, all absorption spectra exhibit two main peaks (see Fig. S6). For all three TBB solutions these two peaks are centered at the same wavelength, namely λ_1=206 nm and λ_2=260 nm. While for unsubstituted TPB the peak at longer wavelength is slightly blue-shifted and centered at λ_2=250 nm, thereby demonstrating the influence of the Br substitution. Because for all three TBB solutions the shape of the spectra and the peak positions remain the same, we conclude that both thermally sublimed molecules and molecules from the crucible which were held at a temperature of 140 °C - 160 °C for extended amounts of time remain intact.

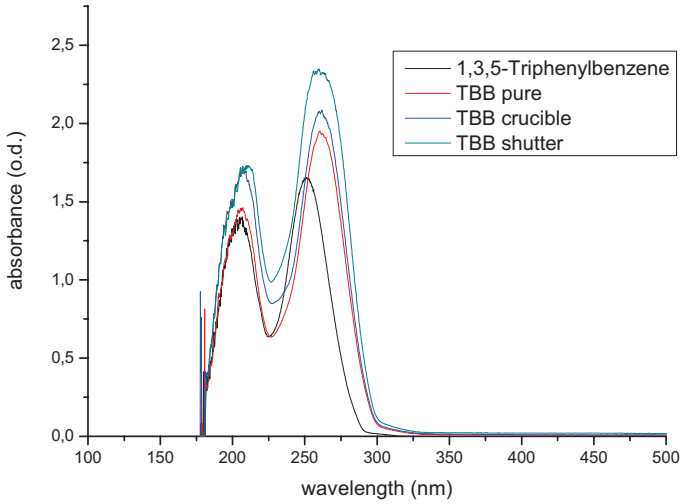

Figure S6. UV/Vis absorption spectra of TBB (saturated solutions) and 1,3,5-Triphenylbenzene (1:30 diluted solutions) in n-hexane

(1) Stipe, B. C.; Rezaei, M. A.; Ho, W. *Rev. Sci. Instrum.* **1999**, *70*, 137-143.

(2) Mayo, S. L.; Olafson, B. D.; Goddard, W. A. *J. Phys. Chem.* **1990**, *94*, 8897-8909.

(3) Frisch, M. J.; Trucks, G. W.; Schlegel, H. B.; Scuseria, G. E.; Robb, M. A.; Cheeseman, J. R.; Montgomery, J., J. A.; Vreven, T.; Kudin, K. N.; Burant, J. C.; Millam, J. M.; Iyengar, S. S.; Tomasi, J.; Barone, V.; Mennucci, B.; Cossi, M.; Scalmani, G.; Rega, N.; Petersson, G. A.; Nakatsuji, H.; Hada, M.; Ehara, M.; Toyota, K.; Fukuda, R.; Hasegawa, J.; Ishida, M.; Nakajima, T.; Honda, Y.; Kitao, O.; Nakai, H.; Klene, M.; Li, X.; Knox, J. E.; Hratchian, H. P.; Cross, J. B.; Bakken, V.; Adamo, C.; Jaramillo, J.; Gomperts, R.; Stratmann, R. E.; Yazyev, O.; Austin, A. J.; Cammi, R.; Pomelli, C.; Ochterski, J. W.; Ayala, P. Y.; Morokuma, K.; Voth, G. A.; Salvador, P.; Dannenberg, J. J.; Zakrzewski, V. G.; Dapprich, S.; Daniels, A. D.; Strain, M. C.; Farkas, O.; Malick, D. K.; Rabuck, A. D.; Raghavachari, K.; Foresman, J. B.; Ortiz, J. V.; Cui, Q.; Baboul, A. G.; Clifford, S.; Cioslowski, J.; Stefanov, B. B.; Liu, G.; Liashenko, A.; Piskorz, P.; Komaromi, I.; Martin, R. L.; Fox, D. J.; Keith, T.; Al-Laham, M. A.; Peng, C. Y.; Nanayakkara, A.; Challacombe, M.; Gill, P. M. W.; Johnson, B.; Chen, W.; Wong, M. W.; Gonzalez, C.; Pople, J. A. *Gaussian, Inc., Wallingford CT* **2004**.

Combination of a Knudsen effusion cell with a quartz crystal microbalance: *In situ* measurement of molecular evaporation rates with a fully functional deposition source

Rico Gutzler,[1] Wolfgang M. Heckl,[2,3] and Markus Lackinger[1]
[1]*Department of Earth and Environmental Sciences and Center for NanoScience (CeNS), Ludwig-Maximilians-University, Theresienstrasse 41, Munich 80333, Germany*
[2]*Deutsches Museum, Museumsinsel 1, Munich 80538, Germany*
[3]*Department of Physics, TUM School of Education, Technical University Munich, Schellingstrasse 33, Munich 80333, Germany*

(Received 12 November 2009; accepted 21 December 2009; published online 25 January 2010)

We describe a straightforward, reliable, and inexpensive design of a Knudsen type molecular effusion cell capable of measuring molecular evaporation rates *in situ*. This is accomplished by means of a quartz crystal microbalance integrated into the shutter of the effusion cell. The presented layout facilitates both the measurement of effusion rates under ultrahigh vacuum conditions without the need for a separate experimental setup and the growth of surface supported molecular layers and nanostructures. As an important prerequisite for reproducible deposition of molecular films with defined coverages ranging from submonolayers up to multilayers, the Knudsen cell features a stable deposition rate for crucible temperatures between 50 and 500 °C. Experimental determination of deposition rates for different crucible temperatures allows to approximate sublimation enthalpies of the evaporant based on the Clausius–Clapeyron equation. © *2010 American Institute of Physics.* [doi:10.1063/1.3292510]

I. INTRODUCTION

In organic molecular beam epitaxy (OMBE), the deposition rate of molecules is a crucial parameter for the defined fabrication of molecular thin films.[1] A widespread application of OMBE in basic research is the deposition of organic molecules on crystalline substrates for the subsequent investigation via surface sensitive techniques such as scanning tunneling microscopy, atomic force microscopy, or low-energy electron diffraction.[2] Since the emergence of distinct phases and possible phase transitions can depend on coverage,[3] both the precise coverage and deposition rate are extremely important parameters for reproducible sample preparation. Especially heteromeric molecular systems which consist of more than one molecular species are commonly prepared by simultaneous deposition from independent sources. In order to attain a defined stoichiometry, relative evaporation rates of the various single constituents have to be known and adjusted precisely.[4] Determining deposition rates can be tedious and time consuming and methods to make this procedure simpler and more efficient are greatly demanded.

Various parameters determine the effusion and deposition rate respectively: Besides the mutual geometric arrangement of source and sample, also the area of the crucible aperture influences the effusion rate of sublimable molecules. Furthermore, the effusion rate inherently depends on the sublimation enthalpy ΔH_{sub} of the respective compound. This in principle temperature-dependent material parameter is influenced by the structure and size of the molecule as well as intermolecular binding forces. For many novel synthesized molecules, tailored according to the requirements of crystal engineering, the sublimation enthalpy and thus the sublimation temperature which yields the desired evaporation rate are both unknown. Also, building blocks for supramolecular self-assembly are becoming increasingly more complex and consequently some molecules are already too large and fragile to withstand the temperatures required for their thermal sublimation. Decomposition sets in before the compound sublimes. In order to save valuable instrument time it would be very desirable to know beforehand whether the targeted compound is sublimable at all. This question can in principle also be economically addressed with our setup.

The design of the Knudsen cell presented here is thus motivated by the requirement to measure evaporation rates in a straightforward and inexpensive setup which readily allows to estimate the sublimation temperature for further experiments, but is also usable as fully functional deposition source. In contrast to previous Knudsen cell assemblies,[5] determination of evaporation rates and molecular deposition is now possible with the same setup. Additionally, sublimation enthalpies can be approximated from evaporation rates measured at different temperatures by applying the Clausius–Clapeyron equation.

The proposed Knudsen cell operates under ultrahigh vacuum (UHV) conditions. Sublimated molecules adsorb onto a quartz crystal microbalance (QCMB) which is integrated into a rotatable shutter and read out by standard external electronic circuits. The Knudsen cell allows for the measurement of molecular evaporation rates for crucible temperatures ranging from 50 up to 500 °C as well as for the deposition of molecules onto substrates. The whole setup is realized on a common single conflat (CF) 35 flange and is

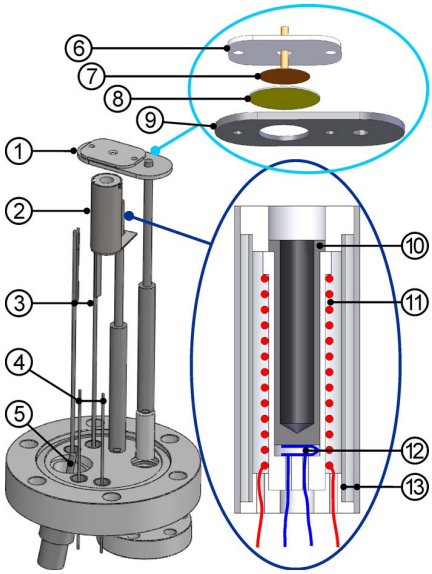

FIG. 1. (Color online) Design of the molecular evaporator. (1) Rotatable shutter with integrated QCMB. One electrode of the QCMB crystal is connected to a coaxial cable and isolated by a macor plate. The whole shutter is attached to a rotary feedthrough. (2) Knudsen cell. (3) Thermocouple feedthrough (type *K*), connected to (12). (4) Power feedthroughs for filament current, connected to (11). (5) BNC signal feedthrough (grounded to body) connected to the quartz crystal via a coaxial cable. (6) Macor plate clamping QCMB. (7) Copper plate connecting back electrode of QCMB to coaxial cable. (8) Quartz crystal. (9) Stainless steel shutter with 10 mm orifice. (10) Molybdenum crucible housed and stabilized by macor holders and spacers. (11) Heating coil made from 0.3 mm tantalum wire. (12) Thermocouple attached to a flat spring to assure good thermal connection to the crucible. (13) Two stainless steel radiation shields to minimize heat loss to the environment.

thus ideally suited for implementation in UHV systems. The performance is demonstrated by evaluation of estimated sublimation enthalpies for selected compounds.

II. CONSTRUCTION

The whole setup (cf. Fig. 1) is mounted onto a single CF 35 flange which includes power feedthroughs for the filament current, type *K* thermocouple feedthroughs for an accurate temperature measurement, and a grounded BNC feedthrough for the high frequency signal driving the QCMB. Centerpiece of the Knudsen cell is a molybdenum crucible which is housed by a macor holder. This holder is resistively heated by a 0.3 mm tantalum wire which is wrapped around the macor holder with a defined coil density. Macor, a machinable ceramic, is rated for operation temperatures up to 600 °C and thus adequate for a molecular evaporator. The thermocouple is pushed onto the bottom of the crucible by means of a spring. Radiation heat loss is minimized by two isolated stainless steel radiation shields surrounding the crucible assembly. The base flange also includes a CF 16 half nipple in order to mount a standard rotary feedthrough for shutter operation. The beam shutter (stainless steel) is designed to hold a standard quartz microbalance crystal (nominal eigenfrequency 6 MHz, diameter 1.4 cm) and can be positioned directly above the aperture of the crucible. The signal of the QCMB is transmitted to the BNC feedthrough via an UHV compatible coaxial cable. The quartz crystal is grounded via the stainless steal shutter and rotary feedthrough. Independent grounding of both the quartz crystal and the BNC feedthrough was not necessary for stable operation. The close proximity of the quartz crystal and its large size in comparison to the aperture size of the Knudsen cell guarantees a high adsorption probability of effused molecules and hence a high sensitivity of the setup. In contrast to other, more sophisticated assemblies with a cooled QCMB, the proposed instrument does not require any external means for temperature stabilization. For instance, a dwell time of ~10 min is sufficient to equilibrate the system when the temperature is increased in steps of 5–10 °C. This is owed to the good thermal isolation of the heating filament and the low temperature coefficient of the AT cut quartz crystals.

III. OPERATION

In order to verify the function of the QCMB, evaporation rates were monitored at different sublimation temperatures for commercially available compounds. The crucible temperature was held constant at a user-defined set point temperature within ±0.5 °C by means of a temperature controller (Eurotherm 2416) and a downstream power supply. Two different molecules were tested: 1,3,5-triphenylbenzene (TPB) and 1,3,5-tris(4-bromophenyl)benzene (TBB). Both compounds were acquired from a commercial source (Sigma-Aldrich) and used without further purification. Prior to measurements, the crucible containing the molecules was extensively outgassed.

The accumulation of TPB and TBB on the quartz crystal as a function of deposition time is plotted in Figs. 2(a) and 2(b), respectively, for a series of different crucible temperatures (from 80 to 100 °C for TPB and from 130 to 170 °C for TBB). According to Sauerbrey's equation,[6] the accumulated mass Δm was calculated from the eigenfrequency shift of an excited shear mode. For thin layers of low density organic material, this approximation remains valid even for use over extended periods of time. For each temperature T, the mass Δm deposited on the QCMB increases linearly with deposition time t. This indicates a constant flux and thus deposition rate of molecules from the crucible on the quartz crystal, provided that the sticking coefficient remains constant (not necessarily unity). As anticipated, the deposition rates increase monotonously with crucible temperature. From these temperature-dependent measurements of deposition rates the sublimation enthalpy of the evaporant can be extracted based on the well-established assumption that measured deposition rates are proportional to the vapor pressure of the compound in the crucible. In this case, the vapor pressure p in the Clausius–Clapeyron equation $\ln p \propto -\Delta H_{\mathrm{sub}}/k_B T$ can be expressed through the magnitude of the deposition rate or the absolute value of the eigenfrequency shift per time $|\Delta f/\Delta t|$, respectively. The sublimation enthalpy ΔH_{sub} can conveniently be extracted from the slope in Arrhenius plots of experimentally determined pairs of $\Delta f/\Delta t$ and corresponding crucible temperature T. For TPB this procedure results in a sublimation enthalpy of

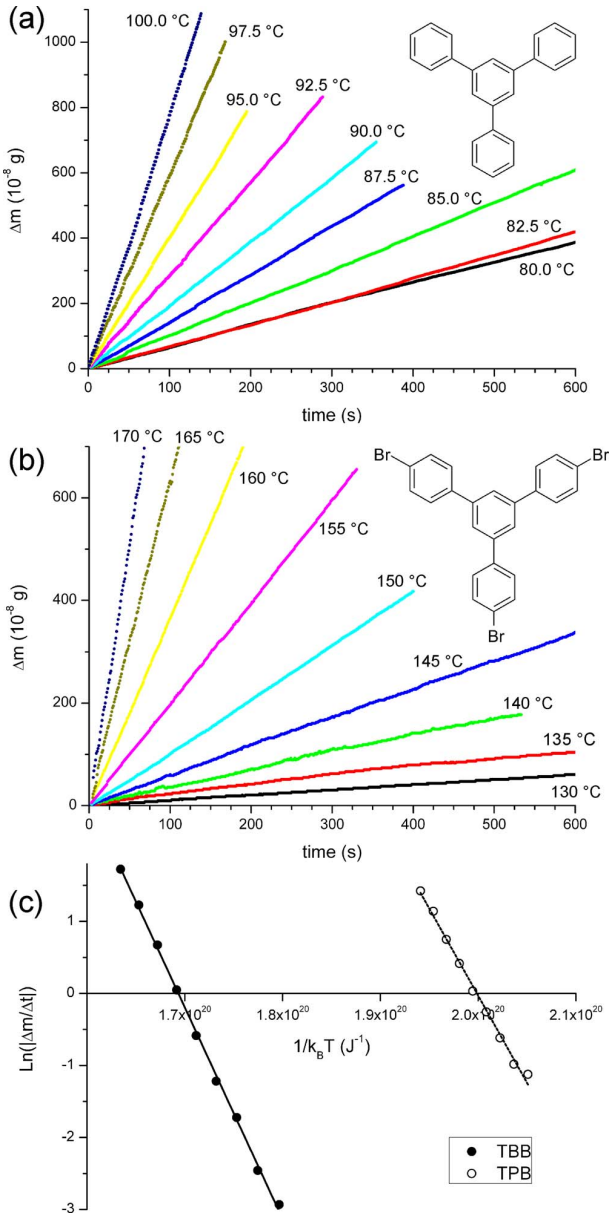

FIG. 2. (Color online) (a) Accumulated mass of TPB molecules on the QCMB as a function of deposition time at different evaporation temperatures (inset: chemical structure of TPB). A linear mass increase with time is perceptible for all temperatures (from 80 to 100 °C). The slope of the straight lines increases with evaporation temperature and yields the rate of molecular deposition. (b) Same for TBB. (c) Arrhenius plot of deposition rates versus evaporation temperature from (a) and (b). The sublimation enthalpy of the respective compound can be extracted from the slope.

(146 ± 4) kJ mol^{-1} [cf. Fig. 2(c)]. Within the error margin this value is equal to the recommended value in literature of (149.8 ± 1.6) kJ mol^{-1}.[7] The latter value is stated for a temperature of 25 °C and the difference might be owed to the temperature dependence of the sublimation enthalpy. Higher temperatures diminish the sublimation enthalpy by an amount proportional to the heat capacity of the substance. In the same way the sublimation enthalpy of TBB was estimated to be (177 ± 3) kJ mol^{-1} [cf. Fig. 2(c)], but for this specific compound no literature value is available for comparison.

By means of the rotary feedthrough the QCMB can be rotated away, thereby unblocking the molecular beam and enabling deposition on substrates. Thus, the proposed setup also offers the possibilities of a fully functional deposition source for OMBE.

This combined apparatus also allows determining the sublimation temperature which features the required molecular flux already during the mandatory outgassing procedure of newly introduced compounds, thereby saving valuable time. Also, provided the impurity molecule is sufficiently large to stick to the QCMB, the outgassing and purification procedure can be monitored quantitatively.

There are still further advantages to the proposed setup: the deposition rate versus crucible temperature curves can serve as a calibration standard for a specific compound which enables to determine the required temperature when a defined change in deposition rate is envisaged. Furthermore, if experimentally determined deposition times are inconveniently short or long, the calibration curve allows to recalculate more practical values for deposition parameters, i.e., crucible temperature and deposition time. Moreover, the setup enables one to check whether the sublimation rate for a given temperature remains constant over extended periods of time between different experimental runs. Fluctuations in the deposition rate for constant temperature are a common source for irreproducibility in OMBE experiments. The possibility to control the stability of the deposition rate is particularly interesting for chemically reactive compounds which might already react in the crucible, thereby also affecting the sublimation rate.[4]

IV. CONCLUSION

The simple and inexpensive setup presented here for a Knudsen cell type molecular evaporator is capable of monitoring evaporation rates over a wide range of temperatures (from 50 to 500 °C) by means of an integrated QCMB. It works reliably under UHV conditions and allows deposition of organic molecules in a precisely defined coverage onto substrates at constant flux. The coverage of molecules on surfaces can be fine tuned based on previously recorded deposition versus crucible temperature calibration curves, thus facilitating excellent control over important experimental parameters. Furthermore, evaporation rates measured for different crucible temperatures can be used to estimate sublimation enthalpies of organic compounds. The performance of the Knudsen cell is demonstrated by recording deposition rates for selected compounds (TPB and TBB) and calculating sublimation enthalpies which are in good agreement with previously reported values.

ACKNOWLEDGMENTS

Financial support by the Deutsche Forschungsgemeinschaft (Grant No. SFB 486) and Nanosystems Initiative Munich (NIM) is gratefully acknowledged.

[1] S. R. Forrest, Chem. Rev. **97**, 1793 (1997); S. Kowarik, A. Gerlach, and F. Schreiber, J. Phys.: Condens. Matter **20**, 184005 (2008).
[2] J. V. Barth, Annu. Rev. Phys. Chem. **58**, 375 (2007); S. A. Burke, J. M. Topple, and P. Grütter, J. Phys.: Condens. Matter **21**, 423101 (2009); W.

Moritz, J. Landskron, and M. Deschauer, Surf. Sci. **603**, 1306 (2009).
[3] Y. Ye, W. Sun, Y. Wang, X. Shao, X. Xu, F. Cheng, J. Li, and K. Wu, J. Phys. Chem. C **111**, 10138 (2007); M. Stöhr, M. Wahl, C. H. Galka, T. Riehm, T. A. Jung, and L. H. Gade, Angew. Chem., Int. Ed. **44**, 7394 (2005).
[4] N. A. A. Zwaneveld, R. Pawlak, M. Abel, D. Catalin, D. Gigmes, D. Bertin, and L. Porte, J. Am. Chem. Soc. **130**, 6678 (2008).
[5] A. L. F. de Barros, A. Medina, F. Zappa, J. M. Pereira, E. Bessa, M. H. P. Martins, L. F. S. Coelho, W. Wolff, and N. V. de Castro Faria, Nucl. Instrum. Methods Phys. Res. A **560**, 219 (2006); A. Freedman, P. L. Kebabian, Z. Li, W. A. Robinson, and J. C. Wormhoudt, Meas. Sci. Technol. **19**, 125102 (2008); A. K. Shukla, S. Banik, R. S. Dhaka, C. Biswas, and S. R. Barman, Rev. Sci. Instrum. **75**, 4467 (2004).
[6] G. Sauerbrey, Z. Phys. **155**, 206 (1959).
[7] M. V. Roux, M. Temprado, J. S. Chickos, and Y. Nagano, J. Phys. Chem. Ref. Data **37**, 1855 (2008).

Influence of Solvophobic Effects on Self-Assembly of Trimesic Acid at the Liquid−Solid Interface

Nguyen T. N. Ha,[†,§] Thiruvancheril G. Gopakumar,*[,†,⊥] Rico Gutzler,[‡] Markus Lackinger,[‡] Hao Tang,[∥] and Michael Hietschold[†]

Institute of Physics, Solid Surfaces Analysis Group, Chemnitz University of Technology, D-09107 Chemnitz, Germany, Department for Earth and Environmental Sciences and Center for NanoScience (CeNS), Ludwig-Maximilians-University, Theresienstr. 41, D-80333 Munich, Germany, Department of Applied Physics, Faculty of Physics, University of Natural Sciences, 227 Nguyen Van Cu, Ho Chi Minh City, Vietnam, and CNRS, CEMES (Centre d'Elaboration des Matériaux et d'Etudes Structurales), BP 94347, 29 rue J. Marvig, F-31055 Toulouse, France, and Université de Toulouse, UPS, F-31055 Toulouse, France

Received: August 12, 2009; Revised Manuscript Received: January 17, 2010

Despite the multitude of surface supported monolayer structures already reported for trimesic acid (TMA), new self-assembled structures are still discovered, depending on conditions and environment. This exemplifies the versatility of this archetypical supramolecular building block and justifies its role as a model system. At the interface between 1-phenyloctane (PO), a highly nonpolar solvent, and graphite, a new densely packed and partly hydrogen-bonded TMA structure is observed by means of scanning tunneling microscopy (STM). Normally, the TMA solubility in PO is too low to allow for self-assembly of interfacial monolayers. However, as verified by UV−vis spectroscopy, sonication of solutions with TMA sediment increases the amount of dissolved solute molecules. Consequently, the self-assembly of interfacial monolayers can be observed with these enriched solutions. In contrast to many other structures reported, the observed monolayers are densely packed and composed of partly hydrogen-bonded TMA molecules that form zigzag chains. The proposed structural model is derived from semiempirical quantum chemistry methods, which also provide the basis for STM image simulations by means of a scattering formalism. Solvophobic effects are likely to account for both, low TMA solubility in PO and the high packing density of the interfacial monolayer.

Introduction

Molecular self-assembly is the basic concept of supramolecular chemistry where preexistent building blocks spontaneously assemble into ordered aggregates by means of noncovalent interactions. In the design of supramolecular structures, chemists take advantage of various interactions, such as electrostatic, hydrogen bonding, $\pi-\pi$ interaction, metal coordination, and chelate effects.[1–5] Because of their cooperativity, selectivity, and directionality, hydrogen bonds are the most important interaction.[2] However, the finial supramolecular structure is not exclusively encoded in the building block but can also depend on the conditions under which self-assembly takes place. In particular, at the liquid−solid interface, the solvent is more than just a reservoir and transport medium for building blocks but can influence self-assembly in several ways.[6–9]

Because of its versatility, trimesic acid (TMA) has advanced to a model system for understanding the complex interactions that drive self-assembly, both in three and two dimensions. For the self-assembly of surface supported monolayers, various different TMA structures are reported for the solid−liquid and the solid−vacuum interfaces.[10–13] Also, TMA has proven to be a suitable building block for heteromeric self-assembly.[14–16] In homomeric TMA structures, two principally different adsorption geometries can be distinguished: TMA molecules adsorb either planar or (nearly) upright to the surface, although planar adsorption prevails. On a graphite substrate, TMA adsorbs planar and typically assembles into one of two commonly observed nanoporous polymorphs, the low packing density "chicken wire" and a higher packing density "flower" structure. Again, both structures can be observed at the liquid−solid interface and for vacuum deposited monolayers.[10,11] At the solid−vacuum interface, both polymorphs can coexist, whereas at the liquid−solid interface, a particular solvent stabilizes an individual structure. By means of vacuum deposited monolayers on Au(111) with increasing coverage, Ye et al. demonstrated that these two structures are special cases within a systematic series.[17] For this series, the highest packing density reported is 1.34 molecules/nm^2, a value that has never been reached or exceeded at the solid−liquid interface, though it was predicted.[10] Higher monolayer surface packing densities are only attained for perpendicular adsorption of TMA due to the smaller footprint. Such an arrangement is observed for electrochemically controlled experiments at the liquid−solid interface, likewise on Au(111).[18] Transitions from planar to perpendicular adsorption can be induced by tuning the potential to positive values. In this case, TMA adsorbs with one deprotonated carboxylic group chemisorbed to the surface, while the other two carboxylic groups remain protonated and point off the surface.[18]

Planar adsorption of TMA is advantageous for $\pi-\pi$ interaction between the aromatic systems of the graphite substrate and the molecule but also facilitates intermolecular hydrogen bonds. In most of the homomeric TMA structures reported, all three

* To whom correspondence should be addressed. E-mail: thiruvancheril.gopakumar@physik.tu-chemnitz.de.
[†] Chemnitz University of Technology.
[‡] Ludwig-Maximilians-University.
[§] University of Natural Sciences.
[∥] University of Toulouse.
[⊥] Present address: Institut für Experimentelle and Angewandte Physik, Christian-Albrechts-Universität zu Kiel, D-24118 Kiel, Germany.

10.1021/jp907781a
Published on Web 02/08/2010

carboxylic groups of TMA are involved in either cyclic dimer or cyclic trimer binding motifs. For instance, in the chicken wire structure, all intermolecular hydrogen bonds are realized through cyclic dimers, whereas in the flower structure, one-third of the carboxylic groups take part in a cyclic trimer arrangement. In the aforementioned series of nine TMA structures on Au(111), the ratio between cyclic trimers and dimers monotonously increases with surface coverage. In contrast, the structure that we report on here is anomalous: TMA molecules do adsorb planar, but only two-thirds of the carboxylic groups take part in cyclic intermolecular hydrogen bonds. These results give rise to interesting questions concerning the influence of the solvent that is anomalous as well, not generally for STM experiments at the liquid−solid interface, but for TMA. Phenyloctane (PO) is a solvent widely used for STM experiments at the liquid−solid interface because it combines various advantages: low affinity to the graphite substrate, low vapor pressure, no electrochemisty at moderate voltages, nonpolar as evident from the low static dielectric constant of $\varepsilon = 2.26$, and is also a nonprotic solvent, that is, does not exhibit functional groups for intermolecular hydrogen bonds. Because of the nonprotic nature of PO, the formation of structures that incorporate solvent molecules is not expected. Therefore, we have opted for PO as solvent to study the self-assembly of interfacial TMA monolayers on graphite.

Experiments

Due to the nonpolar and nonprotic nature of PO, a very low solubility of TMA can be anticipated. Consequently, experiments with saturated solutions do not yield self-assembled monolayers at the liquid−solid interface. To enhance the amount of TMA dissolved in PO, supersaturated solutions are prepared by sonication for uncommonly extended amounts of time (~5 h). This results in a colloidal (turbid) solution that is allowed to settle for 2 weeks. Decantation yields a clear stock solution for further experiments. Upon sonication, the amount of dissolved TMA increases with time. This was experimentally confirmed via UV−vis absorption spectroscopy of solutions that have been sonicated for progressively increasing amounts of time (Supporting Information, Figure S1). Comparison with a reference solution of known concentration reveals that sonication increases the TMA solubility in PO up to the order of 100 μM for 5 h of sonication. On the basis of similar experiments with fatty acid solvents, we can exclude that considerable fractions of TMA molecules are being destroyed by the sonication procedure: Sonication of TMA in octanoic acid for comparable time spans yields the well-known more dense flower structure instead of the commonly expected chicken wire structure (to be published). Yet, the flower structure is only feasible with intact TMA molecules, thereby proving that the energy density achieved by a standard lab sonicator is insufficient to decompose such small and stable molecules as TMA.

TMA and PO are purchased from Sigma Aldrich with purities > 99% and have been used as received. STM experiments are conducted with a home-built STM driven by a commercial SPM-100 electronics from RHK. Electrochemically etched tungsten tips are used as probes and have been checked on freshly cleaved graphite surfaces before ~5 μL of solution is applied by means of a micropipet. The public domain program package WSxM is used for data processing.[19]

Results and Discussion

Extensively sonicated TMA solutions in PO facilitate the self-assembly of TMA monolayers with high packing density; a typical constant current STM topograph is reproduced in Figure 1. The lower half depicts the data as measured, whereas the upper half has been mesh-averaged.[19] This procedure averages a deliberately chosen cutout over equivalent parts of the normally periodic original image. The precise locations of equivalent parts are identified by means of local maxima in the cross-correlation between the cutout and the original image and weighted by their respective height. The monolayer is composed of triangularly shaped protrusions aligned along rows running from lower right to upper left. The brightness of those rows, that is, the apparent height, is alternating, as indicated by thick and thin arrows. According to size and symmetry, each bright spot corresponds to a planar adsorbed single TMA molecule. Interestingly, these rows are not equally spaced but alternately exhibit a smaller (0.98 ± 0.03 nm) and larger (1.05 ± 0.03 nm) distance, even though the difference is hardly measurable. As already evident from the STM image, TMA molecules in adjacent rows that are separated by the smaller gap form dimers. The two TMA molecules that constitute the dimer are azimuthally rotated by 180° with respect to each other. Perpendicular to the rows, the molecules run along zigzag chains, as marked with a dashed line in Figure 1. Molecular zigzag chains have previously been observed for isophthalic acid (IA, 1,3-dicarboxylic acid) monolayers.[20] In this structure, IA molecules are interconnected by 2-fold hydrogen bonds and the zigzag pattern is owed to the structure of the building block, that is, the 120° angle between the two carboxylic groups at the 1,3 positions.

The azimuthal orientation of individual TMA molecules can be deduced from high-resolution topographs; an example is

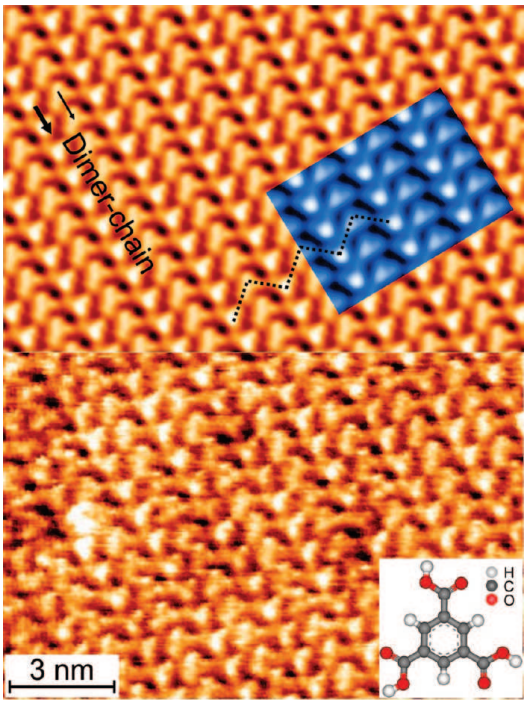

Figure 1. STM constant current topograph of a TMA monolayer at the graphite−phenyloctane interface. The lower half depicts the as-measured data ($V_{sample} = +1.4$ V, $I = 400$ pA), whereas the upper half represents mesh-averaged data, as explained in the text. TMA molecules are interconnected along zigzag chains, as marked with a dashed line in the image. Rows are indicated by the arrows running perpendicular to the zigzag chains. The apparent height of those rows (brightness) alternates; a higher and lower row is highlighted by a thick and thin arrow, respectively. The overlay represents a scaled STM image simulation ($V_{sample} = +1.6$ V, $I = 100$ pA), as further described in the text. Hard sphere model depicts single TMA molecule.

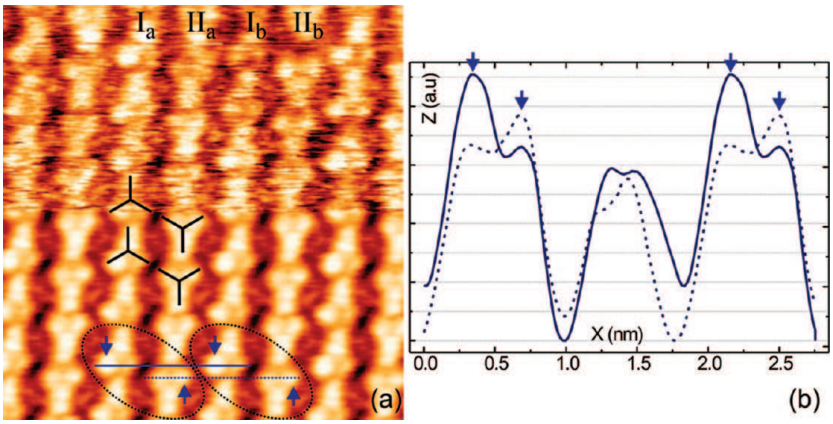

Figure 2. (a) Typical STM constant current topograph (9 × 15 nm^2, V_{sample} = +1.46 V, I = 450 pA) of TMA at the graphite−PO interface. The upper half depicts measured and the lower half mesh-averaged data. To guide the eye, TMA molecules are symbolized by tripods. Along the zigzag chains, TMA molecules dimerize, as indicated by dashed ovals. (b) Line profiles along the dashed and solid lines in (a), respectively; the line profiles illustrate the difference in apparent height and the asymmetry of single molecules. The solid (dashed) line in (a) corresponds to the solid (dashed) line in (b). Carboxylic groups that interlink rows I_a and II_a appear less bright.

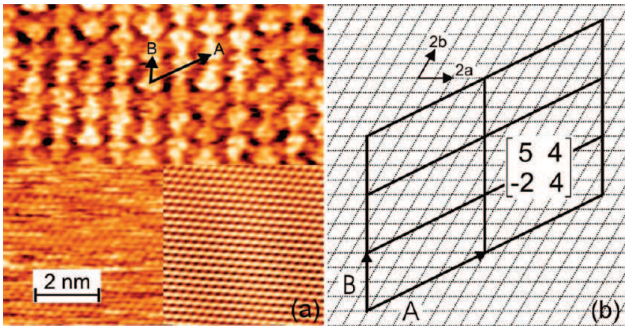

Figure 3. (a) Split image of a TMA monolayer; the upper half depicts the adsorbate layer with molecular resolution and the lower half the graphite lattice with atomic resolution (V_{sample} = +1.33/+0.133 V, I = 470 pA). The inset in the lower right corner is a Fourier filtered image of the graphite part. (b) Geometrical model of the epitaxial relation between TMA and graphite lattice. The monolayer structure is assumed to be commensurate; the origin is random. The inset denotes the superstructure matrix that relates the adsorbate to the substrate lattice vectors.

presented in Figure 2a. To guide the eye, TMA molecules are symbolized by tripods. The difference in apparent height between adjacent rows, as already evident in Figure 1, is further illustrated by line profiles. The topographically higher row is termed I, whereas the lower row is marked by II. Thus, perpendicular to the rows, there is a I−II···I−II pattern, where "−" symbolizes dimerization. As indicated by dashed ovals in Figure 2a, TMA molecules dimerize between rows I_a−II_a and I_b−II_b. Line profiles along the lines depicted in (a) are illustrated in 2b. The TMA lobes (carboxylic groups) that point between I_a and II_a along the dimer axis appear topographically low compared with that between II_a and I_b. In addition to the slight asymmetry between carboxylic groups, the overall difference in height between rows I and II prevails.

To obtain precise values for lattice parameters, the split-image technique was applied. Figure 3a depicts a split image of a TMA monolayer, where, in the upper half, the adsorbate layer is imaged with molecular resolution and, in the lower half, the graphite substrate with atomic resolution. This contrast switching is attained by rapidly lowering the sample bias by one order of magnitude from +1.33 to +0.133 V during image acquisition. The inset in the lower right corner of Figure 3a depicts an FFT filtered image of the graphite lattice. By means of this split image, the influence of thermal drift can be minimized and the epitaxial relation between adsorbate and substrate lattice, as presented in Figure 3b, can be determined. Because no further contrast modulation like a Moiré pattern is observed, commensurate epitaxy is assumed. Experimental and calculated lattice parameters from the deduced superstructure matrix are opposed in Table 1. Precise unit cell parameters provide the basis for an initial geometrical model and are an important experimental input for further simulations.

To understand the origin of dimer formation and the STM contrast modulation along the zigzag chains, we have carried out a structure optimization based on the last parametric method number 6 (PM6) implemented in the MOPAC2009 package.[21] MOPAC2009 is a semiempirical quantum chemistry method that treats hydrogen bonds better than molecular mechanics.[22,23] Our calculations are based on experimental lattice parameters with a periodic supercell containing two molecules adsorbed on two slabs of graphite. In a first step, all geometries are optimized with the atomic coordinates perpendicular to the surface fixed. In a second step, no further constraints are applied so that the final result represents fully relaxed atomic positions. Because the effect of the substrate on molecular binding energies is supposed to be small, the binding energies are calculated between two molecules as optimized on a graphite substrate but without including the molecule−graphite interaction in the binding energies. STM images have been simulated with a Green's function based scattering formalism.[24] This image simulation is based on the geometry-optimized structure from MOPAC calculations. The STM tip is approximated as a 3-fold symmetric pyramid of 10 W atoms adsorbed on a W(111) substrate. The electronic structure of the system as a prerequisite for the scattering formalism is calculated by the extended Hückel approximation. Results are presented in Figure 4, where (a) depicts a model of the optimized structure and (b) the simulated STM image.

The unit cell of this densely packed TMA monolayer accommodates two TMA molecules that are different with respect to their azimuthal orientation, adsorption site, and intermolecular bonds. In both nonequivalent TMA molecules, all carboxylic groups are involved in intermolecular hydrogen bonds; however, the hydrogen-bonding pattern is different for each of the three carboxylic groups in each nonequivalent TMA molecule. The numbering in the following discussion refers to the numbering of molecules in Figure 4a, where hydrogen bonds

TABLE 1: Experimental Values for the Unit Cell Parameters, As Determined by Split Images vs Unit Cell Parameters according to a Commensurate Unit Cell. The Bottom Row Depicts Lattice Parameters As Refined by a MOPAC Simulation with a Fully Relaxed Structure

	A (Å)	*B* (Å)	<*A*, *B*>	<*A*, *a*>	<*B*, *b*>
experiment	19.0 ± 0.5	9.0 ± 0.5	65 ± 2°	24 ± 2°	29 ± 2°
commensurate model	19.21	8.52	63.70°	26.33°	30.00°
MOPAC simulation	19.49	8.64	63.62°	26.30°	30.00°

TABLE 2: Calculated Binding Energies between Different Types of Hydrogen-Bonded TMA Dimers Using MOPAC2009 on Graphite

dimer[a]	Δ*E* kcal/mol
1−2	−34.925
2−4	−32.255
3−4/6−1	−9.479
2−5	−9.835

[a] The numbers refer to Figure 4. The energies of dimers are used only for comparison, since it is known that the absolute value of energies are overestimated by the methods used.

are indicated by blue arrows. Neighboring TMA molecules in adjacent rows are interconnected by two equivalent O−H···O hydrogen bonds between their carboxylic groups in a typical cyclic dimer motif. For the 2-fold hydrogen bond between molecules 1−2, the H···O distance amounts to 1.81 Å. Single O−H···O hydrogen bonds are also formed within the rows, for instance, between molecules 6−1 and 5−2. Those intrarow hydrogen bonds include the hydroxyl hydrogen atoms of molecules 6(5) and the hydroxyl oxygen atoms of molecule 1(2) with a slightly increased H···O distance of 1.89 Å. As evident from Table 2, the calculations reveal no significant difference between the binding energies of intrarow hydrogen bonds in the two nonequivalent rows I and II.

The hydrogen bonds between molecules 2−4 are also of the cyclic dimer type and qualitatively similar to the bonds between molecules 1−2. Yet, the H···O distance for 2−4 is slightly larger (1.83 Å) than that for 1−2, and accordingly, the binding energy is slightly higher (cf. Table 2). This asymmetry is attributed to the aforementioned symmetry breaking additional intrarow hydrogen bonds that only affect the local environment of hydroxyl oxygen atoms involved in the 2-fold hydrogen bond between molecules 1−2. Additional weak C−H···O interrow hydrogen bonds between molecules 1−6 and 2−5 are conceivable and might contribute to the stabilization. Yet, the H···O distance between the carboxy oxygen atoms of molecule 6(5) and a hydrogen atom of the phenyl ring of molecule 1(2) amounts to 2.53 Å and is rather large. This relatively large distance is attributed to steric repulsion between the hydroxyl hydrogen atom of molecule 6(5) and the hydrogen atom of the phenyl ring of molecule 1(2). As another consequence, the simulations indicate bending of the phenyl hydrogen, the carboxylic hydrogen, and oxygen atoms out of the molecular plane. Figure 4b illustrates the out-of-plane bending of the oxygen and hydrogen atoms in carboxylic groups, as marked by red and black arrows, respectively. The dotted line indicates the plane of the phenyl rings.

Figure 4c depicts the simulated STM image along with a mesh-averaged experimental STM image. The simulations nicely reproduce the different apparent heights of rows I and II. Also, the apparent heights of different carboxylic groups agree well between experiment and simulation. For a better comparison of the voids between molecular rows, black and white rectangles are included. Typically, the STM contrast is determined by both geometric and electronic effects, where hybridization of adsorbate and substrate electronic states can cause additional contrast alteration and modulation. In this case, we cannot unequivocally separate topographic from electronic effects. In addition to the asymmetrical binding, the MOPAC simulations indicate that the nonequivalent TMA molecules within the unit cell adsorb on different graphite lattice sites. TMA molecules in row I adsorb on α sites (C atom of the first layer with a next-nearest neighbor in the second layer), whereas molecules in row II adsorb on β sites (C atom of the first layer without a next-nearest neighbor in the second layer) (cf. Figure 4a). Because a contrast modulation as a consequence of different adsorption sites has also been observed for adsorbates on graphite and analyzed in great detail for aliphatic adsorbates, this epitaxial effect cannot be neglected.[25] To demonstrate the effect of different environments (i.e., in-plane binding arrangement and adsorption site on the STM contrast), we simulated STM topographs of a hypothetical superflower structure on graphite (Figure 5), where all TMA molecules exhibit the same 3-fold symmetric hydrogen-bonding pattern and are adsorbed on similar adsorption sites. As anticipated, the symmetry of the monolayer is reflected in the simulated STM image that exhibits ideal *p*3*m*1 symmetry. As for the observed zigzag dimer motif, TMA molecules appear with a triangular shape but do not show any internal asymmetry between the carboxylic groups. Three main reasons, therefore, account for the observed difference in apparent height between rows I and II: (1) nonequivalent electronic structure of TMA molecules in row I vs II, (2) out-of-plane bending of the hydroxyl and hydrogen in the −COOH group (see Figure 4b), and (3) different adsorption sites of molecules in row I vs II (see Figure 4a). However, it is difficult to separate each of these effects as they are closely linked. Most likely, a combination of several effects accounts for the experimental results.

To the best of our knowledge, the zigzag dimer-chain structure exhibits the highest packing density (1.29 ± 0.02 molecules/nm^2) of planar adsorbed TMA molecules ever observed at the graphite−liquid interface. Most abundant structures of TMA in fatty acids are porous flower and chicken wire structures.[10,11] On the other hand, TMA dimer chains have already been observed upon coadsorption with aliphatic alcohols.[16,26] For these structures, polar solvents are used for better TMA solubility. Under vacuum conditions, a densely packed TMA superflower structure has been observed on Au(111) with a lattice parameter of 9.3 Å, resulting in the highest packing density (1.34 molecules/nm^2) of all planar TMA monolayers.[17] To explain the formation of the zigzag structure at the graphite−PO interface, a hypothetical superflower structure on graphite was simulated and is depicted in Figure 5. A hexagonal structure with a lattice parameter of 9.84 Å is obtained, resulting in a molecular packing density of 1.19 molecules/nm^2, which is lower than that of the zigzag dimer chain (1.29 ± 0.02 molecules/nm^2).

The structure and epitaxy of many supramolecular monolayers at the liquid−solid interface are thermodynamically controlled and thus represent a minimum of Gibbs' free energy. This might also provide the key to understanding the formation of a densely packed TMA structure on the PO−graphite interface. Because

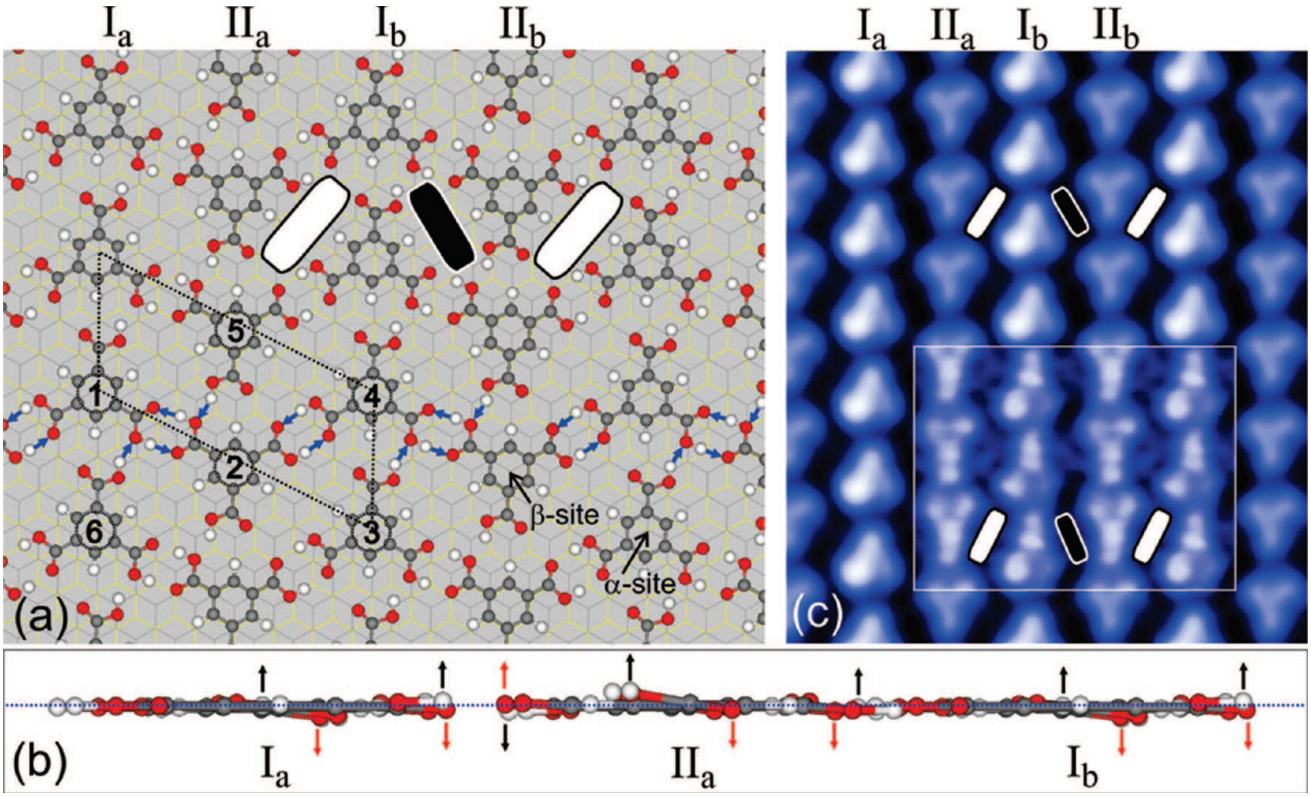

Figure 4. (a) Result of a MOPAC2009 semiempirical simulation of the zigzag dimer-chain TMA structure on graphite. Blue arrows indicate intermolecular hydrogen bonds. α and β sites denote the two nonequivalent C atoms of the topmost graphite layer. (b) Cross-sectional view of I_a, II_a, and I_b along 6−1/2−5 in which red and black arrows indicate vertical shifts of the hydroxyl oxygen and hydrogen atoms out of the adlayer plane, respectively. (c) Simulated STM image ($V_{sample} = +1.6$ V, 100 pA); the geometric structure is based on MOPAC results, and the electronic structure has been evaluated by extended Hückel calculations. For better comparison, a scaled, mesh-averaged experimental STM topograph has been overlaid (the square highlights the boundary of the STM image). Black and white rectangles in the images correlate inter-row voids between MOPAC simulations and STM measurements.

PO is nonpolar and nonprotic, solvophobic effects are likely to drive TMA adsorption and subsequent monolayer formation. This has previously been observed for the self-assembly of a different tricarboxylic acid from PO solutions on graphite[8] and also for other interfacial liquid−solid systems.[6] The low solubility of TMA in PO, as confirmed by UV−vis spectroscopy, is a strong indication for this hypothesis. Introducing a pristine graphite surface to the solution offers a possibility to reduce the free energy. Compared to the "inhospitable" environment in solution, adsorption of TMA on the surface decreases the systems' enthalpy by strong intermolecular binding through hydrogen bonds and adhesion to the graphite substrate. Although the zigzag dimer chain structure is not ideal as far as intermolecular hydrogen bonds are concerned—not all three carboxylic groups participate in the energetically favorable cyclic dimer motif—it might be the best compromise between adsorbing as many TMA molecules as possible on the surface while still providing reasonable intermolecular stabilization. The question why the likewise rather dense superflower structure is not observed, despite its more favorable formation of exclusively unstrained cyclic trimer motifs, can also be answered by free energy arguments. First of all, the packing density of the simulated superflower structure (1.19 molecules/nm^2) is slightly smaller than that of the zigzag dimer chain structure (1.29 molecules/nm^2). This means, for full surface coverage, more molecules are adsorbed in the zigzag dimer chain structure than in the superflower structure, which provides the strongest argument in favor of the zigzag dimer chain structure. Because the hydrogen bond density is larger in the superflower structure

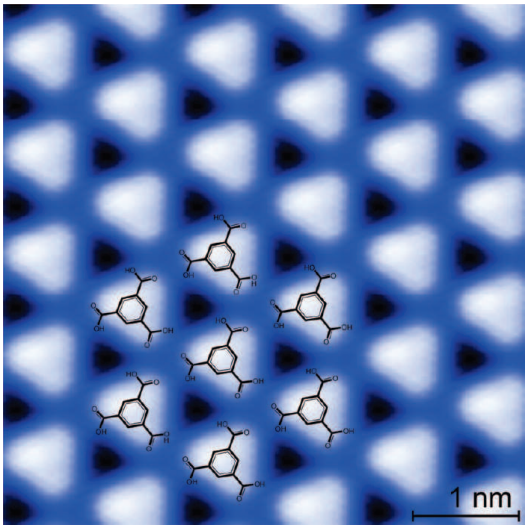

Figure 5. Simulated STM image of a hypothetical superflower structure where all TMA molecules are equivalent and each carboxylic group takes part in a cyclic trimer hydrogen-bonding arrangement. The underlying geometrical structure is obtained by MOPAC simulations. These are carried out without any constraints neither for the symmetry nor for the lattice parameter. For clearance, TMA molecules are overlaid. The structure exhibits *p*3*m*1 symmetry and a lattice parameter of 9.84 Å, which yields a packing density of 1.19 molecules/nm^2.

and the exclusive occurrence of cyclic trimers is more favorable, it is the structure with the highest binding energy per unit area when only hydrogen bonds are taken into account. Yet, the

higher packing density of the zigzag dimer chain structure also results in increased enthalpy contributions from molecule−substrate interactions. For the complete picture, entropic contributions have also to be considered for Gibbs' free energy. Upon adsorption of a monolayer, the systems' entropy is diminished because solute molecules loose translational, conformational, and rotational entropy. Again, because of its lower packing density, the superflower structure seems entropically favored, although we cannot readily evaluate the entropy of a TMA molecule in the superflower versus the zigzag chain dimer structure. To still argue on thermodynamical grounds that the zigzag dimer chain structure is thermodynamically stabilized, the additional enthalpy contribution from the increased molecule−substrate interaction—associated with the higher packing density—has to outweigh the higher entropic cost. Unfortunately, the problem is too complex and figures for the enthalpy are not robust enough for a quantitative discussion. On the other hand, self-assembly of this particular structure might also be kinetically controlled and the thermodynamic equilibrium structure might not be attained. Solvophobic effects can trap TMA molecules on the surface, although vertical mobility of adsorbed molecules is found in many liquid−solid systems. If this is the case, a transition toward a monolayer structure with lower packing density would not be possible. Compared to solvents endowed with functional groups, such as fatty acids, that can form hydrogen bonds with the solute, aprotic solvents, such as PO, exhibit weaker interaction and less stabilization of the solute. Consequently, the enthalpic gain upon adsorption of one molecule is much larger for poor solvents (PO) as compared with good solvents (fatty acids). Because the enthalpy gain per molecule is large in poor solvents, densely packed structures can become thermodynamically preferred over open-pore structures, as observed in fatty acids. We have also checked for the generality of the observed phenomenon with other nonsolvents, in this case, dodecane, which is similarly used as standard STM solvent for aliphatic solutes. Although the concentration of TMA likewise increases with sonication time, very unstable structures could only transiently be imaged with STM (Supporting Information, Figures S3−S5). This observation can be explained with the substantially lower TMA concentration in dodecane solutions as compared with PO solutions. Presumably, aromatic interactions between the PO solvent and the TMA solute are still favorable for the solubility, albeit less efficient than hydrogen bonds, as they become possible through protic solvents, such as fatty acids. In conclusion, we propose that the structure that minimizes Gibbs' free energy can depend on the solvent due to the different stabilization enthalpies of the solute molecules.

Conclusion

Upon increasing the amount of dissolved TMA in PO by sonication, we observe an unusual monolayer structure with a high packing density and atypical hydrogen-bonding pattern. The basic structural unit is a hydrogen-bonded TMA dimer. Thus, we termed the monolayer as a hydrogen-bonded zigzag dimer chain structure. Perpendicular to the dimer chains, the molecules are aligned along rows. MOPAC simulations are applied to refine the measured structure and identify possible hydrogen bonds from the minimum energy structure. Also, the MOPAC results are used for an STM image simulation that reproduces all essential experimentally observed contrast features. The existence of this so far unobserved structure with high packing density is rationalized by solvophobic effects. The solubility of TMA in nonpolar PO is low, and adsorption of molecules is a way to minimize the free energy. Still, the zigzag dimer chain is preferred over a hypothetical superflower structure with slightly lower packing density. For a full quantitative discussion of the problem, not only enthalpic gains associated with intermolecular hydrogen bonds and molecule−substrate interactions but also entropic costs have to be known precisely, which is currently beyond experimental and theoretical possibilities.

Acknowledgment. N.T.N.H. acknowledges DAAD for financial support. R.G. and M.L. acknowledge financial support by the Deutsche Forschungsgemeinschaft (SFB 486) and the Nanosystems Initiative Munich (NIM). H.T. acknowledges Centre de Calcul en Midi-Pyrénées (CALMIP) for computational resources.

Supporting Information Available: UV−vis spectra of TMA dissolved in PO, hexane, and dodecane; STM topographs of TMA self-assembled at the dodecane/graphite interface; and tentative model for the striped TMA−dodecane structure. This material is available free of charge via the Internet at http://pubs.acs.org.

References and Notes

(1) Whitesides, G. M.; Mathias, J. P.; Seto, C. T. *Science* **1991**, *254*, 1312.
(2) Prins, L. J.; Reinhoudt, D. N.; Timmerman, P. *Angew. Chem., Int. Ed.* **2001**, *40*, 2383.
(3) Barth, J. V.; Weckesser, J.; Cai, C.; Günter, P.; Bürgi, L.; Jeandupeux, O.; Kern, K. *Angew. Chem., Int. Ed.* **2000**, *39*, 1230.
(4) Feyter, S. D.; Schryver, F. C. D. *Chem. Soc. Rev.* **2003**, *32*, 139.
(5) Bleger, D.; Kreher, D.; Mathevet, F.; Attias, A. J.; Schull, G.; Huard, A.; Douillard, L.; Debuischert, C. F.; Charra, F. *Angew. Chem., Int. Ed.* **2007**, *46*, 7404.
(6) Yang, Y.; Wang, C. *Curr. Opin. Colloid Interface Sci.* **2009**, *14*, 135.
(7) Gutzler, R.; Sophie, L.; Mahata, K.; Schmittel, M.; Heckl, W. M.; Lackinger, M. *Chem. Commun.* **2009**, 680.
(8) Li, Y. B.; Ma, Z.; Qi, G. C.; Yang, Y. L.; Zeng, Q. D.; Fan, X. L.; Wang, C.; Huang, W. *J. Phys. Chem. C* **2008**, *112*, 8649.
(9) Mamdouh, W.; Uji-i, H.; Ladislaw, J. S.; Dulcey, A. E.; Percec, V.; Schryver, F. C. D.; Feyter, S. D. *J. Am. Chem. Soc.* **2006**, *128*, 317.
(10) Lackinger, M.; Griessl, S.; Heckl, W. M.; Hietschold, M.; Flynn, G. W. *Langmuir* **2005**, *21*, 4984.
(11) Griessl, S.; Lackinger, M.; Edelwirth, M.; Hietschold, M.; Heckl, W. M. *Single Mol.* **2002**, *3*, 25.
(12) Dmitriev, A.; Lin, N.; Weckesser, J.; Barth, J. V.; Kern, K. *J. Phys. Chem. B* **2002**, *106*, 6907.
(13) Payer, D.; Comisso, A.; Dmitriev, A.; Strunskus, T.; Lin, N.; Woll, C.; DeVita, A.; Barth, J. V.; Kern, K. *Chem.—Eur. J.* **2007**, *13*, 3900.
(14) Kampschulte, L.; Werblowsky, T. L.; Kishore, R. S. K.; Schmittel, M.; Heckl, W. M.; Lackinger, M. *J. Am. Chem. Soc.* **2008**, *130*, 8502.
(15) Nath, K. G.; Ivasenko, O.; Miwa, J. A.; Dang, H.; Wuest, J. D.; Nanci, A.; Perepichka, D. F.; Rosei, F. *J. Am. Chem. Soc.* **2006**, *128*, 4212.
(16) Nath, K. G.; Ivasenko, O.; MacLeod, J. M.; Miwa, J. A.; Wuest, J. D.; Nanci, A.; Perepichka, D. F.; Rosei, F. *J. Phys. Chem. C* **2007**, *111*, 16996.
(17) Ye, Y. C.; Sun, W.; Wang, Y. F.; Shao, X.; Xu, X. G.; Cheng, F.; Li, J. L.; Wu, K. *J. Phys. Chem. C* **2007**, *111*, 10138.
(18) Li, Z.; Han, B.; Wan, L. J.; Wandlowski, Th. *Langmuir* **2005**, *21*, 6915.
(19) Horcas, I.; Fernandez, R.; Gomez-Rodriguez, J. M.; Colchero, J.; Gomez-Herrero, J.; Baro, A. M. *Rev. Sci. Instrum.* **2007**, *78*, 013705.
(20) Lackinger, M.; Griessl, S.; Markert, T.; Jamitzky, F.; Heckl, W. M. *J. Phys. Chem. B* **2004**, *108*, 13652.
(21) Stewart, J. J. P. *J. Mol. Model.* **2007**, *13*, 1173.
(22) Stewart, J. J. P. *MOPAC2009*; Stewart Computational Chemistry: Colorado Springs, CO, 2008.
(23) Rezac, J.; Fanfrlik, J.; Salahub, D.; Hobza, P. *J. Chem. Theory Comput.* **2009**, *5*, 1749.
(24) Cerda, J.; Hove, M. A. V.; Sautet, P.; Salmeron, M. *Phys. Rev. B* **1997**, *56*, 15885.
(25) Ilan, B.; Florio, G. M.; Hybertsen, M. S.; Berne, B. J.; Flynn, G. W. *Nano Lett.* **2008**, *8*, 3160.
(26) Dale, S. H.; Elsegood, M. R. J.; Richards, S. J. *Chem. Commun.* **2004**, 1278.

JP907781A

The Influence of Solvophobic Effects on Self-Assembly of Trimesic Acid at the Liquid-Solid Interface

Nguyen T .N. Ha,[1,3] Thiruvancheril G. Gopakumar,[1] Rico Gutzler,[2] Markus Lackinger,[2] Hao Tang,[4] and Michael Hietschold[1]*

[1]Institute of Physics, Solid Surfaces Analysis Group, Chemnitz University of Technology, D-09107 Chemnitz, Germany.

[2]Department for Earth and Environmental Sciences and Center for NanoScience (CeNS), Ludwig-Maximilians-University, Theresienstr. 41, D-80333 Munich, Germany.

[3]Department of Applied Physics, Faculty of Physics, University of Natural Sciences, 227 Nguyen Van Cu, Ho Chi Minh City, Vietnam.

[4]Center for Material Elaboration & Structural Studies, 29, Rue Jeanne Marvig, B.P. 94347, 31055 Toulouse Cedex, France.

Supporting information

Figure S1: UV-vis spectra of TMA dissolved in PO, **Figure S2:** UV-Vis spectra of TMA dissolved in hexane, **Figure S3:** UV-Vis spectra of TMA dissolved in dodecane, **Figure S4:** STM topographs of TMA self-assembled at the dodecane/graphite interface and **Figure S5:** tentative model for the striped TMA-dodecane structure.

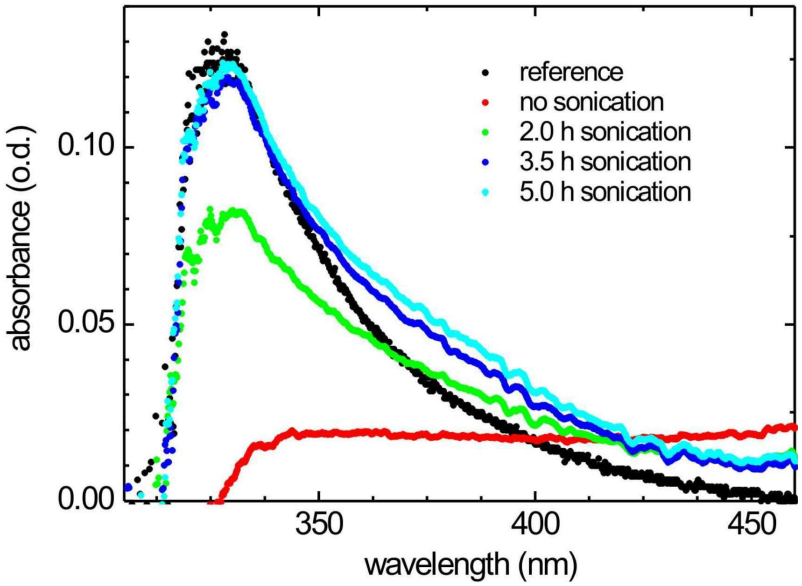

Figure S1: UV-Vis spectra of TMA dissolved in phenyloctane (PO) for different sonication durations (pure PO was used for baseline) and measured in a 10 mm quartz cuvette. Spectra were recorded for 0, 2.0, 3.5, and 5 hours of sonication. Solutions have been centrifuged after sonication for two minutes at 2000 rpm. The black spectrum corresponds to a reference solution where 0.82 mg of TMA were dissolved in 30.75 ml PO and sonicated. Since no visible sediment remained, the concentration corresponds to approximately 127 µM. This value is comparable to the concentration after 5 hours sonication time, and is also roughly one order of magnitude smaller than concentrations of TMA in previously employed fatty acid solvents. Note that in common solvents the main absorption band of TMA lies at much shorter wavelength (i.e. below λ = 300 nm, cf. Figures S2 and S3 for a reference spectrum of TMA in hexane and dodecane respectively). However, the aromatic systems of the solvent (PO) and the solute (TMA) absorb both in the near UV range. Due to this interference only the long-wavelength tail of the TMA absorption spectrum could be used to estimate the solute concentrations.

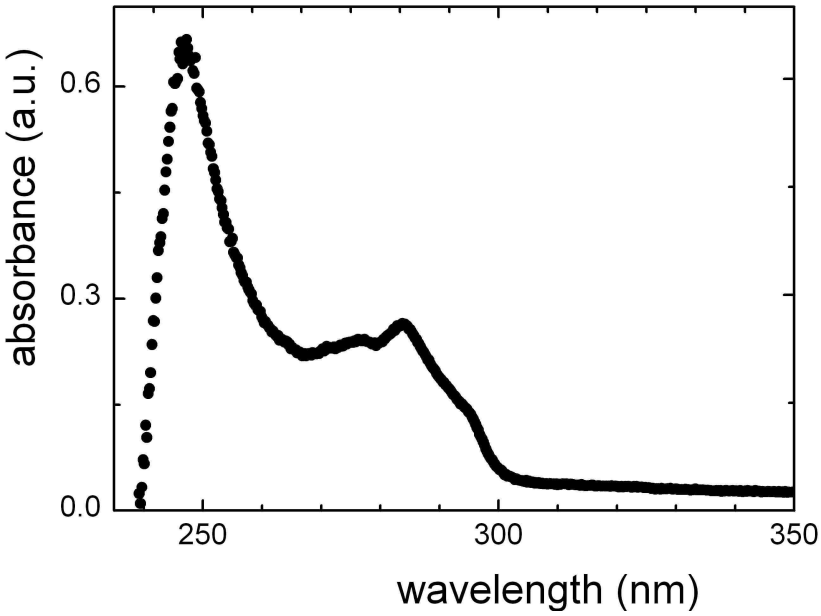

Figure S2: UV-Vis spectra of TMA dissolved in hexane (saturated solution, cuvette with 1 mm optical path length). This reference spectrum was obtained in a non-aromatic solvent in order to evaluate the actual absorption band of the aromatic TMA solute in the near UV range without any interference by solvent absorption.

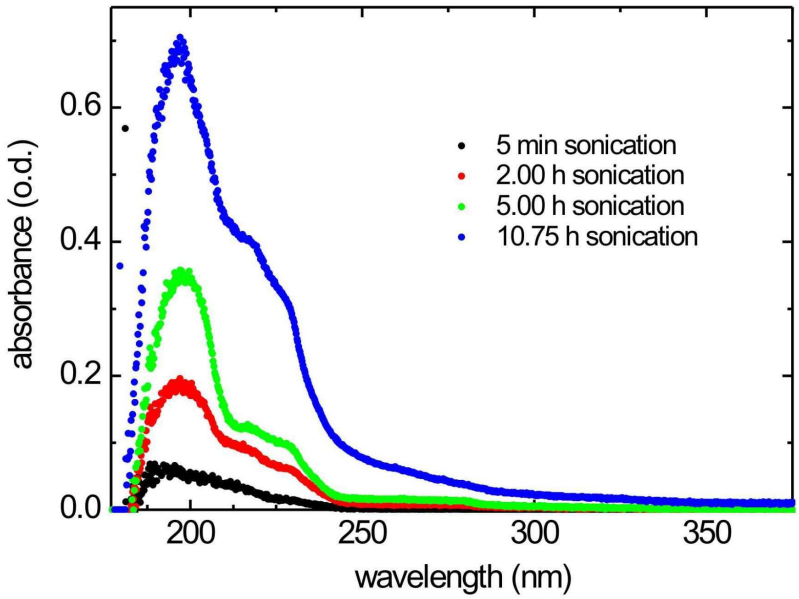

Figure S3: UV-Vis spectra of TMA dissolved in dodecane (solvent without any functional groups for strong interactions with the solute) at different sonication durations and measured in 1 mm quartz cuvette. Sonication times were five minutes, 2.0, 5.0, and 10.75 hours. Solutions have been centrifuged after sonication for two minutes at 2000 rpm. Similar to the case of TMA in PO, the TMA concentration increases with sonication time. By a comparison of the absorbance at a wavelength of ~350 nm, we conclude that the concentration of TMA in dodecane is substantially smaller than in PO. This can be attributed to the absence of any functional group in dodecane which could possibly interact with TMA, while in PO the phenyl group at least facilitates aromatic interactions between solvent and solute, thus increasing solubility.

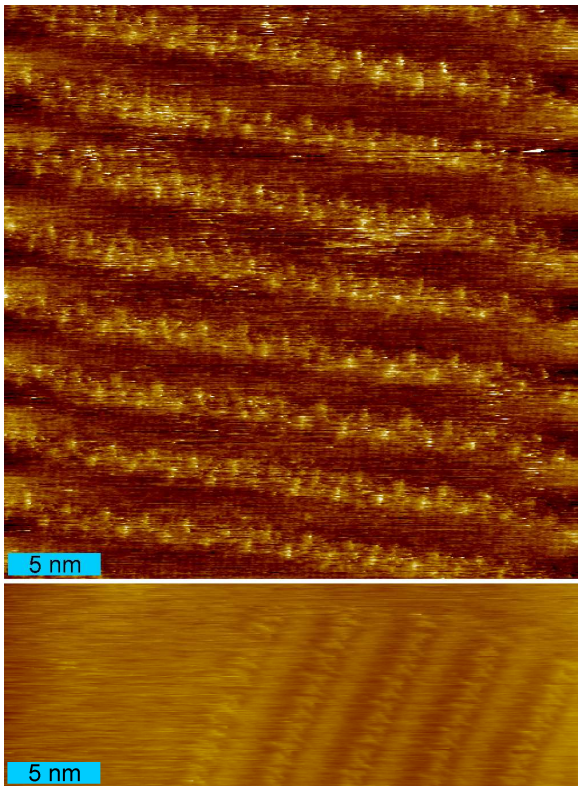

Figure S4: STM topographs of TMA self-assembled at the dodecane/graphite interface (I_T = 30 pA, V_{bias} = 1.2 V) obtained in solutions sonicated for 10.75 hours. The structures are extremely unstable and could only be transiently imaged. As shown in Fig. S5 the structure can be explained by alternating stripes of TMA and dodecane molecules.

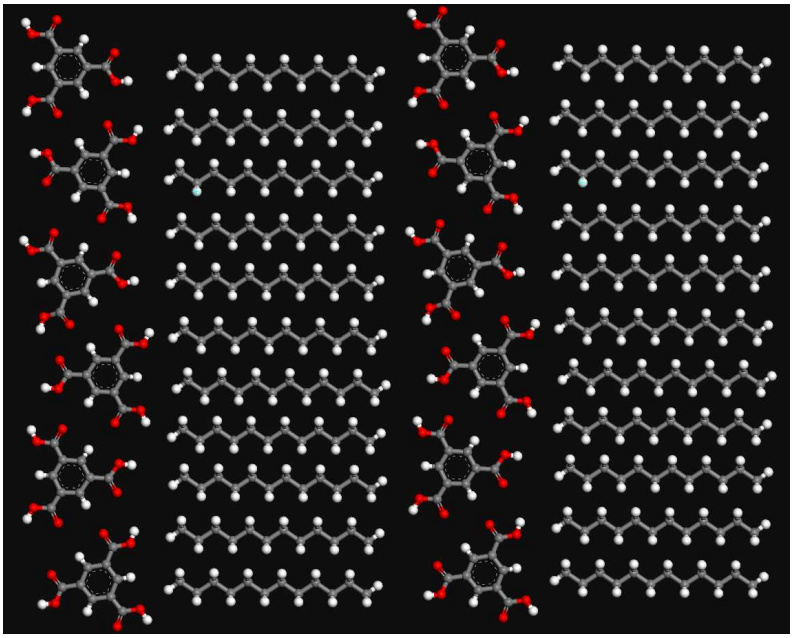

Figure S5: Tentative model for the striped TMA-dodecane structure. The structure consists of alternating TMA and dodecane stripes.

J|A|C|S
ARTICLES

Published on Web 03/17/2010

Reversible Phase Transitions in Self-Assembled Monolayers at the Liquid−Solid Interface: Temperature-Controlled Opening and Closing of Nanopores

Rico Gutzler,*,† Thomas Sirtl,† Jürgen F. Dienstmaier,† Kingsuk Mahata,‡ Wolfgang M. Heckl,# Michael Schmittel,‡ and Markus Lackinger*,†

Department of Earth and Environmental Sciences and Center for NanoScience (CeNS), Ludwig-Maximilians-University, Theresienstrasse 41, 80333 Munich, Germany, Center of Micro and Nanochemistry and Engineering, Organische Chemie I, University Siegen, Adolf-Reichwein-Strasse 2, 57068 Siegen, Germany, Deutsches Museum, Museumsinsel 1, 80538 Munich, Germany, and Department of Physics, TUM School of Education, Technical University Munich, Schellingstrasse 33, 80333 Munich, Germany

Received October 19, 2009; E-mail: rico.gutzler@lrz.uni-muenchen.de; markus@lackinger.org

Abstract: We present a variable-temperature study of monolayer self-assembly at the liquid−solid interface. By means of *in situ* scanning tunneling microscopy (STM), reversible phase transitions from a nanoporous low-temperature phase to a more densely packed high-temperature phase are observed. The occurrence of the phase transition and the respective transition temperature were found to depend on the type of solvent and solute concentration. Estimates of the entropic cost and enthalpic gain upon monolayer self-assembly suggest that coadsorption of solvent molecules within the cavities of the nanoporous structure renders this polymorph thermodynamically stable at low temperatures. At elevated temperatures, however, desorption of these relatively weakly bound solvent molecules destabilizes the nanoporous polymorph, and the densely packed polymorph becomes thermodynamically favored. Interestingly, the structural phase transition provides external control over the monolayer morphology and, for the system under discussion, results in an effective opening and closing of supramolecular nanopores in a two-dimensional molecular monolayer.

Introduction

Self-assembly of ordered monolayers at the liquid−solid interface has been proven to be well suited for functionalizing surfaces and, thus, has become a topic of elaborate research.[1−5] Especially porous networks, which can be utilized as supramolecular host systems for defined coadsorption of nanoscopic guests, have received broad interest.[6−11]Tailoring morphology, size, and functionalization of porous networks thus remains a topic of fundamental interest in nanotechnology. The monolayer morphology is primarily governed by the structure and functional groups of the molecule,[12−14] but can also depend on the type of solvent,[15−18] concentration,[5,19−21] substrate,[22] substrate-mediated interactions,[23] and other factors. Among all important parameters for self-assembly at the liquid−solid interface, temperature is probably the one least studied, and only a few examples are reported in the literature.[21,24−30] For instance, English and Hipps use STM to reveal the progressive desorption of coronene from Au(111) between room temperature and 55 °C (*in situ*, up to 105 °C *ex-situ*).[27] However, in many variable-temperature studies samples are just conditioned at elevated temperatures, while measurements are still conducted at room temperature.

Although temperature is a vital parameter for any self-assembly because it directly affects both thermodynamics and kinetics, little is known about its influence on physisorbed

† Ludwig-Maximilians-University.
‡ University Siegen.
# Deutsches Museum and Technical University Munich.

(1) Barth, J. V.; Costantini, G.; Kern, K. *Nature* **2005**, *437* (7059), 671–679.
(2) De Feyter, S.; De Schryver, F. C. *J. Phys. Chem. B* **2005**, *109* (10), 4290–4302.
(3) Elemans, J. A. A. W.; De Feyter, S. *Soft Matter* **2009**, *5* (4), 721–735.
(4) Kühnle, A. *Curr. Opin. Colloid Interface Sci.* **2009**, *14* (2), 157–168.
(5) Yang, Y. L.; Wang, C. *Curr. Opin. Colloid Interface Sci.* **2009**, *14* (2), 135–147.
(6) Kudernac, T.; Lei, S. B.; Elemans, J. A. A. W.; De Feyter, S. *Chem. Soc. Rev.* **2009**, *38* (2), 402–421.
(7) Madueno, R.; Raisanen, M. T.; Silien, C.; Buck, M. *Nature* **2008**, *454* (7204), 618–621.
(8) Theobald, J. A.; Oxtoby, N. S.; Phillips, M. A.; Champness, N. R.; Beton, P. H. *Nature* **2003**, *424* (6952), 1029–1031.
(9) Stepanow, S.; Lingenfelder, M.; Dmitriev, A.; Spillmann, H.; Delvigne, E.; Lin, N.; Deng, X. B.; Cai, C. Z.; Barth, J. V.; Kern, K. *Nat. Mater.* **2004**, *3* (4), 229–233.
(10) Griessl, S. J. H.; Lackinger, M.; Jamitzky, F.; Markert, T.; Hietschold, M.; Heckl, W. M. *Langmuir* **2004**, *20* (21), 9403–9407.
(11) Kühne, D.; Klappenberger, F.; Decker, R.; Schlickum, U.; Brune, H.; Klyatskaya, S.; Ruben, M.; Barth, J. V. *J. Am. Chem. Soc.* **2009**, *131* (11), 3881–3883.
(12) Tahara, K.; Furukawa, S.; Uji-I, H.; Uchino, T.; Ichikawa, T.; Zhang, J.; Mamdouh, W.; Sonoda, M.; De Schryver, F. C.; De Feyter, S.; Tobe, Y. *J. Am. Chem. Soc.* **2006**, *128* (51), 16613–16625.
(13) Kampschulte, L.; Werblowsky, T. L.; Kishore, R. S. K.; Schmittel, M.; Heckl, W. M.; Lackinger, M. *J. Am. Chem. Soc.* **2008**, *130* (26), 8502–8507.
(14) Gutzler, R.; Lappe, S.; Mahata, K.; Schmittel, M.; Heckl, W. M.; Lackinger, M. *Chem. Commun.* **2009**, (6), 680–682.

 10.1021/ja908919r

monolayers at the liquid−solid interface. For 1,3,5-tris(4-carboxyphenyl)benzene (BTB, cf. Figure 1a) monolayers, temperature-dependent structural phase transitions were observed under vacuum conditions on the Ag(111) surface.[31] Yet, most likely driven by a stepwise deprotonation of the carboxylic groups, these phase transitions are not reversible.

Herein we demonstrate how the morphology of BTB monolayers at the carboxylic acid/graphite interface specifically can be switched bidirectionally by lowering and raising the temperature. As detailed below, interfacial BTB monolayers show a fully reversible temperature-driven structural phase transition, changing from an open pore network to a nonporous, densely packed structure. Accordingly, nanopores can be closed at slightly elevated temperatures and opened again by cooling the sample below the transition temperature. Such a reversible process opens venues for various applications in which guest coadsorption is controlled by temperature, as a densely packed structure in contrast to an open-pore structure does not facilitate coadsorption of molecular guests.

Our experimental findings can be explained and are rationalized by thermodynamic considerations, where the free energies of adsorption of both polymorphs are evaluated from a molecule-based estimation of enthalpic gains and entropic costs.

Results and Discussion

Solvent Dependence. Three different carboxylic acids served as solvents, namely heptanoic (**7A**), octanoic (**8A**), and nonanoic acid (**9A**). At room temperature with **7A** as solvent, BTB furnishes a previously unobserved densely packed row structure on HOPG with striped appearance (Figure 1b). In **8A**, the row structure is found in coexistence with the chicken-wire structure, a hexagonal, less dense open-pore network (Figure 1c) that is quite common for other 3-fold symmetric tricarboxylic acids as well.[14,32] At room temperature, **9A** as solvent exclusively yields the chicken-wire structure (Figure 1d). Models of the respective polymorphs are presented in Figure 1e,f.

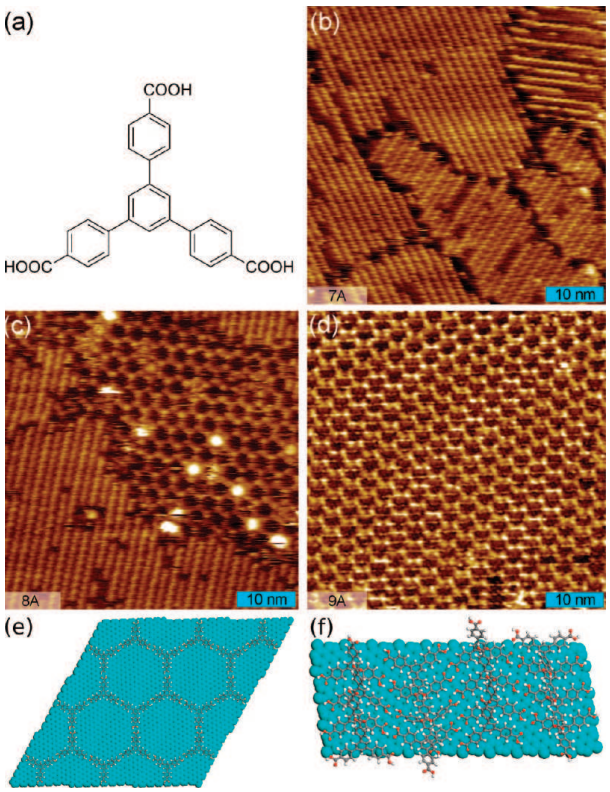

Figure 1. (a) Chemical structure of 1,3,5-tris(4-carboxyphenyl)benzene (BTB). STM topographs of BTB monolayers at the (b) heptanoic acid/graphite (V_{bias} = 0.80 V, I_T = 77 pA), (c) octanoic acid/graphite (V_{bias} = 1.10 V, I_T = 92 pA), and (d) nonanoic acid/graphite interface (V_{bias} = 1.15 V, I_T = 71 pA). In all cases saturated solutions were used and topographs were recorded at room temperature. (e) Ball-and-stick model of a chicken-wire BTB monolayer on graphite; nine unit cells are depicted (cyan: graphite substrate, gray: carbon, white: hydrogen, red: oxygen). (f) Top view of a ball-and-stick model of the row structure of BTB on graphite; eight unit cells are depicted. Adjacent rows are interconnected via hydrogen bonds.

Temperature Dependence. A home-built heatable sample stage facilitates STM measurements at the liquid−solid interface from room temperature up to ∼70 °C. Heating the BTB/**7A** system to over 60 °C did not result in any change of the monolayer morphology. At all intermediate temperatures, exclusively the row structure was observed. In **8A**, the coexistence of both phases prevailed up to ∼43 °C. Above this temperature the sample was entirely covered with the row structure. Similarly, in **9A** the chicken-wire structure was stable up to ∼55 °C, while at temperatures above only the row structure could be observed. In order to verify the reversibility of the BTB phase transition, several heat−cool cycles were conducted in **8A** and **9A**, where images were repeatedly acquired below as well as above the respective transition temperature

(15) Kampschulte, L.; Lackinger, M.; Maier, A. K.; Kishore, R. S. K.; Griessl, S.; Schmittel, M.; Heckl, W. M. *J. Phys. Chem. B* **2006**, *110* (22), 10829–10836.
(16) Mamdouh, W.; Uji-i, H.; Ladislaw, J. S.; Dulcey, A. E.; Percec, V.; De Schryver, F. C.; De Feyter, S. *J. Am. Chem. Soc.* **2006**, *128* (1), 317–325.
(17) Li, Y. B.; Ma, Z.; Qi, G. C.; Yang, Y. L.; Zeng, Q. D.; Fan, X. L.; Wang, C.; Huang, W. *J. Phys. Chem. C* **2008**, *112* (23), 8649–8653.
(18) Zhang, X.; Chen, Q.; Deng, G. J.; Fan, Q. H.; Wan, L. J. *J. Phys. Chem. C* **2009**, *113* (36), 16193–16198.
(19) Lei, S. B.; Tahara, K.; De Schryver, F. C.; Van der Auweraer, M.; Tobe, Y.; De Feyter, S. *Angew. Chem., Int. Ed.* **2008**, *47* (16), 2964–2968.
(20) So, C. R.; Tamerler, C.; Sarikaya, M. *Angew. Chem., Int. Ed.* **2009**, *48* (28), 5174–5177.
(21) Palma, C. A.; Bjork, J.; Bonini, M.; Dyer, M. S.; Llanes-Pallas, A.; Bonifazi, D.; Persson, M.; Samorì, P. *J. Am. Chem. Soc.* **2009**, *131*, 13062–13071.
(22) Klappenberger, F.; Cañas-Ventura, M. E.; Clair, S.; Pons, S.; Schlickum, U.; Qu, Z. R.; Strunskus, T.; Comisso, A.; Wöll, C.; Brune, H.; Kern, K.; De Vita, A.; Ruben, M.; Barth, J. V. *ChemPhysChem* **2008**, *9* (17), 2522–2530.
(23) Wang, Y. F.; Ge, X.; Manzano, C.; Korger, J.; Berndt, R.; Hofer, W. A.; Tang, H.; Cerda, J. *J. Am. Chem. Soc.* **2009**, *131* (30), 10400–10402.
(24) Valiokas, R.; Ostblom, M.; Svedhem, S.; Svensson, S. C. T.; Liedberg, B. *J. Phys. Chem. B* **2000**, *104* (32), 7565–7569.
(25) Azzam, W.; Bashir, A.; Terfort, A.; Strunskus, T.; Wöll, C. *Langmuir* **2006**, *22* (8), 3647–3655.
(26) Bleger, D.; Kreher, D.; Mathevet, F.; Attias, A. J.; Schull, G.; Huard, A.; Douillard, L.; Fiorini-Debuischert, C.; Charra, F. *Angew. Chem., Int. Ed.* **2007**, *46* (39), 7404–7407.
(27) English, W. A.; Hipps, K. W. *J. Phys. Chem. C* **2008**, *112* (6), 2026–2031.
(28) Kong, X. H.; Deng, K.; Yang, Y. L.; Zeng, Q. D.; Wang, C. *J. Phys. Chem. C* **2007**, *111* (26), 9235–9239.
(29) Li, C. J.; Zeng, Q. D.; Liu, Y. H.; Wan, L. J.; Wang, C.; Wang, C. R.; Bai, C. L. *ChemPhysChem* **2003**, *4* (8), 857–859.
(30) Yamada, R.; Wano, H.; Uosaki, K. *Langmuir* **2000**, *16* (13), 5523–5525.
(31) Ruben, M.; Payer, D.; Landa, A.; Comisso, A.; Gattinoni, C.; Lin, N.; Collin, J. P.; Sauvage, J. P.; De Vita, A.; Kern, K. *J. Am. Chem. Soc.* **2006**, *128* (49), 15644–15651.
(32) Lackinger, M.; Griessl, S.; Heckl, W. M.; Hietschold, M.; Flynn, G. W. *Langmuir* **2005**, *21* (11), 4984–4988.

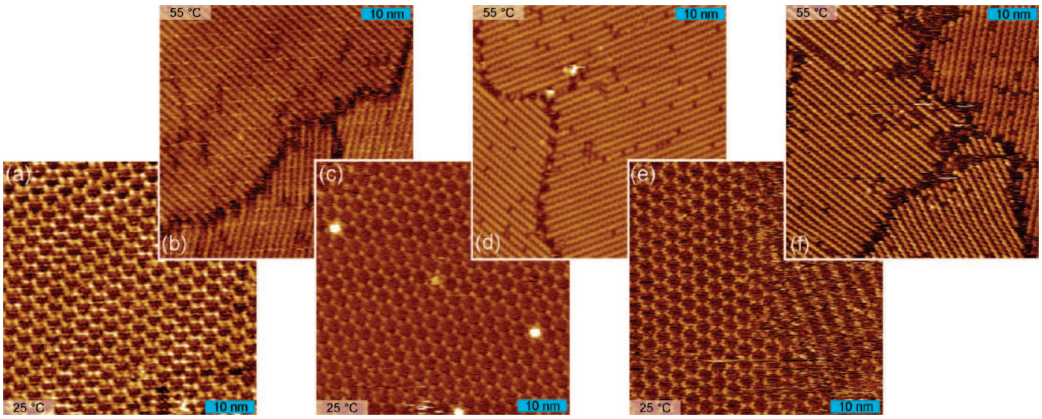

Figure 2. STM topographs as acquired during repeated heat−cool cycles of saturated BTB in nonanoic acid solutions demonstrating the reversibility of the phase transition. The respective temperature is stated in the lower (upper) left corner of each image. The cycle starts at the lower left image (a) at room temperature (V_{bias} = 1.15 V, I_T = 71 pA) and is continued (b) at 55 °C (V_{bias} = 1.15 V, I_T = 72 pA) → (c) at 25 °C (V_{bias} = 1.15 V, I_T = 65 pA) → (d) at 55 °C (V_{bias} = 1.15 V, I_T = 73 pA) → (e) at 25 °C (V_{bias} = 1.15 V, I_T = 77 pA) → (f) at 55 °C (V_{bias} = 1.15 V, I_T = 79 pA).

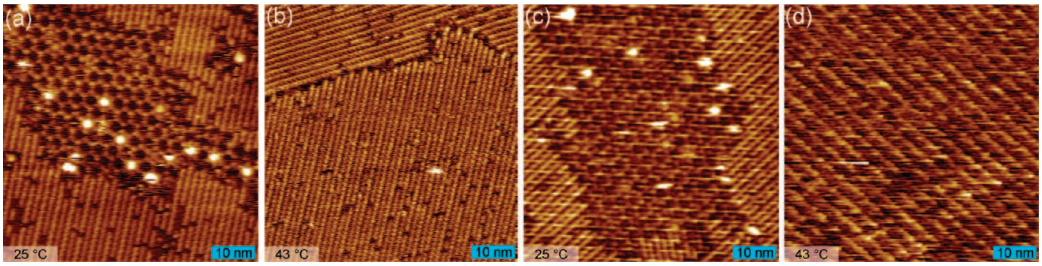

Figure 3. STM topographs as obtained from repeated heat−cool cycles of saturated BTB in octanoic acid solutions demonstrating the reversibility of the phase transition. The respective temperature is stated in the lower left corner of each image. The series starts at the left image (a) at room temperature (V_{bias} = 1.10 V, I_T = 92 pA) and is continued (b) at 43 °C (V_{bias} = 1.10 V, I_T = 78 pA) → (c) at 25 °C (V_{bias} = 1.10 V, I_T = 56 pA) → (d) at 43 °C (V_{bias} = 1.10 V, I_T = 85 pA).

(cf. Figures 2 and 3). In both solvents, the chicken-wire structure reappears below the temperature thresholds of ∼43 °C (**8A**) and ∼55 °C (**9A**), respectively. In some cases in **9A** small patches of the row structure emerged after the first cycle.

Concentration Dependence. While all studies described above were conducted with saturated solutions, further experiments were carried out with diluted solutions. Solubilities of BTB are 0.77 mM in **7A**, 0.75 mM in **8A**, and 0.50 mM in **9A**; thus all saturated solutions exhibit comparable concentrations. At BTB concentrations in **7A** of about 50% saturation, the row structure assembled on the surface coexisting with the chicken-wire structure. For more diluted solutions, at concentrations around 10% saturation, the chicken-wire structure is the dominating polymorph, emphasizing the importance of solute concentration in molecular self-assembly. Concentration-induced polymorphism, where the less densely packed polymorphs emerge for more diluted solutions, was found for various other systems.[18,19,33] As concluded from thermodynamic considerations, the observation of coexistence of both polymorphs over a wide concentration range can be taken as an indication that their free energies are very similar.[19] As a singular experiment we explored possible phase transitions in 50% saturated solution of BTB in **9A**. However, at temperatures up to ∼70 °C no phase transition was observable, therefore pointing toward a relation between concentration and transition temperature.

Discussion

With respect to the adsorption geometry of BTB molecules and adsorbate−substrate and intermolecular interactions, the row and chicken-wire polymorphs are entirely different. In the chicken-wire structure BTB molecules adsorb planar on the surface and are interconnected by linear double O−H···O hydrogen bonds between carboxylic groups, as thoroughly discussed elsewhere.[15] The hexagonal unit cell (a = 3.2 nm) contains two molecules. Likewise, the unit cell of the row structure (unit cell parameters: a = 3.3 nm, b = 0.7 nm, 82° angle) contains two molecules, but its relatively small area readily indicates nonplanar adsorption. The row structure is also comparable to the monolayer morphology found for a slightly larger tricarboxylic acid,[14] in which molecules are stacked face-to-face along columns parallel to the substrate. The monolayer is then comprised of densely packed parallel rows. In the row structure molecules adsorb nearly upright; thus the molecule−substrate interaction is diminished as compared to planar adsorption. However, intermolecular van der Waals and $\pi-\pi$ interactions stabilize the structure. BTB molecules adsorb with two carboxylic groups on the substrate, while the third carboxylic group points off the surface into the solution. According to our structural model, inter-row O−H···O hydrogen bonds are feasible, yet their unfavorable geometry and the absence of resonance effects that stabilize cyclic hydrogen bonds render

(33) Meier, C.; Roos, M.; Künzel, D.; Breitruck, A.; Hoster, H. E.; Landfester, K.; Gross, A.; Behm, R. J.; Ziener, U. *J. Phys. Chem. C* **2010**, *114* (2), 1268–1277.

Table 1. Comparison of Packing Density, Enthalpic Gain (Δh_{eff}), Entropic Cost ($-T\Delta s$), and Free Energy of Adsorption (Δg) per Unit Area of the Two Polymorphs at Two Reference Temperatures of 300 and 350 K[a]

	packing density (10^{14} cm^{-2})	Δh_{eff} (μJ cm^{-2})	$-T\Delta s$(@300 K) (μJ cm^{-2})	$-T\Delta s$(@350 K) (μJ cm^{-2})	$\Delta g = \Delta h_{eff} - T\Delta s$(@300 K) ($\mu$J cm^{-2})	$\Delta g = \Delta h_{eff} - T\Delta s$(@350 K) ($\mu$J cm^{-2})
chicken-wire (without solvent coadsorption)	0.23	−5.8	+3.9	+4.6	−1.9	−1.2
chicken-wire (with 8 × **9A** solvent molecules coadsorbed)	0.23 (BTB) 0.90 (**9A**)	−23.7	+14.6	+17.1	−9.1	−6.6
row	0.87	−18.5	+14.8	+17.3	−3.7	−1.2

[a] Stabilizing enthalpic contributions are assumed to be temperature independent. Δh_{eff} refers to values derived from molecular mechanics calculations; Δs is calculated using eqs 1 and 2.

them energetically inferior as compared to the double hydrogen bonds of the chicken-wire structure. Based on STM-derived unit cell parameters, the packing densities of the polymorphs amount to 0.23 molecules nm^{-2} for the chicken-wire and 0.87 molecules nm^{-2} for the row structure, respectively.

Thermodynamics. In the following we discuss whether the experimentally observed structure always represents the thermodynamically most stable polymorph at the respective temperature, i.e., the polymorph that yields the lowest Gibbs free energy. For monolayer self-assembly at the liquid−solid interface the whole system including the solution needs to be considered to evaluate all thermodynamic contributions. From an entropic point of view, adsorption and self-assembly of molecules from solution is unfavorable because molecules lose degrees of freedom and thus entropy upon aggregation. On the other hand, favorable enthalpic contributions arise from attractive molecule−substrate and molecule−molecule interactions. A balance of both contributions (entropy and enthalpy) steers self-assembly, and renders it a thermodynamically driven process. In order to gain insight into the thermodynamic properties of the two BTB polymorphs, the various entropic contributions were partitioned and estimated according to a method proposed by Whitesides and co-workers and similarly employed by Krissinel and Henrick.[34,35] When molecules assemble into supramolecular complexes, the entropic penalty mainly arises from losses in translational, rotational, conformational, and vibrational entropy, $\Delta S_{tot} = \Delta S_{trans} + \Delta S_{rot} + \Delta S_{conf} + \Delta S_{vib}$. Since BTB molecules do not possess significant internal degrees of freedom, conformational entropy losses can be neglected. Because of their relatively high energy in comparison to thermal energy, intramolecular vibrations do not significantly contribute to the entropy and can also be neglected.[34] The following equations provide reasonable estimates for the two relevant entropy terms for soluted molecules:

$$S_{trans} = R \ln[c^{-1}(2\pi m k_B T e^{5/3}/h^2)^{3/2}] \quad (1)$$

$$S_{rot} = R \ln[\pi^{1/2}/\gamma(8\pi^2 k_B T e/h^2)^{3/2}(I_1 I_2 I_3)^{1/2}] \quad (2)$$

Here, h is Planck's constant, k_B the Boltzmann constant, R the gas constant, and T the absolute Temperature, while e is Euler's number, m is the solute's mass, and c is the solute concentration. Furthermore, γ considers the symmetry of the molecule, and I_1, I_2, and I_3 are its principle moments of inertia. In order to avoid overestimation of translational entropy, concentrations are related to the free volume of the solvent as proposed by Whitesides and co-workers. The free volume of a solvent can be estimated by the hard cube approximation[34] and is significantly smaller than the actual volume, e.g., ∼32 mL for 1 L of heptanoic acid. It is assumed that upon adsorption molecules entirely lose their translational and rotational entropy, consequently eqs 1 and 2 allow estimating the entropic loss for adsorption of a single BTB molecule from solution. In the same manner, the entropic losses for coadsorbed solvent molecules can be estimated.

In order to compare the entropic costs for the two polymorphs, contributions from rotational and translational entropy were calculated assuming saturated solutions. For all three solvents, the entropic cost for BTB adsorption has a similar value of −0.190 kJ mol^{-1} K^{-1} for translational and −0.152 kJ mol^{-1} K^{-1} for rotational entropy. In order to estimate the entropic cost per unit area for self-assembly of a pure monolayer of the respective polymorph, the total entropy loss of −0.342 kJ mol^{-1} K^{-1} was then combined with STM-derived molecular packing densities. Numbers for the entropic contribution to the free energy at 300 K (room temperature) and 350 K respectively are provided in Table 1. It can be clearly seen that the row structure is entropically far less favorable than the chicken-wire structure, due to its 3.8-fold higher packing density. The entropic cost becomes even more pronounced at elevated temperatures. However, the situation is altered when solvent coadsorption within the cavities of the chicken-wire structure is taken into account. Although coadsorbed solvent molecules have not been directly observed in this study, probably due to their low stabilization energy and short residence times, coadsorption of guest molecules within open-pore networks was observed experimentally[14,16,18,21] and has been recognized as an important stabilizing contribution.[12,13,19,33,36] For instance, coadsorption of coronene as molecular guest in the cavities of an open-pore dehydrobenzoannulene polymorph stabilizes this host−guest network thermodynamically in comparison to the densely packed polymorph.[36]

In the present case, up to eight solvent molecules (**8A** or **9A**) can be coadsorbed in each cavity of the chicken-wire structure

(34) Mammen, M.; Shakhnovich, E. I.; Deutch, J. M.; Whitesides, G. M. *J. Org. Chem.* **1998**, *63* (12), 3821–3830.
(35) Krissinel, E.; Henrick, K. *J. Mol. Biol.* **2007**, *372* (3), 774–797.
(36) Furukawa, S.; Tahara, K.; De Schryver, F. C.; Van der Auweraer, M.; Tobe, Y.; De Feyter, S. *Angew. Chem., Int. Ed.* **2007**, *46* (16), 2831–2834.

(cf. Supporting Information Figure S4). Coadsorbed **9A** solvent molecules cause a translational entropy loss of -0.102 kJ mol^{-1} K^{-1} and a rotational entropy loss of -0.132 kJ mol^{-1} K^{-1}. Comparison of these values with the entropic losses for BTB adsorption points out that the total entropic cost increases more steeply with the number of adsorbed molecules rather than with the size and molecular weight of adsorbates. Since solvent coadsorption drastically increases the number of adsorbed molecules, the associated entropic cost of the chicken-wire structure becomes significantly enhanced. The relatively large entropic contributions to Gibbs free energy of both solute and solvent molecules (cf. Table 1) underline the fact that entropy considerations have to be taken into account for thermodynamics of monolayer self-assembly.

A quantitative comparison of the stabilizing enthalpic contributions between the two polymorphs is more difficult because different types of interactions (i.e., hydrogen bonds vs van der Waals and $\pi-\pi$ interactions) need to be compared. Molecular mechanics (MM) simulations are well suited to evaluate the energetics of van der Waals interactions. However, standard force fields seriously underestimate the strength of cyclic resonance stabilized hydrogen bonds.[37] In order to make a valid comparison of binding enthalpies, MM results using the Dreiding force field for the chicken-wire polymorph are combined with the experimentally and theoretically well-established binding enthalpy of -60 kJ mol^{-1} for the 2-fold O$-$H$\cdots$O hydrogen bond between two carboxylic groups.[38]

According to the proposed method, the average binding enthalpy of BTB molecules in the chicken-wire structure amounts to -332 kJ mol^{-1}. This value originates from the combination of a MM-derived molecule$-$substrate interaction of -242 kJ mol^{-1} with the binding enthalpy due to intermolecular hydrogen bonds of -90 kJ mol^{-1} $= 3 \times 0.5 \times -60$ kJ mol^{-1}. In the chicken-wire structure all three carboxylic groups of each molecule form 2-fold intermolecular hydrogen bonds, while the factor 0.5 corrects for overcounting of pairwise interactions.

The row structure is predominantly stabilized by van der Waals interactions, and the average binding enthalpy was evaluated by MM computations, which yield a value of -308 kJ mol^{-1} (cf. Supporting Information for details). As anticipated, the adsorbate$-$substrate binding is inferior in the row structure (-176 kJ mol^{-1}), but due to the high packing density and mutual molecular arrangement the intermolecular van der Waals and $\pi-\pi$ interactions are superior.

Last, the stabilizing effect of coadsorbed solvent molecules within the cavities of the chicken-wire structure is calculated. Coadsorption of eight **9A** solvent molecules in one cavity of the chicken-wire structure yields an enthalpic contribution of -940 kJ mol^{-1} per unit cell (cf. Supporting Information for a structural model and details of the calculation).

Binding enthalpies obtained from the above methods refer to isolated, geometry-optimized molecules under vacuum. Yet, the appropriate reference state for these considerations is dissolved and solvated solute molecules.[39] Solvation enthalpies lower the effective binding enthalpies significantly. In comparison to experiments under ultra-high-vacuum conditions, desorption barriers are substantially lower at the solid$-$liquid interface, which gives rise to an effective adsorption$-$desorption equilibrium even for comparatively large compounds.[13,18,36] Corrections of the adsorption enthalpy due to solvation were included by assuming that the interaction of dissolved solute molecules in solution is governed by intermolecular solvent$-$solute or solute$-$solute hydrogen bonds, where each of the three carboxylic groups of BTB forms a 2-fold hydrogen bond with a binding enthalpy of -60 kJ mol^{-1}. Consequently, solvation lowers the effective binding enthalpy of each molecule by at least $+180$ kJ mol^{-1}.

On the basis of the estimates of both entropic cost and enthalpic gain, the free energies of adsorption of each polymorph were evaluated for two reference temperatures. Since in all experiments the surface coverage is close to unity, we will refer to Gibbs free energy of adsorption per unit area A: $\Delta g = \Delta G/A = \Delta H/A - T\Delta S/A = \Delta h - T\Delta s$ (note that Δh and Δs, i.e., enthalpy and entropy changes per unit area upon monolayer self-assembly, are both negative). The results are summarized in Table 1. For the chicken-wire polymorph two scenarios were considered, with and without coadsorption of solvent (**9A**).

For room temperature the figures in Table 1 indicate that the row structure is thermodynamically favored over the pure chicken-wire polymorph, i.e., when solvent coadsorption is neglected. However, despite its large entropic cost, solvent coadsorption still stabilizes the chicken-wire polymorph at room temperature and even renders this bimolecular monolayer the thermodynamically most stable polymorph in **9A**. At elevated temperature, the free energy gain associated with self-assembly of a monolayer row structure becomes comparable to the chicken-wire structure without coadsorbed solvent due to the increased entropic cost of the more densely packed polymorph. On the basis of these estimates of Δg, the following explanation for the reversible phase transition is proposed: With the aid of solvent coadsorption, the chicken-wire polymorph is the thermodynamically most stable polymorph at room temperature in **9A**. Upon increasing the temperature, coadsorbed solvent molecules start to desorb first, while the chicken-wire network is still stable. Coadsorbed solvent molecules are less tightly bound than BTB molecules, as the latter—due to their size—have increased interaction with the substrate and are additionally stabilized by six hydrogen bonds. Once the chicken-wire structure lacks the stabilizing contribution from solvent coadsorption, the free energy of adsorption of the row structure becomes comparable, giving rise to the phase transition. The proposed model also consistently explains the solvent dependence of the transition temperature. The binding enthalpies of fatty acid molecules on graphite increase approximately linearly with their aliphatic chain length. Accordingly, the desorption temperature of **8A** solvent molecules is lower than that of **9A** molecules. In the thermodynamic competition between chicken-wire and row structure, easier desorption leads to a lower transition temperature in **8A** than in **9A** solutions or a transition temperature even below room temperature as observed for **7A**.

Although in the present case a molecule-based evaluation of thermodynamic quantities yields the correct trends, a word of caution is appropriate. The Gibbs free energies of adsorption and the relative thermodynamical stabilities of these polymorphs sensitively depend on the subtle balance of adsorbate$-$adsorbate, adsorbate$-$substrate, and solute$-$solvent interactions. A quantitative thermodynamic discussion of the complex situation of monolayer self-assembly at the liquid$-$solid interface is challenging primarily because of inaccuracies in the evaluation of

(37) Martsinovich, N.; Troisi, A. *J. Phys. Chem. C* **2010**, *114* (10), 4376–4388.
(38) Neuheuser, T.; Hess, B. A.; Reutel, C.; Weber, E. *J. Phys. Chem.* **1994**, *98* (26), 6459–6467.
(39) Meier, C.; Landfester, K.; Künzel, D.; Markert, T.; Gross, A.; Ziener, U. *Angew. Chem., Int. Ed.* **2008**, *47* (20), 3821–3825.

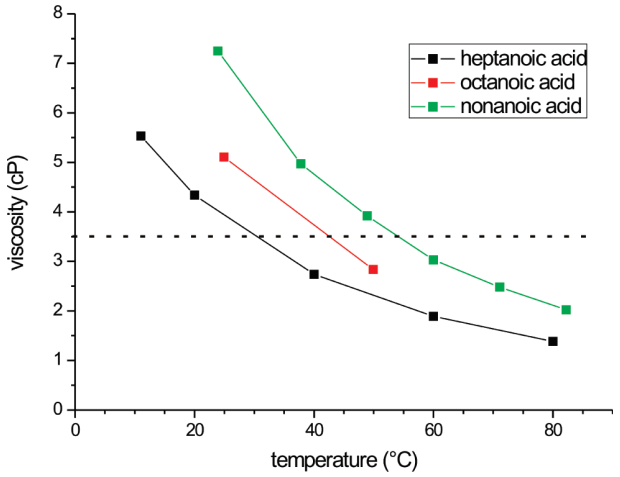

Figure 4. Viscosities of pure heptanoic (**7A**), octanoic (**8A**), and nonanoic acid (**9A**) as a function of temperature,[41] depicting the inverse dependence of viscosity on temperature. The dashed line indicates a value of 3.5 cP.

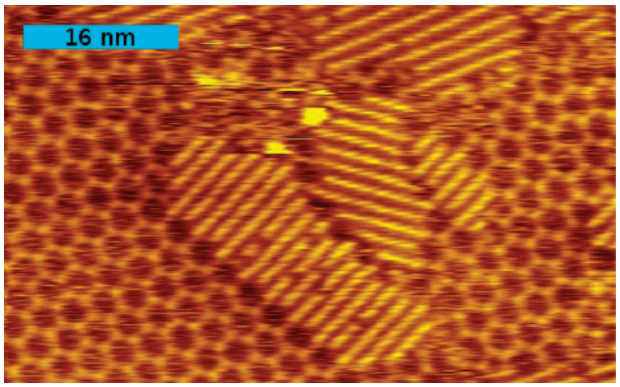

Figure 5. STM topograph of a BTB monolayer in nonanoic acid (**9A**) after heating and cooling. Patches of the row structure are observable and coexist with the chicken-wire structure. The lower left phase boundary exemplifies a general observation: the rows are aligned with the chicken-wire structure. Every other row is connected to molecules from the chicken-wire polymorph; rows in between end in cavities.

both entropic and enthalpic contributions, but also due to hardly assessable contributions, as for instance from solvation. Also, for solvent coadsorption precise structural data are not available.

Nevertheless, established methods to estimate entropic costs and evaluation of binding energies based on molecular mechanics and experimental values for hydrogen bond energies allow at least a semiquantitative evaluation of Gibbs free energies of adsorption of competing monolayer polymorphs. Although the exact prediction of crossing points as a function of concentration or temperature is hardly possible, at least a qualitative understanding of trends can be obtained. On the other hand, kinetic effects might also play an important role for monolayer self-assembly. From basic considerations, we conclude that the adsorption rate of solute molecules is proportional to c/η, where c stands for the solute concentration and η for the solvent viscosity (cf. Supporting Information). Interestingly, the viscosities of all three solvents in this study are considerably different at room temperature and crucially depend on temperature as depicted in Figure 4. Also, the viscosities of **7A**, **8A**, and **9A**, and thus the adsorption rate, correlate inversely with temperature and vary appreciably within the relevant temperature interval.

Further interesting aspects are topological and epitaxial similarities between chicken-wire and row structure: As illustrated in Figure 5, STM topographs of both coexisting polymorphs clearly show a structurally well-defined heterointerface. Moreover, the direction of the rows is aligned with the cavities of the chicken-wire polymorph. Both facts indicate that a morphological transition from chicken-wire to row polymorph might be initiated by filling of empty cavities of the chicken-wire structure with excess BTB molecules. Under conditions where the row structure becomes thermodynamically favored, this phase transition can also be understood as a cross nucleation event, i.e., a special case of heterogeneous nucleation where a thermodynamically more stable polymorph nucleates on a preexistent metastable modification.[40]

De Feyter et al. discussed and modeled the concentration dependence of bimorphic monolayer self-assembly in detail.[19] Similarly, by means of a slightly different model, Meier et al. conclude that densely packed polymorphs become thermodynamically preferred at higher solute concentrations.[33] In both cases, at low concentrations, an open-pore structure is favored over a densely packed structure, just as in the present case for BTB in **7A**. The thermodynamic model proposed by de Feyter et al. also includes a temperature-dependent term, which results in a diminished coverage ratio of open-pore to densely packed polymorph at elevated temperatures. Consequently, their model seems generally applicable and can also explain the temperature-dependent phase transition, provided that the chemical potential of BTB molecules in the row structure is sufficiently large.

Conclusions and Outlook

By means of STM reversible temperature-driven phase transitions have been observed for BTB monolayers at the liquid−solid interface. Carboxylic acids were used as solvents, and transition temperatures were found to depend on type of solvent and concentration. The two polymorphs differ significantly in packing density, arrangement of molecules, and intermolecular interactions. Both morphologies are known, and analogues have previously been reported for other tricarboxylic acids.[14,15] Estimates of the entropic cost and enthalpic gain upon monolayer self-assembly of both polymorphs suggest that a thermodynamic explanation for the phase transition in view of Gibbs free energy of adsorption is only appropriate when solvent coadsorption is taken into account. Solvent coadsorption within the cavity voids of the nanoporous chicken-wire structure has a high entropic cost because the number of adsorbed molecules is large. However, this entropic cost is still outweighed by the associated enthalpic gain. In order to explain the phase transition, we propose that desorption of coadsorbed solvent molecules

(40) Yu, L. *CrystEngComm* **2007**, *9* (10), 847–851.

(41) Landolt-Börnstein *Tabellenwerk Zahlenwerte und Funktionen aus Physik, Chemie, Astronomie, Geophysik und Technik*; Springer: Berlin, **2002**; Vol. 18 B.

eventually destabilizes the chicken-wire polymorph and leads to the emergence of the row structure. This purely thermodynamic model inherently explains the reversibility of the phase transition. However, the kinetics of adsorption and desorption can also determine the experimental observations. For instance, the row structure patches that were occasionally observed in **9A** after the first heat−cool cycle might be attributed to a slow desorption kinetics of BTB molecules in the row structure. Mostly because of the strong temperature dependence of solvent viscosity, also the adsorption kinetics changes significantly with temperature.

There is one particularly intriguing aspect to the phase transition from chicken-wire to row structure: it closes supramolecular cavities. This effect may be utilized for the controlled release of molecular guests with conceivable medical and life-science applications. With this in mind, it would be highly interesting to explore whether adsorption of deliberate molecular guests other than coadsorbed solvent molecules within the pores of the chicken-wire structure hampers the phase transition, thus leading to increased transition temperatures or even suppression of the phase transition.

Acknowledgment. Financial support by the Deutsche Forschungsgemeinschaft (Sonderforschungsbereich 486, FOR 516), the Bayerische Forschungsstiftung, and the Nanosystems Initiative Munich (NIM) is gratefully acknowledged.

Supporting Information Available: Experimental details, kinetic considerations, additional STM topographs, and details of molecular mechanics simulations. This material is available free of charge via the Internet at http://pubs.acs.org.

JA908919R

Supporting Information

Reversible phase transitions in monolayer self-assembly at the liquid-solid interface – temperature controlled opening and closing of nanopores

Rico Gutzler[*†], Thomas Sirtl[†], Jürgen F. Dienstmaier[†], Kingsuk Mahata[‡], Wolfgang M. Heckl[#], Michael Schmittel[‡], and Markus Lackinger*[*†]*

[†] Department of Earth and Environmental Sciences and Center for NanoScience (CeNS), Ludwig-Maximilians-University, Theresienstrasse 41, 80333 Munich, Germany; [‡] Center of Micro and Nanochemistry and Engineering, Organische Chemie I, University Siegen, Adolf-Reichwein-Strasse 2, 57068 Siegen, Germany; [#] Deutsches Museum, Museumsinsel 1, 80538 Munich and Department of Physics, TUM School of Education, Technical University Munich, Schellingstrasse 33, 80333 Munich, Germany

1. Experimental details

All solvents were used as received from Sigma Aldrich and 1,3,5-tris(4-carboxyphenyl)benzene was synthesized according to literature-known procedures.[1] Solutions were prepared by dissolving BTB until saturation in the respective carboxylic acid. Subsequently, solutions were centrifuged in order to avoid supersaturation effects. Droplets of ~2.5 µL saturated solution were applied onto the basal plane of freshly cleaved highly oriented pyrolytic graphite (HOPG). STM experiments were carried out with a home-built STM driven by RHK control electronics. The STM tip was immersed into solution during image acquisition. All images were recorded in constant current mode and were processed by line wise levelling only, except for some topographs recorded in 8A where a Gaussian filter was applied. For details on the heatable sample stage and STM measurements at elevated temperature cf. Walch et al.[2]

BTB solubilities in all solvents were determined by UV-Vis absorption spectroscopy conducted with a USB4000 UV-Vis spectrometer from Ocean Optics.

2. Kinetic considerations

Two main kinetic factors influence monolayer formation on surfaces: the adsorption rate of molecules on the surface, the flux F, and transport of adsorbates across the surface, i.e. surface diffusion as described by the diffusivity D. When the ratio of surface diffusion to adsorption rate F/D is small, the resulting surface structure represents the thermodynamic equilibrium. On the other hand, when the ratio F/D becomes large, kinetic effects become increasingly important.

According to Fick's laws of diffusion, the flux F of dissolved molecules impinging on a surface is given by:

$$F = - d\,(\partial c / \partial z), \tag{1}$$

where d is the bulk diffusivity in solution (not to be confused with the surface diffusivity D), c the concentration in solution and z the spatial coordinate perpendicular to the surface. The chemical potential μ of an ideal solution as a function of temperature T and concentration c is given by:

$$\mu = \mu_0 + RT \ln c \tag{2}$$

with R being the gas constant and μ_0 the chemical potential under standard conditions. Accordingly equation (1) can be rewritten as:

$$F = - dc / RT\,(\partial \mu / \partial z). \tag{3}$$

The flux F of molecules impinging on the surface is thus driven by a gradient in the chemical potential perpendicular to the surface. This gradient is build up by a difference between chemical potential on the surface with respect to the bulk (solution) and is non-zero until the monolayer growth has been completed. In thermodynamical equilibrium, when the gradient is zero, the net flux F likewise becomes equal to zero. As a coarse approximation, the bulk diffusivity d, i.e. the mobility of solute molecules in solution, can be approximated by the Stokes-Einstein equation:

$$d = k_B T / 6\pi r \eta(T). \tag{4}$$

Consequently, the flux becomes:

$$F \propto - \, c \, / \, \eta(T) \, (\partial\mu \, / \, \partial z). \qquad (5)$$

In equations (4) and (5), r is the radius of a spherical particle and $\eta(T)$ the solvent viscosity, which in the case of fatty acids strongly depends on temperature in the range 25 °C to 50 °C. From equation (5), the ratio solute concentration to solvent viscosity c/η is identified as the critical parameter for the flux F.

3. Additional STM Topographs

Concentration dependence (heptanoic acid):

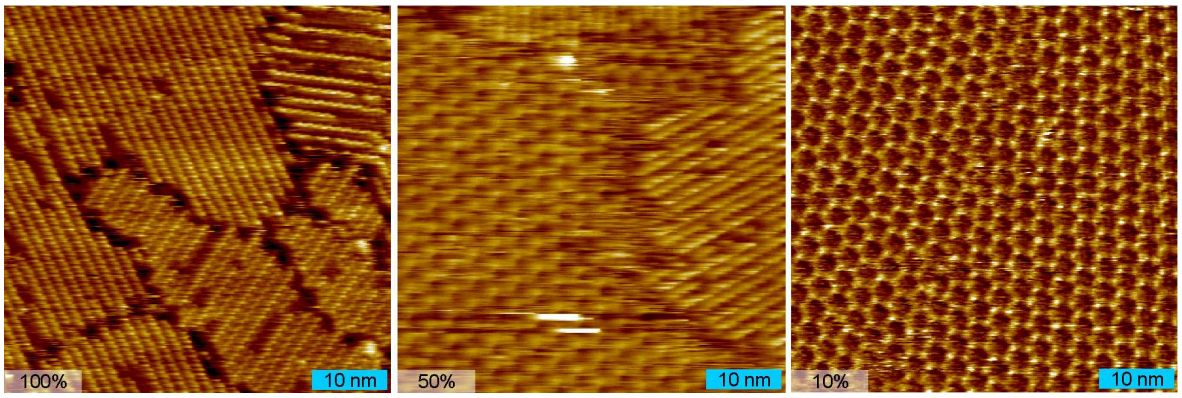

Fig. S1. Left: Saturated solution of BTB in heptanoic acid (V_{bias} = 0.80 V, I_T = 77 pA). Exclusively the row structure is observed. Center: 50% saturated solution (V_{bias} = 0.84 V, I_T = 90 pA).; row and chickenwire structure coexist. Right: 10% saturated solution (V_{bias} = 0.96 V, I_T = 73 pA); almost solely the chickenwire structure is formed.

Intermediate temperatures (nonanoic acid)

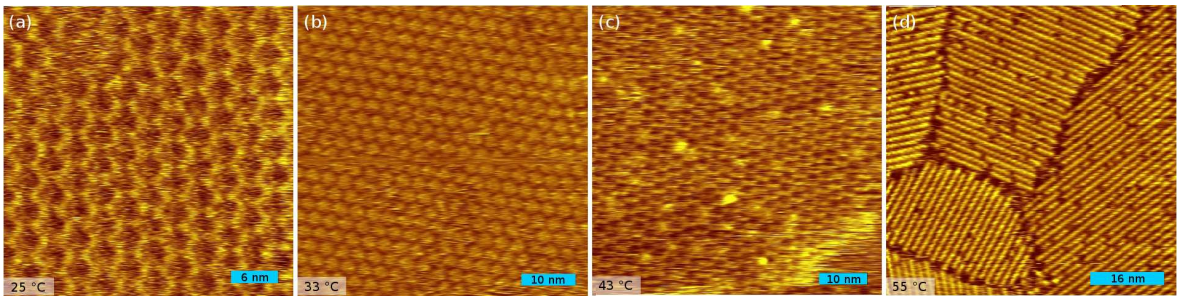

Fig. S2: STM topographs of BTB in nonanoic acid for intermediate temperatures: (a) at room temperature (V_{bias} = 1.05 V, I_T = 90 pA), (b) at ~33 °C (V_{bias} = 1.05 V, I_T = 57 pA), (c) at ~43 °C (V_{bias} = 1.05 V, I_T = 95 pA), and (d) at ~55 °C (V_{bias} = 1.04 V, I_T = 69 pA). At temperatures below the transition temperature only the chickenwire polymorph can be observed.

4. Details on molecular mechanics + additional results

Molecular mechanics based on the Dreiding force field as implemented in the Cerius[2] (Version 4.5, MSI) software package was utilized for a structural refinement and estimation of binding energies. Periodic boundary conditions were employed with the experimental unit cells as constraints. The graphite substrate was approximated by two layers and atomic positions in the second layer were fixed. Values for the unit cell parameters were deduced from split images,[3] where one part of the image depicts the adsorbate layer and in the other part the graphite substrate was atomically resolved. Molecules were arranged on the surface without further constraints. An energy difference of < 0.001 kcal/mol and a force difference < 0.5 kcal/mol/Å between single steps served as convergence criteria. For the hexagonal structure, nine unit cells were used as the basic building unit (cell parameters in matrix notation referring to the graphite lattice vectors: U = (21 45 0) V = (45 24 0)). The basic unit for the row structure consisted of eight unit cells (U = (4 12 0) V = (30 10 0)). Binding energies were calculated by extracting one molecule from the optimized structure and performing a single point energy calculation.

The average binding enthalpy $\Delta H_{BTB\text{-}row}$ of a single BTB molecule in the row structure was evaluated in the following way:

(1) Evaluate energy ΔE_{total} to remove a single BTB molecule from the row structure:

- optimize complete structure (including all BTB molecules on the surface) → E_1
- delete one molecule from the structure and calculate energy (without further geometry optimization) → E_2
- calculate energy of a single geometry optimized BTB molecule → E_3
- $\Delta E_{total} = E_1 - E_2 - E_3$

(2) Evaluate binding energy of a single BTB molecule in the row structure

to graphite $\Delta E_{mol\text{-}sub}$:

- optimize complete row structure (including all BTB molecules on the surface)
- delete all molecules from the structure except one and calculate energy (no geometry optimization in between) → E_1
- calculate energy of pristine graphite, i.e. without BTB molecules adsorbed → E_2
- calculate energy of a single geometry optimized BTB molecule → E_3
- $\Delta E_{mol\text{-}sub} = E_1 - E_2 - E_3$

(3) Average binding enthalpy $\Delta H_{BTB\text{-}row}$ of BTB molecules in the row structure:

- evaluate average intermolecular binding energy $\Delta E_{mol\text{-}mol}$:

$\Delta E_{mol\text{-}mol} = (\Delta E_{total} - \Delta E_{mol\text{-}sub}) / 2$

since pairwise interactions are equally shared by two bonding partners, only 50% count for the average intermolecular binding energy per molecule

- $\Delta H_{BTB\text{-}row} = \Delta E_{mol\text{-}mol} + \Delta E_{mol\text{-}sub}$

Binding enthalpy ΔH_{solv} of coadsorbed solvent molecules ΔH_{coads}:

- optimize full BTB network with one cavity filled with eight 9A molecules → E_1
- calculate energy of empty, geometry optimized BTB network → E_2
- calculate energy of one single optimized 9A molecule → E_3
- $\Delta H_{solv} = E_1 - E_2 - 8 \times E_3$

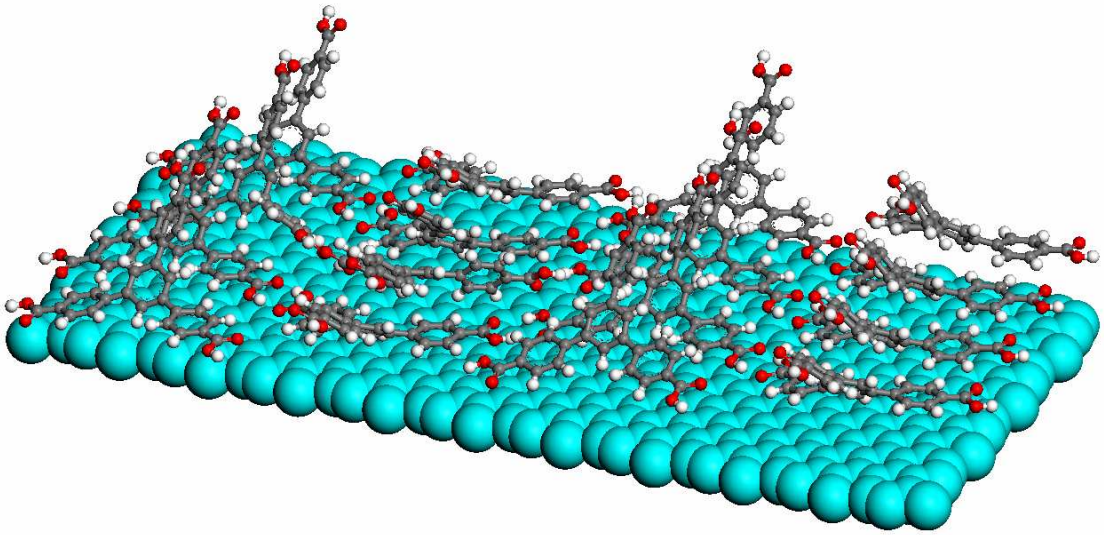

Fig. S3: Inclined view of a ball-and-stick model of the row structure, eight unit cells are depicted. Adjacent rows are tilted in opposite directions. (cyan: graphite substrate, grey: carbon, white: hydrogen, red: oxygen)

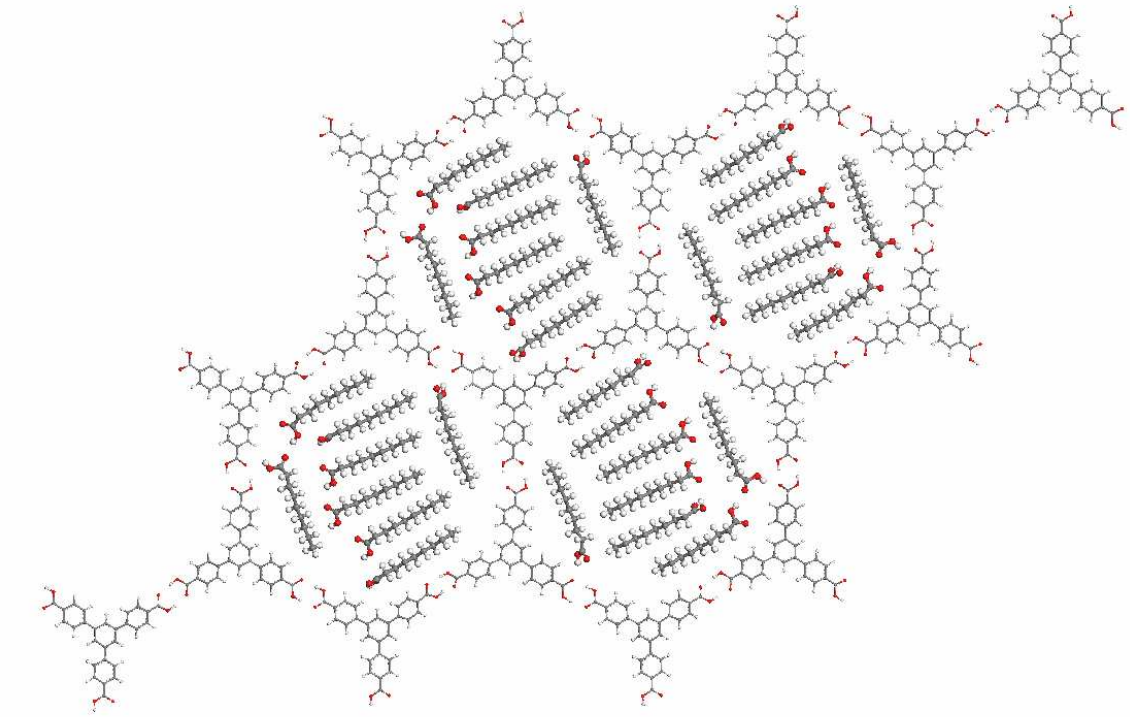

Fig. S4: Ball-and-stick model of the chickenwire structure with coadsorbed nonanoic acid molecules. 8 solvent molecules fit within one cavity;

5. References

1. Weber, E.; Hecker, M.; Koepp, E.; Orlia, W.; Czugler, M.; Csoregh, I., *J. Chem. Soc., Perkin Trans. 2* **1988,** (7), 1251-1257.

2. Walch, H.; Maier, A. K.; Heckl, W. M.; Lackinger, M., *J. Phys. Chem. C* **2009,** 113 (3), 1014-1019.

3. Lackinger, M.; Heckl, W. M., *Langmuir* **2009,** 25 (19), 11307-11321.

Material- and Orientation-Dependent Reactivity for Heterogeneously Catalyzed Carbon−Bromine Bond Homolysis

Hermann Walch,*,† Rico Gutzler,† Thomas Sirtl,† Georg Eder,† and Markus Lackinger*,†,‡

Department for Earth and Environmental Sciences and Center for NanoScience (CeNS), Ludwig-Maximilians-University, Theresienstrasse 41, 80333 Munich, Germany, and Deutsches Museum, Museumsinsel 1, 80538 Munich, Germany

Received: March 25, 2010; Revised Manuscript Received: June 18, 2010

Adsorption of the brominated aromatic molecule 1,3,5-tris(4-bromophenyl)benzene on different metallic substrates, namely Cu(111), Ag(111), and Ag(110), has been studied by variable-temperature scanning tunneling microscopy (STM). Depending on substrate temperature, material, and crystallographic orientation, a surface-catalyzed dehalogenation reaction is observed. Deposition onto the catalytically more active substrates Cu(111) and Ag(110) held at room temperature leads to cleavage of carbon−bromine bonds and subsequent formation of protopolymers, i.e., radical metal coordination complexes and networks. However, upon deposition on Ag(111) no such reaction has been observed. Instead, various self-assembled ordered structures emerged, all based on intact molecules. Also sublimation onto either substrate held at ∼80 K did not result in any dehalogenation, thereby exemplifying the necessity of thermal activation. The observed differences in catalytic activity are explained by a combination of electronic and geometric effects. A mechanism is proposed, where initial charge transfer from substrate to adsorbate, followed by subsequent intramolecular charge transfer, facilitates C−Br bond homolysis.

Introduction

Heterogeneous catalysis provides the basis for the economic synthesis of the majority of compounds produced worldwide and is thus of utmost importance for the chemical industry. In relation to its importance, however, the atomistic understanding of the underlying processes lags behind. The "surface science approach", which was introduced by Ertl, i.e., the use of atomically flat and clean single crystal surfaces under ultrahigh vacuum (UHV) conditions as model catalysts,[1,2] has stimulated a lot of effort in this field. Among other techniques, scanning tunneling microscopy (STM) has been taking a major role as a tool to reveal catalytic phenomena by high-resolution real space imaging,[3–6] in particular for the dissociative adsorption of molecules.[7,8]

Here we report on the heterogeneously catalyzed dehalogenation of the comparatively large aromatic compound 1,3,5-tris(4-bromophenyl)benzene (TBB, cf. Fig. 1 for structure) on coinage metal surfaces. TBB is also a well-suited candidate monomer for the synthesis of surface supported two-dimensional polymers. For the synthesis of two-dimensional polymers, different strategies are proposed to cleave the C−Br σ-bonds, an activation step which creates free radicals that can subsequently form covalent bonds through addition reactions. Recently, we could show that for the on-surface polymerization the substrate does not merely serve as support, but takes a vital chemical role.[9] An inert substrate like graphite(001) does not catalyze the surface-mediated homolysis and hence leaves the molecules intact upon physisorption, whereas on Cu(111) and Ag(110) the dehalogenation reaction readily occurs. Yet, instead of directly forming covalent intermolecular bonds, the on-surface generated radicals coordinate to surface supplied metal atoms in an intermediate reaction step. Thereby coordination complexes introduced as "protopolymers" by Weiss and co-workers are formed[10] through a surface-mediated reaction that has meanwhile also been observed for other systems.[11–13] The first reaction step is dissociative adsorption of halogenated aromatic species on a copper catalyst, a reaction scheme that resembles the coupling chemistry described by Ullmann in 1901.[14] Cleavage of carbon−halogen bonds followed by the formation of comparatively strong bonds[15] of the resulting radicals to copper atoms is also an intermediate step in the Ullmann coupling reaction. In the original Ullmann reaction the bidentate radical−copper complex is a short-lived reaction intermediate, while for the surface variant the radical−copper complexes are metastable at room temperature. Subsequent thermal annealing releases the coordinating copper atoms and induces covalent C−C coupling of the aromatic species. The initially split-off bromine species binds to the surface and thermally activated diffusion results in island formation at ∼600 K,[16] whereas desorption takes place at about 950 K.[17] In STM topographs adsorbed bromine atoms appear as depressions on Cu(111), which was explained by quenching of the surface state.[17] In accordance with these findings we also occasionally observe these depressions in the vicinity of protopolymers (see yellow arrow in Figure 1a), which we attribute to split-off bromine atoms, although we cannot unambiguously prove it.

In order to study the role of the metal support in more detail and shed light on the homolysis mechanism, further experiments were conducted on Ag(111), Ag(110), and Cu(111). The substrate temperature during deposition was introduced as an additional parameter. In this study, TBB was deposited on each substrate held at either room temperature or cooled down to ∼80 K. Subsequently, STM was applied to study the intermolecular bonding schemes and to identify products of a possible dehalogenation reaction.

* To whom correspondence should be addressed. E-mail: hermann.walch@physik.uni-muenchen.de (H.W.), markus@lackinger.org (M.L.).
† Ludwig-Maximilians-University.
‡ Deutsches Museum.

10.1021/jp102704q
Published on Web 07/07/2010

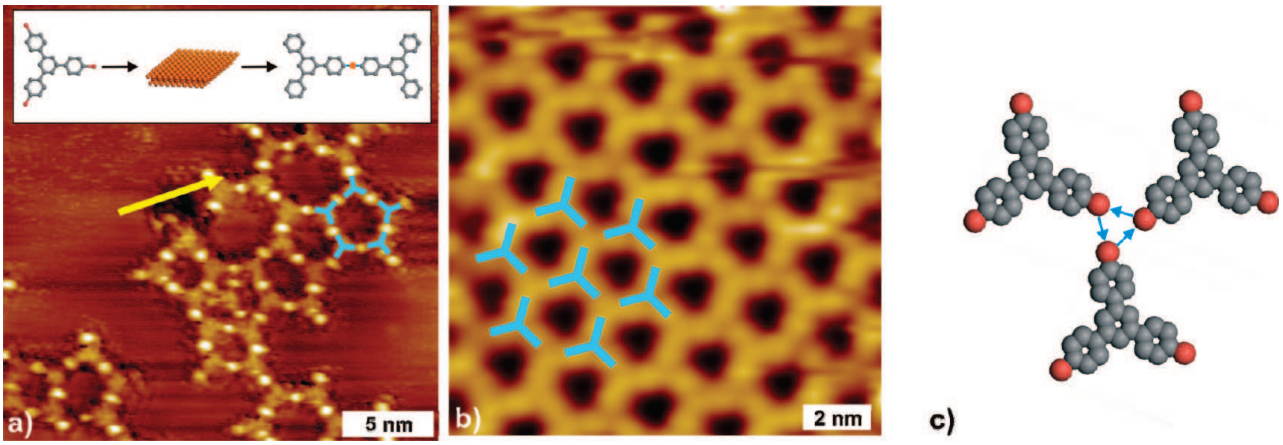

Figure 1. STM topographs of TBB deposited onto Cu(111) with the substrate held at (a) room temperature and (b) ~80 K, respectively. (a) Room-temperature deposition readily induces the dehalogenation reaction and subsequent formation of protopolymers ($U_T = 1.50$ V, $I_T = 85$ pA; inset, reaction scheme). (b) Deposition onto Cu(111) at ~80 K leads to noncovalent self-assembly of a highly ordered structure ($U_T = -1.98$ V, $I_T = 90$ pA). Due to their size and symmetry, the 3-fold bright features are assigned to single intact TBB molecules as shown in the overlay. (c) Tentative model of the intermolecular arrangement based on STM data. As a consequence of a nonspherical charge distribution around the halogen substituents an electrostatic stabilization known as a halogen−halogen bond becomes feasible.

Results and Discussion

Cu(111). Deposition of TBB onto Cu(111) at room temperature leads to the spontaneous formation of protopolymers, in accordance with previous experiments on brominated aromatic molecules.[11,12,17] Coordinating copper atoms are either extracted from terraces[18] or supplied by the free adatom gas that originates from a temperature-dependent condensation/evaporation equilibrium at step edges.[19] An STM topograph of TBB−protopolymer networks on Cu(111), i.e., radical−metal coordination complexes, is depicted in Figure 1a. Bright circular protrusions midst the triangular molecular units are clearly discernible, and readily identified as copper atoms. However, an unambiguous experimental indication for protopolymer formation is the center-to-center distance between interlinked molecules. In full agreement with the anticipated value for protopolymers, a distance of ~1.50 nm was found. The irregularity and high defect density of these networks is owed to both the pronounced reactivity of phenyl radicals and the low directionality of coordination bonds. By virtue of a postannealing step (up to 300 °C), it was possible to release the copper atoms and eventually convert metal-coordination bonds into covalent C−C interlinks. This is accompanied and proven by a ~0.25 nm decrease of the center-to-center distance of adjacent interconnected TBB molecules from ~1.50 nm to ~1.25 nm.[9,12]

In order to gain deeper insight into the dissociation mechanism, the present study also takes the influence of the substrate temperature during deposition into account. In the case of Cu(111), a prominent difference arises depending on the substrate temperature: Deposition of TBB onto Cu(111) held at ~80 K leads to the formation of highly ordered, virtually defect-free self-assembled structures which are comprised of intact molecules. A representative STM topograph and the corresponding structural model are depicted in Figure 1b,c. Single molecules are clearly resolved and appear as 3-fold symmetric features in accordance with the molecular structure. The structure is based on a hexagonal lattice with $a = 2.05 \pm 0.06$ nm and contains one molecule per unit cell. Both, the high degree of ordering and the unit cell dimensions substantiate the conclusion that molecules remain intact and self-assemble due to relatively weak noncovalent interactions. The halogen substituents cannot be distinguished from the aromatic backbone in the submolecular STM contrast, because the frontier molecular orbitals equally have contributions from the aromatic system and the peripheral halogen substituents, respectively. A comparable cyclic bonding pattern among three halogen atoms has previously been observed in bulk crystals of halogenated phenyls.[20] The underlying interaction is of electrostatic origin and attributed to a nonspherical charge distribution around the bromine substituents. Calculations of the electrostatic potential at the halogen atoms propose a positive cap opposite to the C−Br bond and a ring of negative potential around the bond axis.[21] A cyclic intermolecular arrangement as shown in Figure 1c thus optimizes electrostatic interactions and can be described as Coulombic "donor−acceptor" attraction.[20]

Warming up the well-ordered TBB layer on Cu(111) to room temperature also induces the formation of protopolymers, similar to those observed for room-temperature deposition. These experimental findings illustrate that dissociation of C−Br bonds on Cu(111) requires thermal activation and that the thermal energy supplied at 300 K is sufficient.

Ag(110). Regarding the dissociation of C−Br bonds upon room temperature deposition, Ag(110) shows a qualitatively similar behavior as Cu(111): formation of protopolymers was readily observed (Figure 2a). For low-temperature deposition, however, TBB molecules do not form ordered structures; instead, adsorption of isolated, apparently immobile single molecules has been observed, as illustrated in Figure 2b. This result is explained by a more corrugated surface potential on Ag(110) as compared to Cu(111). For face-centered cubic (fcc) metals, the potential energy landscape for adsorbates exhibits higher corrugation on (110) than on (111) surfaces. Consequently, thermally activated surface diffusion is more easily suppressed at lower temperatures on (110) surfaces. In addition, surface diffusion is more anisotropic on (110) surfaces than on densely packed (111). In many cases this results in quasi-one-dimensional diffusion, which also hampers self-assembly of two-dimensional islands. Similar to Cu(111), warming up the low-temperature deposited Ag(110) sample to room temperature results in dehalogenation and spontaneous formation of protopolymers.

In summary, only at room temperature are Cu(111) and Ag(110) sufficiently reactive to catalyze homolysis of C−Br bonds in TBB. For low-temperature deposition, differences concerning the mutual arrangement arose: on the densely packed

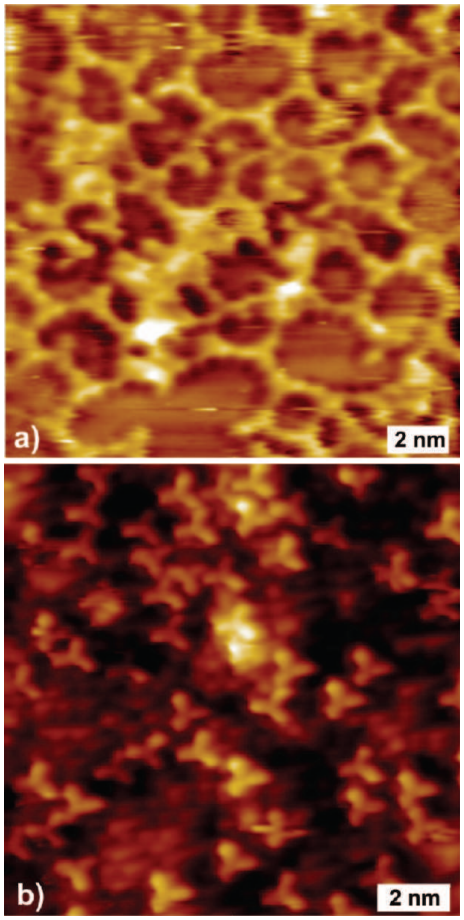

Figure 2. STM topographs of TBB deposited on Ag(110) (a) after warming up the sample to room temperature ($U_T = 1.76$ V, $I_T = 41$ pA) and (b) at ~80 K ($U_T = -1.50$ V, $I_T = 110$ pA). Low-temperature deposition results in disordered arrangements of single molecules without any indication of ordered self-assembly due to suppressed lateral mobility on the (110) face; warming up the sample to room temperature leads to dehalogenation and the formation of protopolymers similar to the case for Cu(111). Albeit adatoms are not resolved in this case, the measured center-to-center distances of 1.50 nm between interlinked molecules clearly indicates formation of protopolymers.

Cu(111) surface the lateral mobility of TBB is sufficient to facilitate self-assembly into ordered monolayers, while on Ag(110) the lack of surface mobility leads to adsorption of isolated molecules.

Ag(111). In order to gain deeper insight into the relevant parameters for the catalytic activity of coinage metal surfaces for this particular homolysis reaction, further experiments were conducted on Ag(111). Low-temperature deposition onto Ag(111) results in self-assembly of a monolayer structure similar to the Cu(111) case. The arrangement of molecules, the symmetry of the monolayer, and within the experimental error, the lattice parameter are identical for low-temperature deposition on Cu(111) and Ag(111). Most importantly, similar to the aforementioned cases, for low-temperature deposition TBB molecules also stay intact upon adsorption on Ag(111). Yet, qualitatively different observations in comparison to Cu(111) were made when TBB was evaporated onto Ag(111) at room temperature. Instead of protopolymers—a clear indication of dehalogenation—a variety of distinct self-assembled phases based on intact molecules was observed. All structures are stabilized by weak noncovalent interactions between intact molecules. Representative STM topographs of the various phases on Ag(111) are presented in Figure 3.[22] It is noteworthy that low-temperature deposition followed by warming up the sample resulted in the same morphologies as deposition directly at room temperature. In the overview image of Figure 3a, two coexisting phases, namely, a hexagonal and a row structure with oblique unit-cell, can be distinguished. Furthermore, in the lower part of the image molecules that are "frozen" in a disordered state can be identified. We attribute the emergence of this phase to rapid surface diffusion at room temperature, which kinetically traps molecules in the disorder state.

A detailed analysis of the intermolecular distances in the disordered phase does not indicate any formation of protopolymers or covalently interlinked aggregates. Close ups of the ordered phases are presented in Figure 3b,c. Similar to the low-temperature polymorphs observed on Cu(111) and Ag(111), the well-ordered structures are likewise stabilized by electrostatic interactions between nonspherical charge distributions of halogen substituents. Yet, the structures of these polymorphs are more complex, and in addition to the triple halogen−halogen bonds, the hexagonal structure also contains six-membered rings of cyclic halogen bonds, as shown in Figure 3b. Three of those supramolecular hexamers are interconnected via single TBB molecules in a triple Br−Br−Br bond pattern similar to those observed in the low-temperature structure. As illustrated by the overlaid symbolic representations of the molecules, attractive halogen−halogen interactions are topologically very versatile and not restricted to three or six membered rings. Also a slightly displaced head-to-head geometry enables favorable electrostatic interactions, as exemplified in Figure 3c, and gives rise to another polymorph, the row structure. The measured center-to-center distances of halogen−halogen bond associated dimers (2.05 nm) is significantly larger than for metal-coordinated (1.50 nm) or covalently interlinked dimers (1.25 nm)[9] and clearly indicates noncovalent interaction. Figure 4 illustrates the three different types of intermolecular bonding schemes and the corresponding center-to-center distances. For the halogen−halogen interaction, the molecules exhibit a slight lateral displacement and significantly larger center-to-center distance as compared to the covalent and metal coordination case. The substantial differences in center-to-center distance allow for a clear distinction of the interaction type solely based on intermolecular distances as measured in STM topographs.

A displaced halogen−halogen bonded dimer is also the basic unit of the structure depicted in Figure 3d, another occasionally observed polymorph that features a rather high packing density. The experimentally observed coexistence of all structures in Figure 3 indicates the relative weakness and topological versatility of halogen−halogen interactions. In any case, it can be stated that for Ag(111) different noncovalent self-assembled structures were observed dependent on the deposition temperature without any indication of dehalogenation either for room temperature or for low temperature deposition.

In brief, the experiments described above reveal a clear dependency of the catalytic activity on the material [Cu(111) vs Ag(111)], but also on the crystallographic surface orientation [Ag(110) vs Ag(111)].

The experimental findings as summarized in Table 1 give rise to the question about the origin and the detailed mechanism of the catalytic activity of the investigated metal surfaces for the dehalogenation reaction. In particular, we want to address the question of which parameters influence the TBB dehalogenation on coinage metal surfaces. Irrespective of substrate material and orientation, for low-temperature deposition we have never observed dehalogenation, a clear indication of a thermally

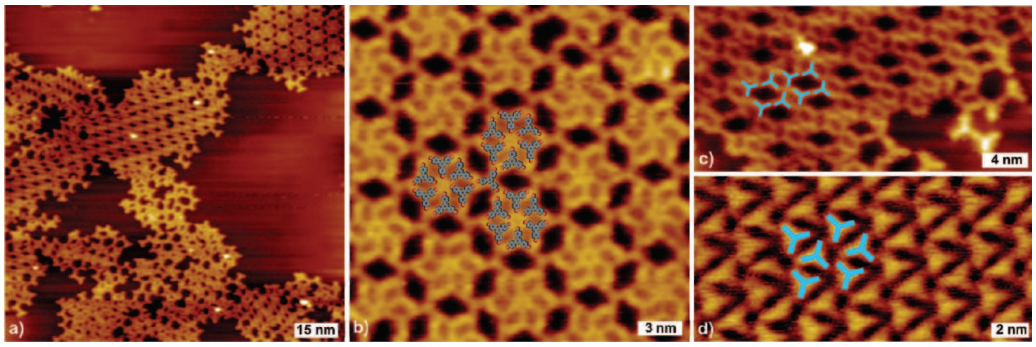

Figure 3. STM topographs of different self-assembled TBB phases on Ag(111). Molecules were deposited at room temperature, while for improved drift stability STM images were acquired at ∼80 K. (a) Overview image presenting two coexisting ordered phases, namely, a row structure on the upper center part and a hexagonal flower structure in the upper right part. The lower half depicts a disordered phase ($U_T = -1.11$ V, $I_T = 102$ pA). (b) Close up of the flower structure with overlaid molecular model ($U_T = -1.11$ V, $I_T = 90$ pA). (c) Close up of the row structure ($U_T = -1.11$ V, $I_T = 112$ pA). (d) Close up of a third, densely packed structure ($U_T = 1.77$ V, $I_T = 94$ pA).

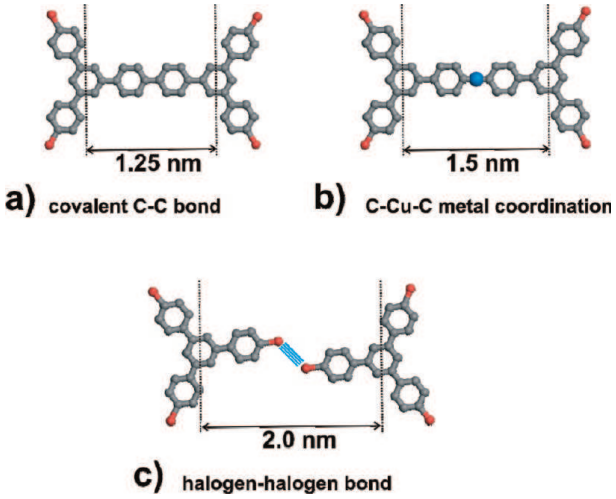

Figure 4. Three possible intermolecular bonding schemes and corresponding center-to-center distances of interlinked molecules. (a) Covalent coupling of TBB molecules leads to the shortest center-to-center distance of ∼1.25 nm. (b) Metal coordination yields a notably higher center-to-center distance of ∼1.50 nm. (c) In addition to cyclic triple halogen−halogen−halogen bonds, also a dimeric arrangement with a center-to-center distance of ∼2.0 nm was observed.

TABLE 1: Summary of Experimentally Observed Intermolecular Bonding Schemes Dependent on Both Substrate Material and Crystallographic Orientation, as Well as Deposition Temperature

	surface @ 80K	surface @ RT
Cu (111)	triple halogen bond	protopolymer
Ag (110)	no ordering	protopolymer
Ag (111)	triple halogen bond	various halogen bond schemes

activated reaction step. TBB molecules do not react and stay intact on the two densely packed Ag(111) and Cu(111) surfaces, where ordered structures were observed. In contrast, on Ag(110) no self-assembly into ordered structures takes place, due to suppressed surface mobility.

In order to understand the substrate dependency of the room-temperature dehalogenation, reactivity is discussed in the framework of heterogeneous catalysis and molecule−metal interactions. Alternatively, an adatom-based surface chemical approach can also explain the experimental findings. Yet, a significant contribution from step edges as active sites for the dehalogenation can be excluded.

Grounded on DFT results, Christensen and Nørskov state that for an accurate description of surface reactivity one has to differentiate between geometrical and electronic effects.[23] In the following, based on their argumentation, we also want to formally distinguish between electronic and geometric effects, where the former can explain the material and the latter the orientation dependency.

The geometrical effect can be explained by means of the active sites concept, which implies that bond cleavage of adsorbates occurs preferentially at low-coordinated surface atoms,[24,25] in particular, at vacancies, kinks, step edges, or dislocations.[8] The literature is rich with examples, where dissociative adsorption favorably occurs at step edges, where reactions rates can be orders of magnitude enhanced as compared to terraces.[26,27]

However, since on Ag(111) dehalogenation has been observed neither for low-temperature nor for room-temperature deposition, it is concluded that the (mostly densely packed) step edges on this surface are not active sites for cleavage of carbon−halogen bonds. Yet, in general, the reactivity of step edges will depend on their crystallographic direction, which determines both the step edge atom coordination and density of kink or ledge sites, giving rise to substantial differences.

Although overview topographs clearly show that many protopolymers are anchored at step edges, we nevertheless exclude a dominant contribution from step edges for the following reason. If the reaction could exclusively proceed at step edges, only step-edge decoration would be observable but not structures extending into terraces. Protopolymers that are bound to step edges would block these active sites and passivate them, resulting in a quenching of the reaction. Such a self-poisoning effect has, for instance, been observed for the dissociation of ethylene on Ni(111) step edges.[28] In conclusion, a dominant contribution from step edges can be ruled out for the dehalogenation reaction.

In the following it is argued that the reactivity differences might originate already in the different atomic arrangement of ideal surfaces and no special active sites are required. While the (111) surfaces of fcc metals are densely packed, the (110) surfaces consist of alternating atomic rows and troughs running along the [$\bar{1}$10] direction. In some respect the (110) surfaces can be seen as a dense stringing of step edges, thereby exposing a large area density of low coordinated surface atoms that

promote the catalytic activity. For comparison, the coordination number of a topmost surface atom in an ideal fcc (111) surface is 9 while for an ideal fcc (110) surface the coordination number is only 7. The coordination number can directly affect the energy of the d-band center and thus the reactivity of the respective sites.[29]

A more direct electronic aspect of the catalytical activity comes into play for understanding the observed differences between Cu(111) and Ag(111). Adsorption of aromatic molecules on transition-metal surfaces leads to significant changes in their electronic structure, as concluded for instance from ultraviolet photoelectron spectroscopy (UPS),[30] scanning tunneling spectroscopy (STS),[31] and density functional theory (DFT) studies.[32–34] Depending on the interaction strength, level shifts, level broadening, or emergence of new electronic states due to hybridization are common and most seriously affect frontier molecular orbitals.[35] For instance, Thygesen and Rubio show that the HOMO−LUMO gap of adsorbed molecules shrinks with increasing interaction strength.[36] For the aromatic molecule 3,4,9,10-perylenetetracarboxylic acid dianhydride (PTCDA), it has been shown that fully or partly filled LUMO-derived interface states are created upon adsorption on Cu(111) and Ag(111), respectively, rendering the organic layers semiconducting or metallic. On Au(111), on the other hand, only "soft chemisorption" is reported, where energy levels do not shift significantly because of a relatively weak interaction.[37] These findings are in accordance with the proposed trend of decreasing reactivity for the d10s1 transition metals when moving down this group in the periodic table of the elements from Cu over Ag to Au.[38] This reactivity order was also confirmed by UPS measurements of PTCDA[37] and pentacene[35] on noble metal surfaces. Both compounds serve as model systems for interaction of large π-conjugated molecules with metal surfaces. Since the underlying processes are fundamental and by no means specific for PTCDA or pentacene, it is proposed that this reactivity order can be generalized for other planar π-conjugated aromatic adsorbates. In both cases the newly formed hybridized orbitals originate from interaction of the π-electrons with the metal s- and d-states, in line with the Newns−Anderson model.[30,39] Adsorption of aromatic molecules on transition-metal surfaces is also accompanied by charge transfer between adsorbate and substrate as a consequence of the aforementioned adjusting of the frontier molecular orbitals.[35,37] This can lead to partial filling of mainly the π^* orbital, where the degree of occupancy increases with increasing interaction strength and is thus largest on copper surfaces. Since the π^* orbital is mainly localized at the aromatic system, adsorption induced charge transfer can still not explain the observed homolysis of peripheral C−Br bonds. In order to explain the bond cleavage, we propose that thermally activated charge transfer from the newly occupied π^* into σ^* orbitals, which are antibonding with respect to the C−Br bond, eventually destabilizes these bonds and facilitates homolysis. A similar two-step mechanism for C−X bond dissociation in solution was found by Kimura and Takamuku, who studied halogen scission in aryl halides[40] and benzyl halides[41] by means of low-temperature pulse radiolysis. First, an additional electron is captured by the π^* orbital and then in a second step transferred into the C−halogen σ^* orbital. This results in destabilization and dissociation of the C−Br bond. Moreover, a comparable two-step mechanism is also discussed for photodissociation of dibromobenzene and tribromobenzene, where the initially excited singlet (π, π^*) state in the phenyl ring decays into the repulsive triplet (n,σ^*) state located at the C−Br bond.[42] On the basis of these findings we conclude that the dehalogenation of TBB on densely packed noble metal surfaces can only occur when the interaction strength is sufficiently strong. Evidently, this criterion is fulfilled for Cu(111), but not for Ag(111). For higher corrugated (110) surfaces, however, the reactivity of Ag(110) becomes sufficient to catalyze the dehalogenation reaction. Along the lines of heterogeneous catalysis research, the higher reactivity of Ag(110) as compared to Ag(111) is explained with the higher surface corrugation leading to a lower coordination and thus higher reactivity of surface atoms. Again, Zou and co-workers have confirmed this trend for the adsorption of PTCDA on Ag(111) and Ag(110), where the more corrugated (110) face exhibits stronger interaction.[30]

As already stated above, a decisive influence of adatom chemistry would also be consistent with our experimental observations and cannot be fully excluded. It is well-known that for metal surface chemistry adatoms can be important mediators or reaction partners for various types of reactions.[29] Consequently, both the temperature and surface dependent density of the adatom gas as well as the adatom reactivity can explain reactivity differences. For instance, a face-specific dependency for the adsorption geometry of benzoate molecules has been attributed to the availability of metal adatoms, being significantly higher on Cu(110) as compared to Cu(111).[43] It has also been reported that the deprotonation of carboxylic groups in trimesic acid molecules does not take place on pristine Ag(111) at room temperature but can be triggered by an additional supply of more reactive copper atoms.[19] Especially the latter example exemplifies the importance of adatom chemistry for the formation of metal-coordination complexes on surfaces. In this picture, the temperature dependence can be explained by suppression of the adatom gas at lower temperature, while the orientation dependence can be explained by different binding energies of atoms in step edges. However, since we do not observe any formation of protopolymers on Ag(111), a dominant contribution from adatoms for the dehalogenation reaction seems unlikely. Even though the density of adatoms on fcc(111) surfaces is substantially lower than on (110) surfaces, as rationalized by a model based on the change of coordination number for the detachment process,[43] at least a few coordination complexes should also be observable on Ag(111), if the reaction was exclusively driven by adatoms. However, a plain consideration of merely the adatom density is not satisfying, and also the adatom reactivity has to be considered. Since the coordination number of adatoms is also surface-dependent, it is conceivable that Ag adatoms behave chemically distinctly on (111) than on (110) surfaces. In order to obtain a detailed and quantitative understanding of the dehalogenation reaction, theoretical studies that address the electronic structure of the chemisorbed molecule−substrate complex and tackle conceivable reactivity differences of adatoms are very desirable.

Conclusions

In summary, studies of a heterogeneously catalyzed dehalogenation reaction, namely full debromination of the aromatic compound TBB, on single crystal metal surfaces revealed interesting reactivity differences. Since the reaction only proceeds on Cu(111), but not on Ag(111), the catalytic capability of the substrate for this reaction is clearly material dependent. On the other hand, the dehalogenation reaction took place on Ag(110), thereby exemplifying that also the specific surface orientation can be decisive. Third, in variable-temperature experiments it was found that the dehalogenation reaction cannot proceed at low substrate temperatures (~80 K) irrespective of

the substrate, thereby proving the necessity of thermal activation. In order to explain the occurrence of the reaction as a function of different experimental parameters, we propose a two-step mechanism, where initial charge transfer upon adsorption provides the basis for occupation of an antibonding orbital. Besides the recognized role of active sites, this comparative series of experiments elucidates that the overall reactivity of a catalytically active surface originates from a combination of atomic arrangement and electronic structure.

For future experiments, it would also be enlightening to study the role of the organic compound and its respective electronic structure. For instance, the HOMO−LUMO gap can be altered by means of decreasing or increasing the size of the aromatic system, thereby also affecting the level alignment and magnitude of charge transfer. The strength of the carbon−halogen bond is another accessible parameter worthy of study. This bond can be weakened by substituting bromine with iodine, but it can also be strengthened by substituting bromine with chlorine.

Methods

All samples were prepared and characterized in an ultrahigh vacuum chamber (base pressure $<5 \times 10^{-10}$ mbar) equipped with a scanning tunneling microscope (STM). Metal single crystals [Cu(111), Ag(111), and Ag(110)] were prepared by repeated cycles of Ne^+ ion sputtering and annealing. 1,3,5-Tris(4-bromophenyl)benzene was obtained from a commercial source (Sigma Aldrich) and vacuum sublimed from a home-built Knudsen cell with crucible temperatures between 150 and 160 °C.[44] Samples were deposited in the microscope, which is a home-built beetle-type STM mounted on a flow cryostat and thus able to operate at variable temperatures. During deposition the STM and the substrates were held either at room temperature or at ∼80 K. Typically, images were acquired at ∼80 K (also for room temperature deposition), because of improved drift stability of the instrument at low temperatures.

Acknowledgment. Financial support by the Deutsche Forschungsgemeinschaft (SFB 486) and the Nanosystems Initiative Munich (NIM) is gratefully acknowledged. G.E. acknowledges support by the Hanns-Seidel-Stiftung.

References and Notes

(1) Ertl, G.; Freund, H. J. *Phys. Today* **1999**, *52*, 32–38.
(2) Ertl, G. *J. Vac. Sci. Technol., A* **1983**, *1*, 1247–1253.
(3) Bowker, M. *Surf. Sci.* **2009**, *603*, 2359–2362.
(4) Bowker, M. *Chem. Soc. Rev.* **2007**, *36*, 1656–1673.
(5) Vang, R. T.; Lauritsen, J. V.; Laegsgaard, E.; Besenbacher, F. *Chem. Soc. Rev.* **2008**, *37*, 2191–2203.
(6) Leibsle, F. M.; Murray, P. W.; Francis, S. M.; Thornton, G.; Bowker, M. *Nature* **1993**, *363*, 706–709.
(7) Africh, C.; Comelli, G. *J. Phys.: Condens. Matter* **2006**, *18*, R387–R416.
(8) Zambelli, T.; Wintterlin, J.; Trost, J.; Ertl, G. *Science* **1996**, *273*, 1688–1690.
(9) Gutzler, R.; Walch, H.; Eder, G.; Kloft, S.; Heckl, W. M.; Lackinger, M. *Chem. Commun.* **2009**, 4456–4458.
(10) Sykes, E. C. H.; Han, P.; Kandel, S. A.; Kelly, K. F.; McCarty, G. S.; Weiss, P. S. *Acc. Chem. Res.* **2003**, *36*, 945–953.
(11) McCarty, G. S.; Weiss, P. S. *J. Am. Chem. Soc.* **2004**, *126*, 16772–16776.
(12) Lipton-Duffin, J. A.; Ivasenko, O.; Perepichka, D. F.; Rosei, F. *Small* **2009**, *5*, 592–597.
(13) Xi, M.; Bent, B. E. *J. Am. Chem. Soc.* **1993**, *115*, 7426–7433.
(14) Ullmann, F.; Bielecki, J. *Ber. Dtsch. Chem. Ges.* **1901**, *34*, 2174–2185.
(15) Migani, A.; Illas, F. *J. Phys. Chem. B* **2006**, *110*, 11894–906.
(16) Nanayakkara, S. U.; Sykes, E. C. H.; Fernandez-Torres, L. C.; Blake, M. M.; Weiss, P. S. *Phys. Rev. Lett.* **2007**, *98*, 206108.
(17) Blake, M. M.; Nanayakkara, S. U.; Claridge, S. A.; Fernandez-Torres, L. C.; Sykes, E. C. H.; Weiss, P. S. *J. Phys. Chem. A* **2009**, *113*, 13167–13172.
(18) Pai, W. W.; Bartelt, N. C.; Peng, M. R.; Reuttrobey, J. E. *Surf. Sci.* **1995**, *330*, L679–L685.
(19) Lin, N.; Payer, D.; Dmitriev, A.; Strunskus, T.; Woll, C.; Barth, J. V.; Kern, K. *Angew. Chem., Int. Ed.* **2005**, *44*, 1488–1491.
(20) Bosch, E.; Barnes, C. L. *Cryst. Growth Des.* **2002**, *2*, 299–302.
(21) Awwadi, F. F.; Willett, R. D.; Haddad, S. F.; Twamley, B. *Cryst. Growth Des.* **2006**, *6*, 1833–1838.
(22) In order to improve the drift stability of the microscope, measurements were performed at ∼80 K, also for samples where molecules were deposited at room temperature.
(23) Christensen, C. H.; Norskov, J. K. *J. Chem. Phys.* **2008**, *128*, 182503.
(24) Taylor, H. S. *Proc. R. Soc. London, Ser. A* **1925**, *108*, 105–111.
(25) Norskov, J. K.; Bligaard, T.; Hvolbaek, B.; Abild-Pedersen, F.; Chorkendorff, I.; Christensen, C. H. *Chem. Soc. Rev.* **2008**, *37*, 2163–2171.
(26) Gambardella, P.; Sljivancanin, Z.; Hammer, B.; Blanc, M.; Kuhnke, K.; Kern, K. *Phys. Rev. Lett.* **2001**, *87*, 056103.
(27) Liu, Z. P.; Hu, P. *J. Am. Chem. Soc.* **2003**, *125*, 1958–1967.
(28) Vang, R. T.; Honkala, K.; Dahl, S.; Vestergaard, E. K.; Schnadt, J.; Laegsgaard, E.; Clausen, B. S.; Norskov, J. K.; Besenbacher, F. *Nat. Mater.* **2005**, *4*, 160–162.
(29) Hammer, B. *Top Catal* **2006**, *37*, 3–16.
(30) Zou, Y.; Kilian, L.; Scholl, A.; Schmidt, T.; Fink, R.; Umbach, E. *Surf. Sci.* **2006**, *600*, 1240–1251.
(31) Kilian, L.; Hauschild, A.; Temirov, R.; Soubatch, S.; Scholl, A.; Bendounan, A.; Reinert, F.; Lee, T. L.; Tautz, F. S.; Sokolowski, M.; Umbach, E. *Phys. Rev. Lett.* **2008**, *100*, 136103.
(32) Bilic, A.; Reimers, J. R.; Hush, N. S.; Hoft, R. C.; Ford, M. J. *J. Chem. Theory Comput.* **2006**, *2*, 1093–1105.
(33) Toyoda, K.; Nakano, Y.; Hamada, I.; Lee, K.; Yanagisawa, S.; Morikawa, Y. *J. Electron Spectrosc. Relat. Phenom.* **2009**, *174*, 78–84.
(34) Romaner, L.; Nabok, D.; Puschnig, P.; Zojer, E.; Ambrosch-Draxl, C. *New J. Phys.* **2009**, *11*, 053010.
(35) Yamane, H.; Kanai, K.; Ouchi, Y.; Ueno, N.; Seki, K. *J. Electron Spectrosc. Relat. Phenom.* **2009**, *174*, 28–34.
(36) Thygesen, K. S.; Rubio, A. *Phys. Rev. Lett.* **2009**, *102*, 046802.
(37) Duhm, S.; Gerlach, A.; Salzmann, I.; Broker, B.; Johnson, R. L.; Schreiber, F.; Koch, N. *Org. Electron.* **2008**, *9*, 111–118.
(38) Hammer, B.; Norskov, J. K. *Nature* **1995**, *376*, 238–240.
(39) Tautz, F. S. *Prog. Surf. Sci.* **2007**, *82*, 479–520.
(40) Kimura, N.; Takamuku, S. *J. Am. Chem. Soc.* **1995**, *117*, 8023–8024.
(41) Kimura, N.; Takamuku, S. *Bull. Chem. Soc. Jpn.* **1993**, *66*, 3613–3617.
(42) Kadi, M.; Davidsson, J. *Chem. Phys. Lett.* **2003**, *378*, 172–177.
(43) Perry, C. C.; Haq, S.; Frederick, B. G.; Richardson, N. V. *Surf. Sci.* **1998**, *409*, 512–520.
(44) Gutzler, R.; Heckl, W. M.; Lackinger, M. *Rev. Sci. Instrum.* **2010**, *81*, 015108.

JP102704Q

Acknowledgements

Needless to say, a work of this extent would not have been possible to complete without the help and support of a lot of people. I thank Markus Lackinger for giving me the opportunity to work in his research group. Innumerous discussions on physical principles and the interpretation of data contributed significantly to my understanding of molecular self-assembly as summarized in this work. Most technical issues would probably still be unresolved without his help. I also would like to acknowledge the hundreds of kilometers we ran together as a meditative approach towards the scientific problems we encountered during the last years. I am also grateful to Wolfgang Heckl for his constant support during the last years and the opportunity to complete my research in his laboratory.

As the definition of (research) team implies, all work presented here is the fruit of people working together. The constant struggle and pain to set up a working UHV STM was alleviated by alike suffering of Hermann Walch, whose musical contribution to our work environment in the laboratory cannot be underestimated. Moral support was always offered by the ever optimistic Marek Janko, especially in times when nothing seemed to work out. Stephan Kloft's effort, who worked along on the set up of the vacuum system, is the main reason why the STM is now functional. Thommi Sirtl's incomparable ability to record beautiful STM images was as important to the progress of my work as was the time we spent skiing and snowboarding the Alps. Of course, all other members and some non-members of the group contributed equally to the success of this work: Georg Eder, Jürgen Dienstmaier, Anne-Kathrin Maier, Sophie Lappe, Christoph Heininger, Alexander Gigler, and Michael Bauer. All of them contributed to my understanding of different parts of physics, chemistry, and the world in general.

Special thanks go to the machine shop of the faculty of geosciences, especially to Günter Hesberg. Only through their ability to decipher my requests and to machine them into functional components a great part of my work was made possible.

Michael Schmittel and his research group at the University of Siegen supplied most of the molecules investigated. I thank them for their effort in synthesizing the chemicals and also for the important exchange of thoughts on our common projects.

Finally I thank the most important persons in my life: Marta for her endless patience and her choice to join me on a common journey through the world and through life, and likewise my mother and especially my father, who I am sure would have enjoyed to witness the day of my graduation. They all deserve thanks for their everlasting support and their faith in me.

CV

since 01/2010	postdoctoral fellow at the Institut National de la Recherche Scientifique - Énergie, Matériaux et Télécommunications, Montreal, Canada
01/2007 - 12/2009	graduate student at the faculty of geosciences, Ludwig-Maximilians-University, Munich, Germany
10/1999 - 01/2006	university studies in physics and astrophysics at Freie Universität Berlin and the universities of Seville and La Laguna, Spain
10/1998 - 10/1999	social service at the otorhinolaryngology laboratory of Charité university hospital, Berlin, Germany
06/1998	Abitur (high school diploma equivalent) at John-F.-Kennedy high school, Berlin, Germany